

Diss. ETH No. 19742

High Frequency Atomic Force Microscopy

A dissertation submitted to the
ETH ZÜRICH

for the degree of
Doctor of Sciences

presented by

RAOUL ENNING

M.Sc. ETH
born 5 September 1980
citizen of Germany and the United States of America

Prof. Dr. A. Stemmer, examiner
Dr. U. Duerig, co-examiner

Zürich, 2011

"Give me a place to stand and a (optical) lever long enough and I will move the world."
-Archimedes (more or less) *c.* 250 BC

Abstract

The cantilever deflection sensor is one of the most important and sensitive elements of the atomic force microscope (AFM). Of all methods proposed to detect cantilever deflection, the optical beam deflection method (OBD) is the most widely used due to the ease of beam alignment and simple experimental setup. Theoretical studies have suggested that OBD sensitivity should be equal or even significantly better than alternate detection techniques, like interferometric detection. However, experimentally, interferometric detection methods have proven to be more capable of satisfying low noise and bandwidth requirements.

The bandwidth of the deflection sensor defines the frequency limit of data acquisition from the rapid motility of the mechanical cantilever / surface interaction. In addition, the noise performance of these OBD sensors can limit the sensitivity of detectable deflections and can reduce or influence the stability of lock-in amplifiers, phase locked loops, and other cantilever control mechanisms. Optimizations and advances of these sensors in bandwidth and noise would allow the use of high spring constant, high resonance frequency cantilevers resulting in improvements of both scan speed and resolution. Improving the smallest detectable amplitudes will allow a very local probing of the surface forces, resulting in higher resolution imaging. It has been shown previously that improvements in OBD readouts that reach noise levels dictated only by the thermal oscillations of the cantilever while maintaining high bandwidths are possible.

In this thesis, we extended and improved AFM bandwidth, noise and resolution in ambient conditions by redesigning the electrical and electrooptical components of the beam deflection technique. Through the invention of a novel optical beam deflection readout, we are able to directly measure oscillations in excess of 20 MHz without an increase in noise levels. Theory suggests that increases in cantilever resonance frequencies can improve the thermal noise limitation of the cantilever by a significant factor as well as decreasing the response latency of the oscillating cantilever, thus allowing more rapid scanning. Increasing the measurement bandwidth of AFM while maintaining a very low noise level can thus create new opportunities in lateral and topographical resolution, high-speed scanning, force spectroscopy measurements, utilizing higher eigenmodes and their resulting multi-frequency operations, minimum detectable amplitudes, and improved resolutions in Kelvin probe force microscopy techniques. As the noise of any system is only as low as it's strongest contributor, the laser light source used in the beam deflection was high frequency modulated in order to reduce the invasive longitudinal

mode hopping of the laser, and show that this technique significantly improves noise for certain situations.

Finally we show that the newly developed microscope has the sensitivity to achieve very high resolution images in ambient conditions, using high frequency cantilevers on mica and HOPG samples.

Zusammenfassung

Der Biegebalkenauslenkungssensor ist eines der wichtigsten und empfindlichsten Elemente des Rasterkraftmikroskopes (AFM). Von allen potentiellen Methoden zur Erkennung einer Balkenauslenkung ist die Methode der optischen Strahlablenkung die am weitesten verbreitete (OBD), unter anderem wegen der Leichtigkeit der Strahlausrichtung und des einfachen Versuchsaufbaus. Theoretische Untersuchungen haben ergeben, dass OBD-Empfindlichkeiten gleichauf oder sogar deutlich besser sein sollten, als alternative Methoden zur Erfassung von Strahlablenkungen wie die interferometrische Erkennung. Experimentell sind interferometrische Erkennungsverfahren dem Strahlablenkungsverfahren in Bandbreite und Rauschverhaeltnissen ueberlegen.

Die Bandbreite des Auslenksensors limitiert die Erfassungsfrequenz der Wechselwirkung zwischen der mechanischen Spitze und der Oberflaeche. Die Rauschleistung dieser OBD-Sensoren begrenzt die Empfindlichkeit einer nachweisbaren Auslenkung; dieses wiederum reduziert die Stabilitaet von Lock-in Verstaerkern, Phasenregelschleifen und andere Reglermechanismen. Optimierungen dieser Sensoren auf hoehere Bandbreiten und verringertem Rauschen ermoeglicht die Verwendung von Biegebalken mit hoher Federkonstante und hoher Resonanzfrequenz. Dieses wiederum verbessert die Scan-Geschwindigkeit und Aufloesung. Kleinere nachweisbare Amplituden ermoeglichen eine sehr lokale Sondierung der Oberflaechenkraefte, was zu einer hoeheren Aufloesung beitraegt. Bereits frueher haben Verbesserungen bei OBD Sensoren die Rauschbelastung soweit reduziert, dass nur die thermischen Schwingungen des Biegebalkens die Empfindlichkeit des Systems limitiert.

In dieser Arbeit wird die AFM Bandbreite, das Rauschen und die Aufloesung erweitert und verbessert durch die Neugestaltung der elektrischen und elektrooptischen Komponenten der Strahlauslenkungstechnik in einem vorhandenen AFM. Durch die Erfindung eines neuartigen optischen Strahlablenkungssensors, koennen wir direkt Schwingungen von ueber 20 MHz messen ohne eine Erhoehung des Rauschpegels. Die Theorie besagt, dass eine Erhoehung der Resonanzfrequenzen die Begrenzung des thermischen Rauschens des Biegebalkens um einen wesentlichen Faktor reduziert, sodass noch kleinere Amplituden aktiv angeregt werden koennen. Die gleichzeitige Erhoehung der Messbandbreite und der sehr geringe Geraeuschpegel eroeffnen somit neue Chancen in lateraler und topographischer Aufloesung, im Hochgeschwindigkeitsscannen, in spektroskopischen Messungen, in der Ausnutzung hoeherer Eigenmoden und dem daraus resultierenden Multi-Frequenz-Betrieb, in den kleinsten messbaren Amplituden, und in

einer verbesserten Auflösung in Raster-Kelvin-Mikroskopie-Techniken. Die Rauschbelastung eines Systems ist nur so niedrig wie der stärkste rauscherzeugende Faktor. Der Speisestrom in der Laserlichtquelle wird deswegen hochfrequent moduliert, um den invasiven "Mode Hopping" des Lasers zu reduzieren; es wird gezeigt, dass diese Methodik die Rauschstabilität in bestimmten Situationen erheblich verbessert.

Zum Schluss zeigen wir, dass das neu entwickelte Mikroskop die Fähigkeit hat, atomar aufgelöste Bilder mit hochfrequenten Spitzen in Umgebungsbedingungen auf Glimmer und HOPG zu erzeugen.

Acknowledgements

First and foremost I would like to thank Prof. Andreas Stemmer for giving me the opportunity and the freedom to try out some wild ideas. His patience and guidance during my rather invasive and sometimes amateurish modifications of expensive laboratory microscopes was unprecedented. I would like to thank Dr. Urs Duerig from IBM Research in Rueschlikon, Switzerland, for agreeing to be a co-examiner for my thesis, and for proofreading the text.

The members of the Nanotechnology Group deserve many thanks for the easygoing working environment and constructive advice, not to mention all the great laughs during the coffee breaks! Particularly I would like to thank Dr. Dominik Ziegler for the many intensive brainstorming and idea generation sessions, and Ralph Friedlos for his omnipotent knowledge of the lab equipment. Many other members have come and gone, and I would like to mention them: Dr. Markus Beck, Dr. Reto Fiolka, Kristina Javor, Dr. Khaled Kaja, Dr. Claudia Kuettel, Lea Nowack, Antje Rey, Dr. Miho Sakai, Dr. Livia Seemann, Dr. Jing-Hua Tian, Dr. Krithika Venkataramani, and Dr. Xun Wei. I also like to thank all the students whose projects were conducted under my supervision: Corrado Fraschina, Adrian Nievergelt, and Giselher Wichmann.

I would like to thank Dr. Jeroen van Heijst, Thomas Bauer, Dr. Junji Sakamoto and Prof. Dieter Schlueter from the Polymer Chemistry Department (ETH Zuerich) for their collaborations in 2-D Polymer analysis, and for all the work involved in supplying samples.

I would like to thank Mathieu Burri and Christoph Richter of Nanoworld AG for providing the USNMCB and USCSi prototype small dimensional cantilevers. I would like to thank Dr. Thomas Burger and the Institute for Integrated Systems (ETH Zuerich) for the training and use of their network analyzer. Also, many thanks to Dr. Giacomo Indiveri at the Institute of Neuroinformatics (ETH Zuerich) for looking over some of my ideas and confirming that I am not crazy, and for his course in Analog VLSI that was the basis for my ideas in this thesis. The services rendered by Andreas Stuker and the ETH's Physics Machine Shop are also greatly appreciated.

Finally I would like to thank my family, friends and everyone that showed me love and support during my thesis, the last few months of which has undoubtedly been one of the most challenging and stressful moments of my life.

Technical Acknowledgments

All circuits and layouts were designed using the wonderful and free E.A.G.L.E. CAD (Cadsoft, Pembroke Pines, FL, USA) schematic and layout editor and Protel (Altium Ltd., Sydney, Australia). Circuit design simulations were run using OrCAD PSpice (Cadence Design Systems, San Jose, CA, USA). The manufactured mechanical parts were designed using Inventor 2010 (Autodesk, Inc., San Rafael, CA, USA). Figures were generated using MATLAB R2008b (MathWorks, Natick, MA, USA); the images in this document were created and or edited using Corel-Draw X3 (Corel Corporation, Ottawa, Ontario, Canada), and this document was written and compiled using \LaTeX .

Contents

1	Introduction	5
1.1	Motivation	5
1.2	Scope of this Thesis	7
2	Principles of Scanning Probe Microscopy	9
2.1	Scanning Probe Microscopy	9
2.2	Scanning Tunneling Microscopy	10
2.3	Raster Scanning Technique	11
2.4	Resolution of the STM	12
2.5	Forces	14
2.5.1	Contact Forces	14
2.5.2	Van-der-Waals Forces and the Lennard-Jones Potential	15
2.5.3	Electrostatic Forces	17
2.5.4	Capillary Forces	17
2.5.5	Frictional Forces	19
2.6	Atomic Force Microscopy	20
2.6.1	The Cantilever	20
2.6.2	Interferometric Detection	27
2.6.3	Optical Beam Deflection	27
2.7	Scanning and Control Techniques	31
2.7.1	Force Distance Curves	33
2.7.2	Contact Mode and Frictional Force Microscopy	34
2.7.3	Cantilever Actuation	36

2.7.4	Amplitude Modulation	37
2.7.5	Frequency Modulation	38
2.7.6	Small Amplitude AFM	40
2.7.7	Bandwidth and Noise Limits of the state of the art AFM	41
2.7.8	The Shot Noise Limit	42
3	Translinear Beam Deflection Sensor	43
3.1	Adding and Subtracting Currents: The Current Mirror	43
3.2	Translinear Principle	44
3.3	Translinear Optical Beam Deflection Sensor	47
3.3.1	Extracting the Sum	48
3.3.2	Signal Normalization and Amplification	48
3.3.3	Dual Channel Translinear Readout	49
3.3.4	Implementation	49
3.3.5	Bandwidth Measurements using Emulated Photodiodes	50
3.4	Application	52
3.4.1	Bandwidth Measurements of Selected High Frequency Cantilevers	52
3.4.2	DC Stability	54
3.5	Noise Evaluation	54
3.5.1	Input Bias Current Gain	56
3.5.2	Emitter Resistor Gain	56
3.5.3	Calculating Noise Factor	59
3.6	Conclusion	60
4	Optoelectronics	61
4.1	Laser Diodes	61
4.1.1	Laser Diode Noise Origins	62
4.1.2	Effects of Mode Hopping in AFM	64
4.1.3	Laser Diode Driver	66
4.2	High Frequency Modulation	67
4.2.1	Interference Reduction through Modulation	68
4.2.2	Noise Relationship	68

4.3	Conclusion	69
5	Small Cantilevers and High Resolution Imaging	71
5.1	Spectral Noise Density Measurements	72
5.2	Small Dimensional Cantilevers	72
5.2.1	High Resolution Scanning in Ambient Environments	75
5.2.2	Atomic Resolution Imaging	77
5.2.3	Selected High Resolution Images	78
5.3	Conclusion	80
6	Summary and Outlook	81
7	Appendix A: AFM Instrumentation	85
7.1	Base Redesign	85
7.2	Optical Redesign	87
7.3	Electronic Redesign	89
7.4	Conclusion	94
8	Appendix B: Photothermal Excitation	97
8.1	Experimental Setup	99
8.2	Photothermal Excitation of Higher Eigenmodes	100
8.3	Conclusion	104
9	Appendix C: Analysis of 2-D Polymer Surfaces	105
9.1	Thin Film Characterization and Visualization	105
9.2	Conclusion	110

Chapter 1

Introduction

Microscopes are devices that magnify views of very, very small features to macro-scale images suitable for human interpretation. The atomic force microscope is a very powerful device capable of delivering features of objects and surfaces down to fractions of a nanometer, where the rituals and routines of atoms in their native environment can be observed, measured, and quantified. The applications in science are wide ranging and intuitive— from imaging biological samples, viruses, and DNA, to evaluating the chemical and atomic orientations of polymers, crystals, or other man-made structures on the nanometer scale. Understandably, the minuscule power of signals originating from these tiny interactions need to be handled very carefully, and magnified immensely. Only through the combination of the magnification power of the microscope with the technological advances in signal processing and computation of the past 20 years has this science managed to arrive at the extraordinary level where it is today.

1.1 Motivation

Theoretical physicists have spent a good portion of the past 30 years attempting to tie all known theories of physics together into one unified "theory of everything" [Weinberg93]. Such a theory, if it existed, would be capable of properly predicting the outcome of every imaginable experiment. The idea of having to study only one single formula or physical law is very appealing, however in reality most educational tracks in science and engineering that this author knows about take a number of years to complete.

The situation is no different when working in the field of microscopy. Ideally, one would like to use a microscope that could acquire any desired result from any sample. This, unfortunately, is not possible. Combining multiple different types of microscopes is possible [Stemmer88, Stemmer89], however every type of microscope has its strengths and weaknesses. The light microscope, the device most commonly associated with microscopy, is an excellent device for

imaging biological samples like cells and bacteria, and micrometer sized objects. Due to the wave nature of the light normally used (visible light, 400 - 700 nm wavelength), the resolving power of the light microscope ends at approximately 250 nm, according to the Rayleigh criterion.

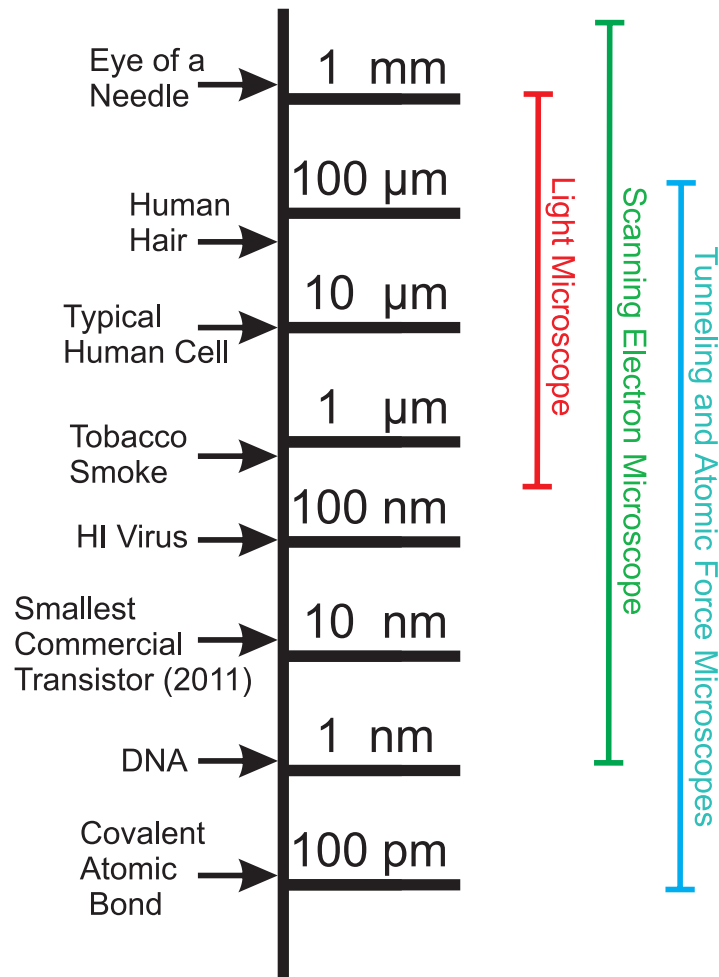


Figure 1.1: A size distribution chart of some commonly known objects and particles, including methods that can be used to image them.

The scanning electron microscope (SEM), a device which scans a sample in a raster-like pattern using a high energy electron beam, has a very large magnification range. The device is capable of scanning mm sized scan areas and samples, onto which the device can then zoom in down to nanometer resolution. Due to the high energy electron beam, the sample must be immersed in vacuum in order to avoid resorption of the electrons by the environmental gas. Thus, all samples must survive high vacuum, which significantly limits the viewing of many biological samples in

their native, untreated state in a high vacuum SEM. In addition, sample surfaces must generally be electrically conductive and grounded to prevent the accumulation of charge at the surface. Non-conducting samples must then be coated with a thin layer of a conducting metal; gold is commonly used for this purpose.

Both the light microscope and the SEM rely on electromagnetic radiation or the emission of electrons to create an image in the plane horizontal to the surface. It is difficult to evaluate the true height or depth of features on a studied surface using these techniques. The atomic force microscope (AFM) is a device which solves these problems— it can precisely evaluate the height and depth of said features, creating true, three dimensional images with a potential for extreme resolution. The AFM is a mechanical microscope, signals are generated by moving a sharp probe in a raster-like pattern over a surface, so close that the probe experiences local force field interactions with the surface. Measuring these interactions with the highest sensitivity is the challenge that this thesis is intent on pursuing.

1.2 Scope of this Thesis

Signal-to-noise is one of the most important concepts when designing any instrument for sensitive measurements; this is true for AFM as well. Detection of the mechanical motion of the cantilever, essentially the generation of a usable signal, is done by the cantilever deflection sensor, which is one of the most important and sensitive elements of the AFM. The bandwidth of the deflection sensor defines the frequency limit of data acquisition from the rapid motility of the mechanical cantilever / surface interaction. In addition, the noise performance of these beam deflection sensors can limit the sensitivity of detectable deflections and can reduce or influence the stability of lock-in amplifiers, phase locked loops, and other cantilever control mechanisms. Optimizations and advances of these sensors in bandwidth and noise would allow the use of high spring constant, high resonance frequency cantilevers resulting in improvements of both scan speed and resolution. Improving the smallest detectable amplitudes will allow a very local probing of the surface forces, resulting in higher resolution imaging. It has been shown previously [Fukuma05d] that improvements in OBD readout bandwidth that reach noise levels dictated only by the thermal oscillations of the cantilever are possible.

This thesis primarily aims at extending and improving AFM bandwidth and resolution in ambient conditions. Ultimately it would be desirable to obtain resolutions in ambient that rival low temperature vacuum based environments and the more recent tuning fork setups. The first part of this thesis explains the basic instrumentation of scanning probe microscopy, and the forces, interactions and detection techniques that are relevant for high resolution imaging. The next part of the thesis describes a novel beam deflection sensor, with which significantly higher band-

widths can be achieved, while maintaining very low noise levels. Theory suggests [Albrecht91] that increases in cantilever resonance frequencies can improve the thermal noise limitation of the cantilever by a significant factor as well as decreasing the response latency of the oscillating cantilever, thus allowing more rapid scanning. The following part describes the advantages and disadvantages of laser diode modulation, which is generally used to reduce laser diode mode hopping and noise in the optical path. The final part details the use of small dimensional, high frequency cantilevers, and shows a selected few high resolution images achieved with the complete novel microscopic system.

Chapter 2

Principles of Scanning Probe Microscopy

2.1 Scanning Probe Microscopy

Scanning probe microscopy (SPM) is an imaging technique in which the interaction between a sharp probe and a surface can be used to reveal properties of the surface. The probes or "tips" in use are generally manufactured to have an extremely sharp sphere as a terminal end, the radius of which can range from about 100 nm all the way down to a single protruding atom. Intuitively, when moving or scanning over a surface, these extremely sharp tips are capable of detecting surface contours and corrugations at an extremely high resolution; on many samples all the way to imaging individual atoms and, sample permitting, even covalent bonds. The area of competence of SPM is not limited solely to the surface topography of a sample, but can be used as a noninvasive way of measuring electrical, magnetic, chemical and material properties as well. This imaging power has made Scanning Probe Microscopy an indispensable tool for the physical, chemical and biological sciences and industry simultaneously.

The initial steps into SPM were taken by Young with the invention of the Topografiner [Young72], a device which used field emission of electrons between a conducting tip and sample to image the surface in a noninvasive manner. Although novel, due to the relative insensitivity of field emission the device was not able to deliver the results needed to catapult SPM to what it is today. However, Young suggested metal-vacuum-metal tunneling would result in a significant jump in sensitivity, but was unable to verify this, due to limitations with the mechanical design and the loop feedback electronics. It would take an additional decade of advances in engineering before the true breakthrough, Scanning Tunneling Microscopy, is discovered and implemented. In 1982, Binnig achieved the first successful combination of metal-vacuum-metal tunneling and probe scanning [Binnig82]. Shortly afterwards, the same group produced real space atomic

resolution images of a Si(111) surface in high vacuum [Binnig83]. Binnig and Rohrer quickly received the Nobel Prize in Physics in 1986, as STM research was undergoing a significant expansion.

2.2 Scanning Tunneling Microscopy

The principle of Scanning Tunneling Microscopy (STM) is straightforward. In classical physics an electron cannot pass a potential barrier if its energy is smaller than the potential within the barrier itself. However, quantum mechanics predicts an exponentially decaying electron wave-function within the barrier. In the case of the STM, two energy regions where electrons can travel freely, namely the tip and the sample, are separated by a potential barrier, consisting predominantly of a vacuum. As the tip approaches the sample, this potential barrier becomes increasingly narrower. When the tip is just a few Ångströms above the surface the exponentially decaying wave-functions will overlap, allowing the movement of electrons from one side of the barrier to the other, without passing over the barrier. If a small potential bias exists between the tip and sample, there will be a net flux of electrons through the barrier, which is known as the tunneling current, and is given by:

$$I \propto V \rho_s(0, E_f) e^{-1.025 \sqrt{\phi} d}, \text{ where } [d] = \text{Å}, [\phi] = \text{eV}; \quad (2.1)$$

where I is the tunneling current, V is the tip sample bias voltage, ρ_s is the local density of states (LDOS) around the sample's Fermi level E_f at the sample surface, ϕ is the barrier height, which is an average of the tip and sample work functions, and d the distance between the tip and the sample. The probability for tunneling is highest for electrons near the Fermi level E_f , where the barrier height is minimum. With normal work-functions around a few eV, a 1 Å decrease in tip sample distance will increase the tunneling current by almost one order of magnitude. This strong exponential relationship so close to the surface permits a very high vertical resolution, and in combination with proper feedback electronics allows one to lock the tip very close to the surface during scanning, maintaining a constant d , regardless of topography. In an ideal STM configuration V , ϕ , and d all remain constant; in such a situation the tunneling current I becomes a function of the local density of states, ρ_s .

2.3 Raster Scanning Technique

In Figure 2.1a, a simplified schematic of a typical STM is shown. The tip itself is generally a wire with a sharp tip manufactured by mechanical cleaving or chemical etching [Melmed91, Li-biouille95]. In this example the sample is fixated, and the tip is attached to 3 orthogonal piezo-electric transducers. These piezos allow the maneuverability of the tip in three dimensions, X, Y, and Z. In a raster scan, a larger area is subdivided into a sequence of horizontal scan lines, and each scan line is further subdivided into a series of pixels; the sum of all pixels of all scan lines will create an image of the original scan area. When the controller applies a saw-tooth signal to the X-piezo and slowly sweeps the y-piezo from one end of it's scan range to the other, a raster type scanning pattern is achieved, which is portrayed in Figure 2.1b. Forward and backward scan lines are usually distinguished from one another and recorded separately, creating two images. An alternative raster scanning technique is shown in Figure 2.1c, which is more precise than the method in Figure 2.1b due to the fact that the forward and backward lines are perfectly superimposed, but requires more advanced "closed-loop" piezo scanner technology. The Z-piezo, which has control over the vertical distance between tip and sample, is under full control of the proportional-integral (PI) feedback control loop. While the tip is scanning over the surface, the tunneling current observed by the current amplifier may deviate from the desired value due to a change in sample topography. The feedback control loop tries to correct this deviation and return the tunneling current to it's desired setpoint value by moving the z-piezo and thus adjusting the tip to sample distance, returning the tunneling current to it's desired value. Thus, by recording the position of the Z-piezo at each pixel in the raster image, a 3-dimensional image of the scan area can be created. This method of scanning is known as the constant current mode; ideal feedback control would always hold the current perfectly constant. An alternative method of scanning is the constant height or variable current mode. Here, the feedback control is switched off, keeping the tip at a constant absolute position above the sample during scanning. In this mode, images are acquired by recording the values of the tunneling current instead of the Z-position of the piezo. There are advantages in both modes of scanning; constant current mode produces images directly proportional to electron charge density profiles, while constant height mode overcomes the bandwidth and noise limitations of the z-piezo and feedback loop, allowing for faster scanning and potentially improved image resolution. It is important to note that if two different materials are present in the same sample, the tunneling current the tip experiences may be different due to a change in LDOS and barrier height from one material surface to another. Through this, the height information of the surface during constant current scanning may not be a direct representation of the topography, creating an artifact in the image.

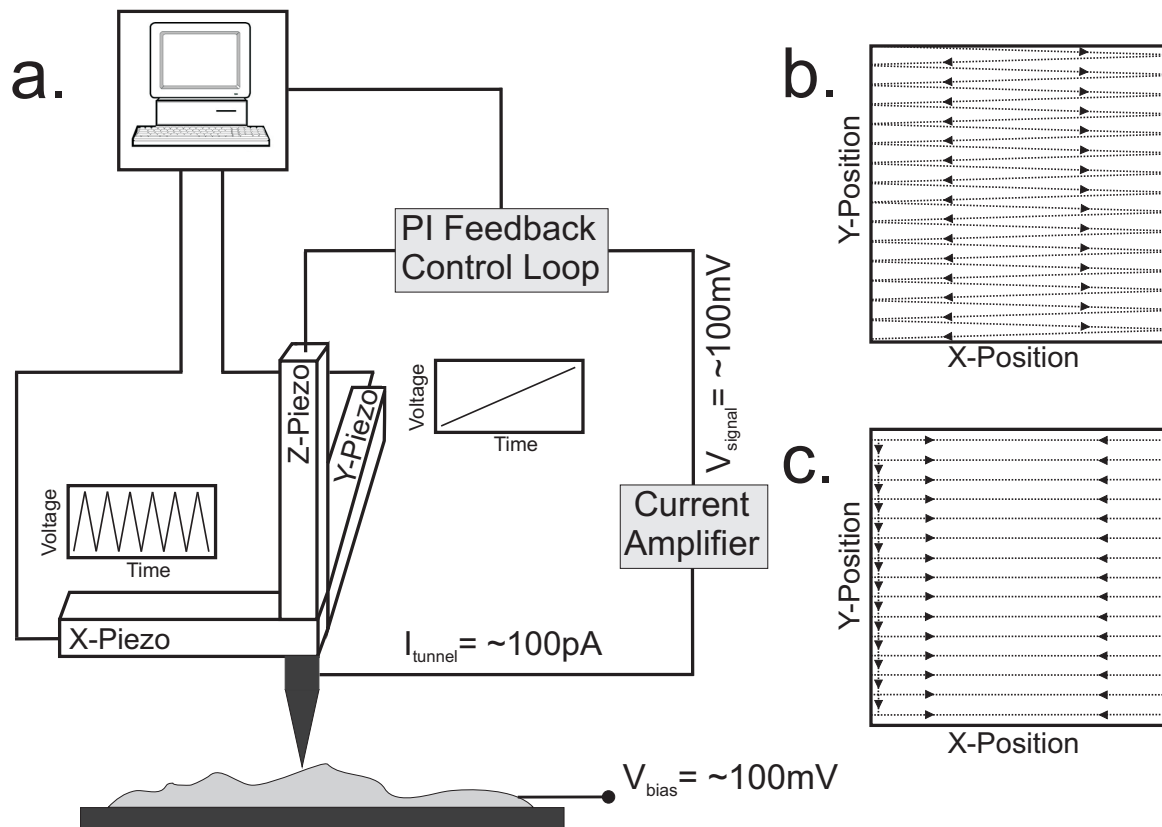


Figure 2.1: (a) Schematic drawing of the scanning tunneling microscope. A bias voltage V_{bias} is applied across the tip and sample, resulting in a tunneling current when the tip approaches the sample. The current intensity, equivalent to the tip to sample interaction distance, is controlled by the Z-piezo. The Z-piezo in turn is controlled by the PI feedback loop and the controller. In order to achieve raster scanning motion, a saw-tooth signal is applied to the x-piezo, while a lower frequency sweep signal is applied to the y-piezo; the combination of both piezos will move the tip over the sample in a zig-zag manner as seen in (b). An alternate scanning method where the forward and backward lines are superimposed is seen in (c). Typical values for tunneling currents are around the order of 100 pA , tip-sample bias voltages are around 100 mV and tip-sample distances around 5 \AA .

2.4 Resolution of the STM

As mentioned earlier, the atomic resolution capability of the STM achieved shortly after its invention is one of the most important achievements in surface science. According to Binnig, the smallest detectable resolution f of the STM is related by:

$$f \approx \sqrt{(r + d)l} \quad (2.2)$$

a combination of tip radius r , tip-sample distance d , and the decay length l of the interaction [Bin-

nig99, Tersoff83]. From the equation we can see that by reducing the tip radius and tip – sample distance, the smallest measurable resolution improves. Additionally, as mentioned previously, the strong exponential relationship between distance and tunneling current is synonymous with a very short decay length l , further adding to the resolution power of the STM. Interestingly, most successful STM tips are made of Tungsten, Platinum, Iridium, or combinations thereof. These d-band metals have a high density of partially occupied d-orbitals at their surfaces. Chen has suggested and calculated [Chen90] that the high resolution power of STM relies on the short decay length of quantum tunneling reducing the effective tip radius to a single d-orbital protruding from the very end of the tip. In Figure 2.2a a topography image (constant current mode) of freshly cleaved highly ordered pyrolytic graphite (HOPG) recorded on a tabletop STM in ambient conditions. The "honeycomb" like structure of the graphite lattice can clearly be seen, with lateral resolution around 1 Å.

The tip – sample interaction is fundamental for achieving excellent results in STM. It was quickly understood that in addition to measuring electronic structure due to induced tunneling currents, where electronic interactions take place close to the Fermi level, it would be interesting to study the tip – sample interaction forces as well, where interactions depend on the complete electronic band structure [Duerig86]. In addition, STM is limited to freely conducting tips and surfaces; an analogous system for insulating samples was not available [Hansma88]. With the invention of the atomic force microscope a new field of scanning probe microscopy was created, capable of measuring many types of interaction forces on a variety of different surfaces.

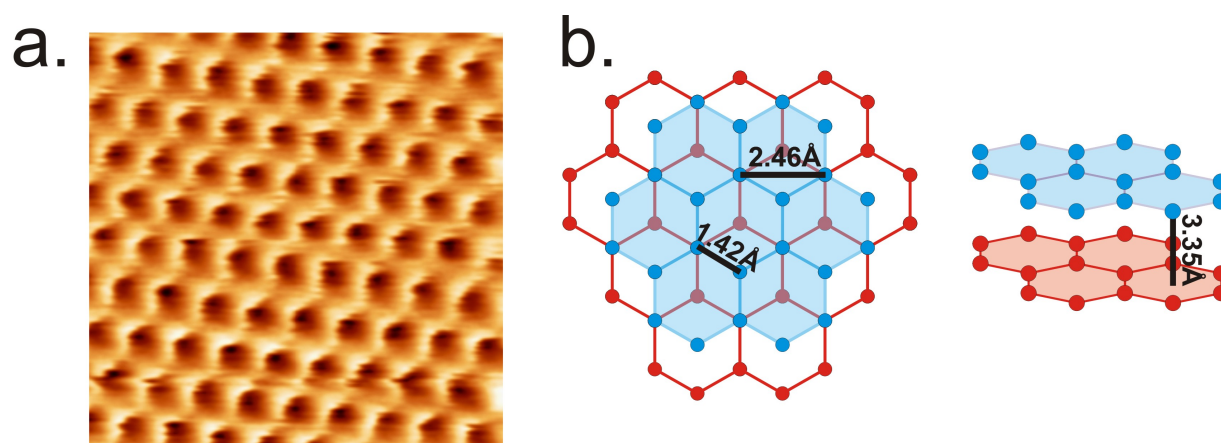


Figure 2.2: (a) The resolution power of STM on a surface of HOPG, an allotrope of carbon which forms ordered atomically flat sheet-like surfaces. A 2.0 nm x 2.0 nm scan of HOPG, acquired in constant current mode on a EasyScan using Pt/Ir tips (Nanosurf AG, Switzerland) with tunneling current $i = 1.0\text{nA}$, $V_{bias} = 80\text{mV}$ and tip speed 50 nm/s. The tips were prepared using the wire cutting method detailed in the EasyScan manual. The corresponding lattice constants of HOPG are shown in (b).

2.5 Forces

As the name suggests, the Atomic Force Microscope (AFM) is a device in which the relevant interactions between a tip and a surface consist of forces. There are many different forces that can be measured with an AFM, like contact forces, Van-der-Waals forces, electrostatic forces, capillary and hydration forces, frictional forces, and forces caused by chemical bonding [Israelachvili07]. Some forces are attractive, others repulsive; some are long ranged and are observable at larger tip–sample separations, others are short ranged and become relevant only at very small separations. The atomic force microscope is an extremely sensitive device for measuring forces. Detecting forces of 2×10^{-13} N are possible with routine cantilevers [Patil07], and forces down to 4×10^{-17} N have been measured with special cantilevers [Stowe97].

Contact Mechanics

The first analysis of contact mechanics is generally associated with Heinrich Hertz. Hertzian contact mechanics refer to the localized stresses that appear when two curved surfaces come in contact, deforming slightly under the imposed load. The Hertzian model [Hertz82] is a simple one, where repulsive forces dominate, and any attractive or adhesive forces are ignored. This is acceptable for larger objects where adhesive forces are relatively weak when compared to the rest of the system. However, the tip–sample interaction forces in scanning probe microscopy are sufficiently small for adhesive forces to become relevant. Two additional models attempt to take attractive forces into account: the Johnson-Kendall-Roberts (JKR) [Johnson71] and Derjaguin-Mueller-Toporov (DMT) [Derjaguin75, Muller83] models. The JKR model approximates the case of large, spherical tips on elastic samples with much adhesion, and in contrast the DMT model approximates the case of small, spherical tips on relatively inelastic samples with little adhesion. A fourth model, the Maugis model [Maugis92], is the closest approximation to the real situation; a combination of both JKR and DMT models, as they are opposite limits of the same theory. These models are extensively used in SPM where theoretical explanations of tip sample interactions are required.

2.5.1 Contact Forces

Contact between two different surfaces remains difficult to define. In scanning probe microscopy, atomic contact is commonly defined as the point where overlapping valence electron orbitals cause the first net repulsive forces on the tip as it approaches a surface [Goodman91]. Known as Pauli repulsion, these forces arise due to the requirement of anti-symmetry when electron orbitals are close enough to interact. Some electrons will be forced to assume a higher energy

state in order to satisfy anti-symmetry; the desire of the system to relax this energy back to the ground state results in a repulsive force. This force is extremely short ranged ($\approx 1 \text{ \AA}$), and thus only the surface atoms nearest to the tip are involved. Bader has stated that repulsion due to Pauli exclusion is a fictitious force; more truly overlapping electron orbitals can not properly screen nuclear charges anymore, leading to nuclear coulombic repulsion [Bader00, Bader06]. Nevertheless, the observed interactions are the same and follow the exponential potential estimation defined by Born-Mayer [Israelachvili07]:

$$F_{con} = Cbe^{-Cr} \quad (2.3)$$

where r is the distance between the two orbitals, b contains information on the number of electrons and their density, and C is the inverse of the radial "overlap" of the orbitals. b and C are generally found empirically.

2.5.2 Van-der-Waals Forces and the Lennard-Jones Potential

In addition to the short range repulsive forces detailed in the previous section, there is an additional force known as the Van der Waals force. This is the force that will cause noble gases to aggregate as they are cooled, and consists of 3 different multi-polar interactions that can take place: (i) forces due to permanent multi-pole orientations, (ii) forces due to a permanent multi-pole interacting with an induced multi-pole, and (iii) dispersion forces, where charge distribution fluctuations of an atom can instantaneously create multi-poles and interact with the same induced multi-pole on a neighboring atom. Van-der-Waals forces are significant for distances of a few Ångstroms to a few nanometers, and they can be attractive or repulsive (they are always attractive between identical atoms). The Van-der-Waals potential is given as:

$$U_{VdW}(r) = -\frac{A}{r^6} \quad (2.4)$$

The true intermolecular potential that takes place between two non-bonding atoms or molecules is often modeled as having an attractive and a repulsive term, the attractive term being the Van-der-Waals interaction, and the repulsive term due to contact or Pauli repulsion. Thus, combining both the Born-Mayer term and the Van-der-Waals interaction gives the Buckingham potential [Buckingham38]:

$$U_B(r) = be^{-Cr} - \frac{A}{r^6} \quad (2.5)$$

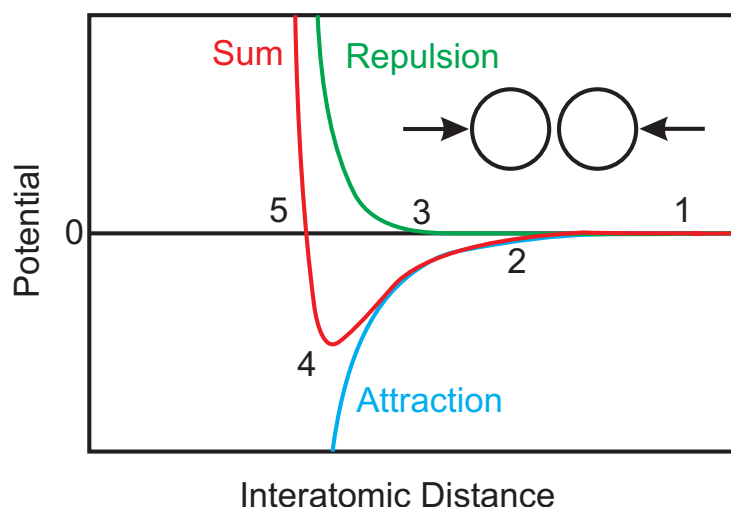


Figure 2.3: The Lennard-Jones Potential. Position 1: When two atomic objects are sufficiently far from one another, no interactions are observed. 2: As the two objects come closer, an attractive force (negative potential) begins to build up due to Van-der-Waals interactions. 3: The objects are close enough for repulsive forces to become relevant, however the total interaction is still attractive. 4: Repulsive contact forces are emerging more rapidly than attractive Van-der-Waals forces. The total sum reaches a potential minimum. 5: Repulsive contact forces become stronger than attractive Van-der-Waals forces. Further decreases in inter-atomic distance requires large amounts of energy (contact).

Alternately, it is common to use the 12-6 or Lennard-Jones potential [Jones24], which is given as:

$$U_{LJ}(r) = \frac{B}{r^{12}} - \frac{A}{r^6} \quad (2.6)$$

Here again, constants A and B are found empirically. The "brick wall" repulsive term r^{-12} of the Lennard-Jones potential is not very representative of the exponential nature of overlapping wave-functions [Abrahamson63], so it would be more empirically accurate to use the Buckingham potential function. However, the mathematical and computational efficiency of the Buckingham function is significantly reduced due to the exponential [White97], and thus the Lennard-Jones estimation remains popular.

Jump to Contact

Attractive forces like Van–der–Waals forces can sometimes cause undesired effects in SPM that can influence the performance of the tip–sample interaction significantly. Where attractive surface forces overpower the static spring force of the approaching tip, the tip will suddenly “jump–to–contact” with the sample [Hutter94, Tabor69]. In the case of snap–in due to Van–der–Waals when the lever spring constant is weak, the tip will come to rest at a distance equivalent to the potential minimum of the Lennard–Jones curve (area 4 of Figure 2.3). In the case of ambient environments, the unavoidable water films on the surface and tip can cause a powerful jump–to–contact due to capillary forces (see Section 2.5.4).

2.5.3 Electrostatic Forces

Electrostatic forces are long range forces between objects that take place when one object has a net charge relative to the other (coulomb interaction). Depending on the sign of the charges, these forces can be either attractive or repulsive; however in AFM these forces are usually attractive, and can be detected at tip sample separations up to a few micrometers, where the force is given by [Kalinin01]:

$$F_{elec} = -\frac{1}{2} \frac{dC(z)}{dz} (V_{tip} - V_s)^2 \quad (2.7)$$

where C is the induced tip–sample capacitance, z is the tip–sample separation, V_{tip} and V_s is the electric potential of the tip and surface, and F is the resulting force. It remains difficult to precisely calculate the capacitance, which is dependent on the geometry of the entire tip–sample interaction region, which can be micrometers in size due to the long range nature of electrostatic forces. Models exist that take into account a simple charge [Hu95b], a sphere [Terris89], a cone [Hao91] a spherical tip on the end of a truncated cone [Hudlet98], or the entire cantilever probe [Colchero01].

2.5.4 Capillary Forces

Where two solid surfaces come into close contact in ambient conditions, liquid menisci form due to capillary condensation of water. These liquid menisci cause an attractive force known as the capillary force, which for the geometry of a sphere on a flat surface is given as [Gao97]:

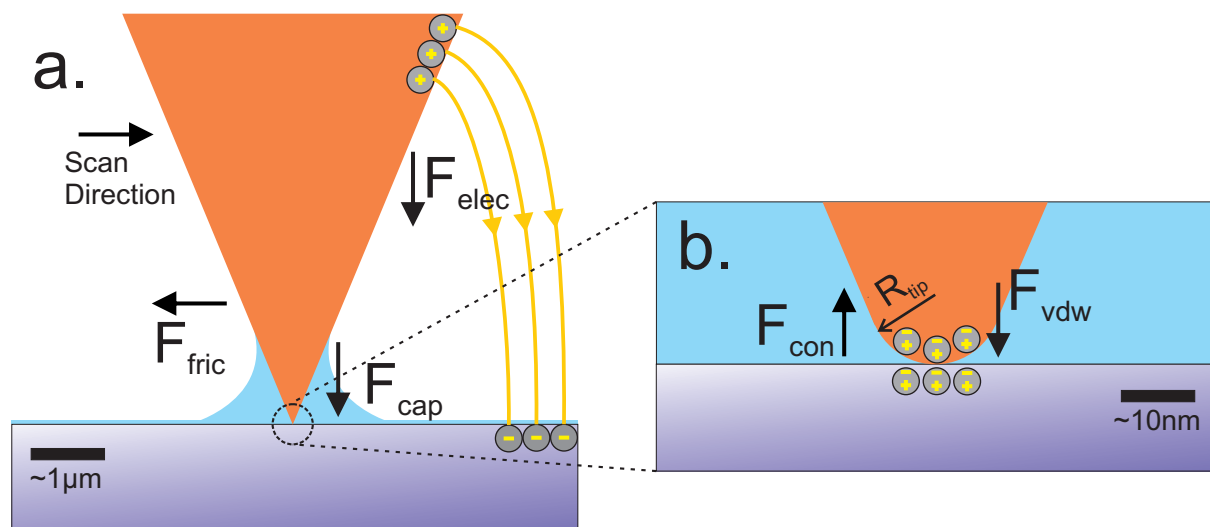


Figure 2.4: (a) Common long range interaction forces (scale bar $\sim 1 \mu m$). Charge imbalances or trapped charges in the tip and surface will cause electrostatic forces (usually attractive). Surface water will collect and form a meniscus with the tip, causing attractive capillary forces. Frictional forces appear in the opposite to tip motion when the tip is interacting with the surface. (b) Common interaction forces close to the sample surface (scale bar $\sim 10 nm$). Van-der-Waals forces induced by the dipoles in the tip and surface begin to interact a few nanometers from the surface. Contact is defined when strong repulsive forces appear between tip and surface. Tip radii R_{tip} are typically $\sim 10 nm$.

$$F_{cap} \cong 2\pi R \gamma_{LV} (\cos\theta + \cos\phi) \left(1 - \frac{dh}{dD}\right) \quad (2.8)$$

where R is the radius of the sphere, γ_{LV} is the liquid-vapor surface tension, θ is the contact angle of the sphere, ϕ is the angle of immersion relative to the normal of the surface, h is the immersion height of the liquid film, and D is the separation distance between sphere and sample. With larger spheres ($> 1 \mu m$ in size) the forces are humidity independent, as this equation suggests. As the size of the spheres are reduced, the humidity increasingly influences the capillary force [Pakarinen05, Kim10]. In addition, the precise geometry of the interface are not included in this calculation; deviations from the ideal sphere can alter the observed forces significantly [Butt08]. These liquid menisci can be burdensome for scanning probe microscopy imaging. The "jump-to-contact" effect detailed in Section 2.5.2 is also very relevant with capillary forces. In many cases the capillary forces outweigh the electrostatic and Van-der-Waals forces significantly, becoming the dominant factor in tip-sample adhesion [Tang01], reducing the force sensitivity significantly. However, it is difficult to avoid the formation of the menisci; it has been shown that even on extremely hydrophobic surfaces at least a monolayer of water will form [Wang10]. One solution is to image entirely in liquids, which Weisenhorn has shown will

lead to an increase in force sensitivity by a factor of 100 [Weisenhorn89], or to image in high vacuum environments ($< 1 \times 10^{-12}$ bar), where water films will not survive; these alternatives assume the sample under observation can withstand these environments. When imaging in liquid environments, any net surface charge that would normally cause long range electrostatic forces can be quenched by the counter ions in the buffer solution, if a buffer solution is used. In addition, depending on the pH and the salt concentration in the solution, the electrostatic interactions can be carefully balanced out [Butt91], which would improve imaging resolution.

2.5.5 Frictional Forces

When one surface is in contact and in motion relative to another, friction forces are resistive forces that always act in opposite direction of that movement. In basic physics textbooks it is simply calculated by multiplying the normal force (the force that holds the two surfaces together) by the coefficient of friction. These coefficients dictate the intensity of the frictional force, and are generally found empirically; they depend widely on the specific structure, chemistry and elastic properties of the surfaces, and the chemical environment in which the measurements are performed [Szlufarska08]. When two macroscale objects are in mechanical contact, a large sum of asperities on each surface in the interfacial region define that contact [Bhushan95]. Each single asperity interacts with the surface; the sum of all asperities will give the total macroscale frictional interaction. Scanning probe microscopy has created the possibility of studying the frictional interaction of a single asperity. The physics behind the single asperity frictional force is still widely debated; some results claim a linear relation between friction and tip-load (as on the macroscale) while others claim a sub-linear relation between the two [Szlufarska08, Mo09, Braun10, Wenning01]. What is generally agreed upon is that the frictional force is dependent on:

$$F_{fric} = \tau A(L) \quad (2.9)$$

where $A(L)$ is the interfacial contact area, τ is the interfacial shear strength, and L the load exerted by the tip. Carpick [Carpick99] derives a simple analytic equation to derive the contact area $A(L)$, where the Maugis model is used to fit the contact radius as a function of tip load. The interfacial shear strength τ represents the frictional force per interfacial atom, whose dependence on tip load is still under debate.

2.6 Atomic Force Microscopy

The Atomic Force Microscope (AFM) developed from the STM due to the desire to both accurately measure forces and scan non-conducting surfaces [Binnig86]. Similar to the STM, the AFM uses a raster scanning technique with piezoelectric transducers to move the tip relative to the sample (see Section 2.3). However, as the STM measures and uses currents for tip–sample feedback control, the AFM will measure tip–sample interaction forces, and use these as feedback control. In addition to ambient and vacuum environments, the AFM can also be used in liquid environments, which has developed it into a crucial device for biological research, achieving very high resolution imaging on biological samples [Müller95]. The first device consisted of a gold foil cantilever with a sharp diamond tip glued on. An STM tip was positioned right on top of the conductive cantilever, and STM feedback between the STM tip and the cantilever was used to measure and control the force between the cantilever tip and the sample. This setup was capable of achieving atomic resolution scanning on non-conductors [Albrecht87].

2.6.1 The Cantilever

In AFM, the predominant method of detecting tip-sample interaction forces is by attaching a sharp tip to a cantilever beam. Any interactions the tip may have with the surface will influence the mechanical behavior of the cantilever beam as well, whose motion can be easily detected using the optical detection methods detailed in Sections 2.6.2 and 2.6.3 below. AFM cantilevers are predominately made of Silicon or Silicon Nitride. Using common micromachining techniques [Bhushan07], these cantilevers can be manufactured with very sharp tips of just a few nanometers on their terminal end. Depending on their application, some cantilevers will have metal coatings on them; these coatings can be limited to the backside (the side opposite the tip) in order to improve reflectivity, or they can cover the whole cantilever and tip if special electrical or magnetic forces are to be analyzed.

Spring Constant

A cantilever can be modeled as a simple spring that is being compressed by an arbitrary force. When in the regime of elastic deformation, this force obeys Hooke's Law:

$$F_z = -k_z x \quad (2.10)$$

where the compression x of the spring is a direct measure of the force F_z related by the spring

constant k_z . The compression x is a quantity that can be measured with a very high precision (Section 2.6.3) making the force sensitivity very much dependent on the cantilever spring constants. The spring constant k_z is dependent on the material stiffness and the cantilever dimensions, and is given as [Sarid07]:

$$k_z = \frac{Ewd^3}{4l^3} = \frac{3EI}{l^3} \quad (2.11)$$

where E is the material dependent Young's Modulus, w is the width, d is the thickness, and l is the length. Since a cantilever can be considered as a beam with a rectangular cross-section, the width w and height d^3 can be rewritten as the area moment of inertia I .

Most AFM cantilevers are fabricated from Silicon or Silicon Nitride; this is predominately due to the simplicity and efficiency of micro-machining using Silicon-on-Insulator substrates. It is possible to create cantilevers with very small dimensions using this process [Hosaka00, Yang05]. However, small discrepancies and misalignments in the lithography steps give a considerable amount of uncertainty in the reproducibility of the intended cantilever. Additionally, it is difficult to control the thickness and uniformity of the backside reflective coatings [Butt05]. These margins of error have a profound effect on the spring constants of the cantilever, which can change significantly with small changes in the length and the thickness (as can be deduced from Equation 2.11). Webber showed that even cantilevers fashioned from the same wafer can have spring constant variations up to a factor of two [Webber08]. For this reason most manufacturers will give a very wide estimate as to what the true spring constant of their supplied lever(s) is, which often ranges an entire order of magnitude.

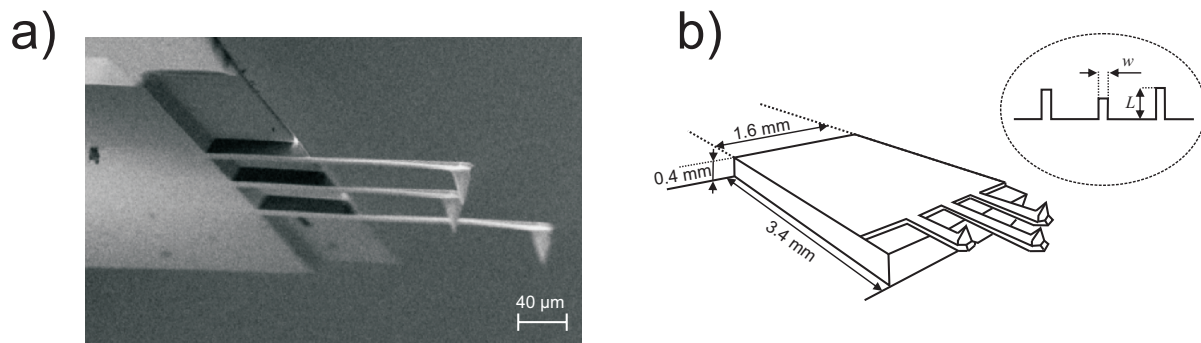


Figure 2.5: (a) Scanning electron microscope image of three different cantilevers (NSC35 series, Mikromasch, Tallinn, Estonia). Each cantilever has a slightly different length, resulting in different resonance frequencies and spring constants. (b) For handling purposes the cantilevers are attached to a bulk chip, whose dimensions are in the mm scale (based on image provided by Mikromasch).

Proper calibration of the spring constant is thus a necessary step for every cantilever that is used to quantify tip-sample interaction forces. The most common methods are: the reference beam method [Kim93, Torii96, Kim07], where the cantilever in question is exposed to a known force, for example when brought into contact and deflected by a calibrated reference beam. This method enjoys the highest precision, however is invasive and can potentially damage the cantilever or dull the tip. The Cleveland method [Cleveland93], where the frequency shift (and thus the spring constant) of the cantilever's fundamental eigenmode is measured when a known mass like a small spherical gold particle is intentionally added to the end of the cantilever. The thermal method [Hutter93], a very practical and non-invasive method where the intensity of the fundamental eigenmode's oscillations caused by thermal energy are measured. When the cantilever is modeled as a harmonic oscillator, it is possible to calculate the spring constant from the mean square deflection caused by thermal energy (See Section 5.1). Lastly the Sader method [Sader99], where the spring constant can be calculated when the fundamental eigenmode frequency and Q-factor of the oscillation are known, along with precise knowledge of the cantilever length and width.

A cantilever has 3 degrees of freedom; in addition to bending (z-axis), it can also twist (y-axis) and compress (x-axis). Each one of these motions has its own unique spring constant and equation of motion. The twisting motion of the cantilever can be measured using optical techniques (see Section 2.7.2) however the buckling of the compression motion is largely ignored.

Dynamic Behavior

In addition to the measuring the static deflections caused by forces acting on the tip and cantilever, it is possible to measure the dynamic behavior of the cantilever as well. In dynamic AFM, the cantilever is excited at or near its resonance frequency in order to induce an oscillation. The oscillation amplitude and phase can be measured in the same manner that the static deflections are measured (see Sections 2.6.2 and 2.6.3), provided that the oscillation frequency does not exceed the bandwidth of the detector. Dynamic AFM has the capability of being less invasive and destructive than static or "contact" AFM when operating on sensitive samples [Gotsmann99]. In addition, dynamic AFM has the ability to quantitatively characterize materials and material properties on the nanometer scale.

A dynamic cantilever is often considered as a damped and driven harmonic oscillator. In such a case the motion of the cantilever is a function of time. A realistic description of cantilever tip movements is given by Newton's equation of motion [Sarid94]:

$$F(t) = m^* \ddot{X}(t) + \gamma_D \dot{X}(t) + k_z X(t) \quad (2.12)$$

where $F(t)$ is the externally applied force, k_z is the spring constant as seen in Equation 2.11, γ_D is the damping coefficient, and the effective mass m^* is defined as:

$$m^* = 1.24(wdl\rho) + m_t \quad (2.13)$$

where wdl is the volume of the cantilever times the material density ρ (effectively the mass of the cantilever) and m_t is the mass of the tip. Any movement caused by the external force $F(t)$ is considered to be in the normal direction. If the applied excitation force $F(t)$ is of sinusoidal form, like

$$F(t) = A_{ex}\cos(\omega t) \quad (2.14)$$

then the steady state solution to the differential equation 2.12 is sinusoidal as well and given as:

$$X(t) = A_0\cos(\omega t + \phi) \quad (2.15)$$

where A_0 is the effective amplitude of the oscillation, ω is the angular frequency and ϕ is the phase difference to the excitation signal. For the case of an undamped cantilever the constants m^* , and k_z are the elementary parameters of the cantilever motion. From these values one can deduce the frequency of the first fundamental eigenmode of the cantilever beam:

$$\omega_0 = \sqrt{\frac{k_z}{m^*}} \quad (2.16)$$

where ω_0 is the fundamental angular eigenfrequency. Common eigenfrequencies of commercially available cantilevers range from a few kHz all the way to the low MHz range. In the case of a cantilever in vacuum, the cantilever's harmonic motion is damped only by its own internal dissipation, and thus equation 2.16 holds relatively well. The predominant form of damping outside a vacuum is caused by the fluidity of environments such as water or air. In these environments it becomes increasingly more difficult to predict the exact eigenfrequency of the cantilever, due to a frequency dependent virtual mass that is added to m^* caused by the hydrodynamic drag of the media [Walters96, Elmer97]. One can say that the added mass is always positive, resulting in a negative shift in frequency as the viscosity of the media is increased.

The Q-factor is a dimensionless parameter that quantifies the rate of energy loss through damp-

ing of the oscillation. Oscillations that have heavy damping will have low Q-factors, meaning that the oscillation will die out very quickly (like a pendulum oscillating in oil) while oscillations that have low damping will have very high Q-factors, and will ring considerably longer before stabilizing. The quality factor Q of the oscillation is defined as:

$$Q = \frac{m^* \cdot \omega_0}{\gamma_D} \quad (2.17)$$

One can use the Q-factor to calculate this time τ it will take an oscillation to stabilize:

$$\tau = \frac{2Q}{\omega_0} \quad (2.18)$$

In vacuum Q-factors of cantilevers can reach values of 50,000 or more for common cantilevers at typical resonant frequencies of ~ 100 kHz [Yang00]. This results in a relatively long transient response time of ~ 30 ms which can limit the possible operational modes and scanning rates of AFM in vacuum (see Section 2.7.4). In air, the Q-factors will drop to ~ 100 , dropping the response time likewise. In liquid environments the Q values can drop ~ 10 making the cantilever response even faster.

The amplitude response A_0 of a cantilever to the excitation of equation 2.14 as a function of frequency ω is given as:

$$A_0(\omega) = \frac{A_{ex} \cdot Q \cdot \omega_0^2}{\sqrt{\omega^2 \omega_0^2 + Q^2 (\omega_0^2 - \omega^2)^2}} \quad (2.19)$$

and the phase shift φ between the excitation signal and the cantilever steady state is:

$$\varphi(\omega) = \arctan\left(\frac{\omega \cdot \omega_0}{Q(\omega_0^2 - \omega^2)}\right) \quad (2.20)$$

As can be seen in Figure 2.6 and Equations 2.19 and 2.20, the amplitude response is near zero for frequencies significantly below ω_0 ; likewise the phase shift is zero in this area. As ω begins to approach ω_0 , the amplitude response will increase, peaking when $\omega = \omega_0$. Similarly, at this point the phase will have increased to exactly 90 degrees. As ω passes the resonance peak ω_0 , the amplitude will again begin to drop, returning to near zero for frequencies significantly above ω_0 ; the phase will continue to increase, peaking at 180 degrees for large ω .

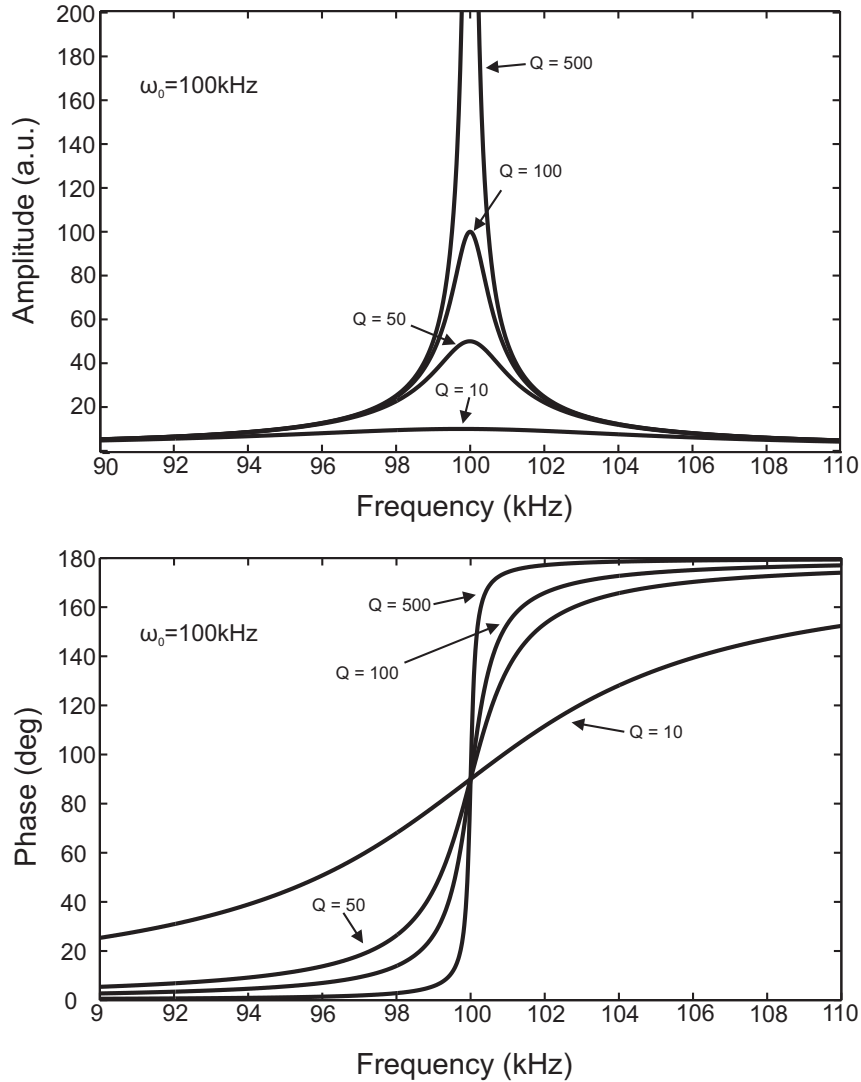


Figure 2.6: Amplitude and phase response of a hypothetical cantilever with resonance frequency ω_0 at 100kHz for a variety of different Q-values. At resonance, the phase offset is always 90 degrees. As the Q value increases, the slope of the phase curve through ω_0 is increasingly steep.

When the cantilever experiences no external forces except for the excitation, the externally applied force of equation 2.12 is directly equal to the dynamic force of excitation. However, when the cantilever is exposed to external forces, for example when the tip and sample interact, the externally applied force becomes:

$$F(t) = F_{ex} + F_{ts} \quad (2.21)$$

where F_{ex} is the excitation force, and F_{ts} is the tip-sample interaction force. When a tip-sample interaction force is present in the system, the fundamental resonance frequency ω_0 of the sys-

tem will shift as well. Attractive interaction forces will shift ω_0 to a lower frequency, while repulsive forces will shift the resonance peak to higher frequencies, as can be seen in Figure 2.7. If the excitation frequency ω (see Equation 2.14) does not follow ω_0 , the free amplitude A_0 will quickly drop due to these shifts in resonance.

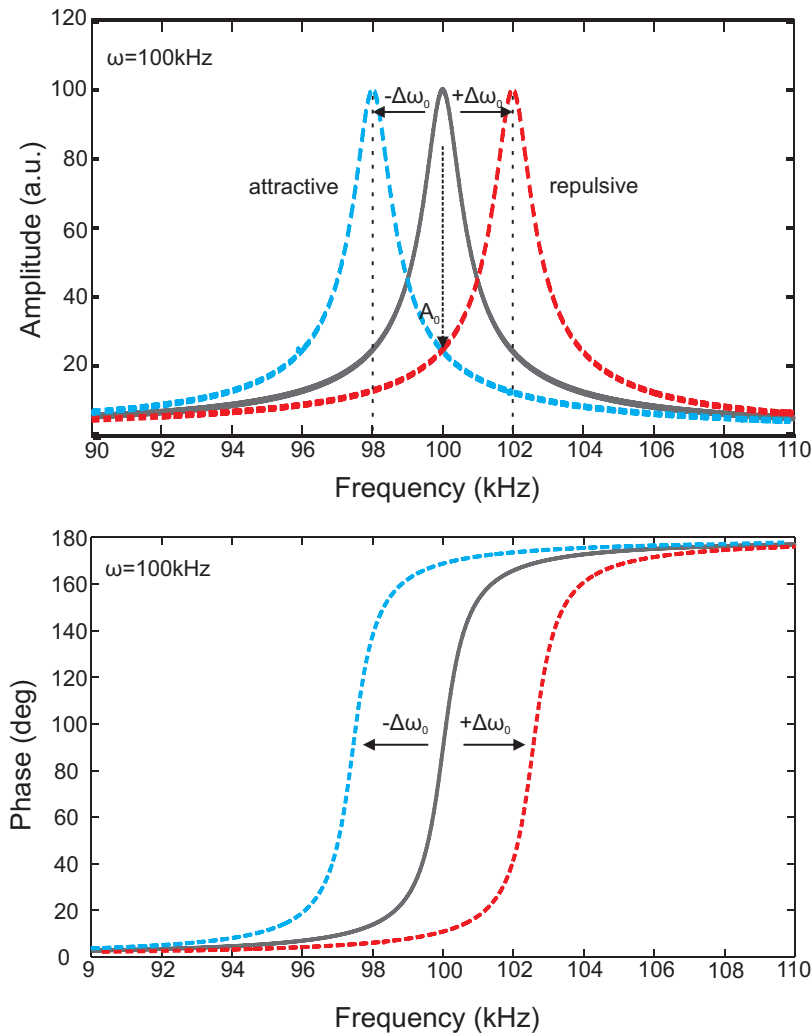


Figure 2.7: Schematic representation of the force dependence on the amplitude and phase of an oscillating cantilever. Attractive external forces will reduce the ω_0 of the system (blue curve) while repulsive forces will increase ω_0 (red curve). Amplitude A_0 will quickly drop to a lower value if ω does not follow the movement of ω_0 .

Sader devised a method to directly calculate the tip-sample interaction force from the frequency shift $\Delta\omega_0$, regardless of the oscillation amplitude [Sader04]. Frequency modulation AFM, a powerful and commonly used control technique, detects and utilizes these force dependent frequency shifts in order to achieve very high resolution topographic imaging (see Section 2.7.5).

2.6.2 Interferometric Detection

Nevertheless, it was quickly observed that replacing the STM tip with a laser interferometer would have advantages. Martin published the first scanning probe microscope with heterodyne interferometric deflection detection [Martin87], citing that interferometry is insensitive to lever surface roughness, is simpler to implement, and is less sensitive to thermal drifts. Coincidentally since the device was a heterodyne interferometer, Martin was also the first to suggest measuring the cantilever amplitude and phase, which would result in an alternate method of tip-sample distance control (amplitude modulation) and that frequency shifts of the oscillating system would be a sensitive indication of tip-sample interaction forces (see Section: 2.7). Shortly afterwards, Rugar created the first interferometric SPM detector capable of measuring DC deflections reliably as well [Rugar88, Rugar89]. In this approach, a laser light source is passed through a halfwave plate into a polarizing beam splitter. Half of the light is then focused into a single-mode fiber-optic cable, the end of which is placed over the cantilever at a distance of a few micrometers, focusing the beam onto the back of the cantilever. The incident beam is reflected by the cantilever, returned to and recaptured by the fiber, after which it passes back to the beam splitter. Here it recombines with the light originally separated by the beam splitter, where cantilever deflections create a measurable interference pattern when the light intensity is measured by a photodiode. Although this beam deflection technique is the most sensitive technique used in AFM today (see Section: 2.7.7), the sensitivity of optical beam deflection should be equal [Putman92b] or significantly better [Ng07] than interferometric detection.

2.6.3 Optical Beam Deflection

Next to interferometric detection, Optical Beam Deflection detection (OBD) is an alternate method of deflection detection. In OBD, an incident light beam is focused onto a reflective surface. The resulting reflected beam is monitored by a Position Sensitive Detector (PSD), a precision photosensitive device capable of detecting small displacements of that incident laser beam. The sensitivity of the cantilever displacement in relation to the signal generated by the Position Sensitive Detector is referred to as the Optical Lever Sensitivity, and is usually given in $\frac{V}{nm}$. Before the advent of atomic force microscopy, optical beam deflection was used to detect sensitive surface shifts caused by photothermal expansion [Olmstead83], and shown that deflections of just a few picometer could be detected [Amer86]. Meyer extended it to AFM [Meyer88], citing the sensitivity and simplicity of setup (in vacuum as well as ambient) as the greatest advantages. This proved to be a correct assumption, as most AFMs constructed today are based on the OBD detection technique. A schematic of a typical beam deflection setup is seen in Figure 2.8. When the cantilever is displaced along the z-axis, the spot will move vertically on the photodiode. This movement is termed vertical deflection. If the spot moves laterally across the photodiode, this

movement is termed horizontal deflection.

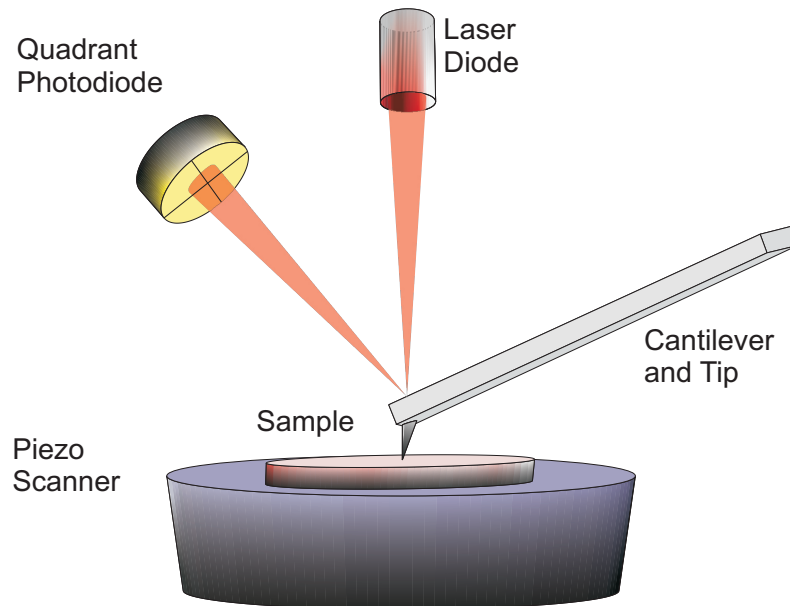


Figure 2.8: Schematic of a typical optical beam deflection based AFM. Light originating from a laser diode is focused onto the backside of a cantilever, which is then reflected and directed onto a quadrant photodiode. The quadrant photodiode has the capability of detecting the exact position of the incident light, and thus the behavior of the cantilever can be recorded. In this schematic, movement by the piezo scanner in the X, Y, and Z dimensions is executed through the sample, while the tip remains stationary.

Light Source

Numerous light sources have been used for optical beam deflection AFM. Originally, Meyer used a Helium-Neon laser, however this was quickly abandoned due to the vibrations caused by the large mechanical loop that is created between tip and sample when the relatively bulky He-Ne tube is attached to the optics. Semiconductor diode lasers were used in place [Meyer90]. Diode lasers have the advantage that they are small and can be easily incorporated into a compact optical system, have a wide spectral range in the visible and infrared from which to choose a particular wavelength, and have a wide range of laser intensities from $\sim 100 \mu\text{W}$ to 100 mW. Diode lasers are monochromatic, resulting in a relatively long coherence length (up to 20 cm); they are also prone to intensity and pointing noise, due to thermal fluctuations and optical feedback. More recently super-luminescent light emitting diodes (SLD) have been used as light sources as well [Budakian02, Geisse09]. SLDs have a shorter coherence length when compared to conventional laser diodes, which reduces the difficulties associated with potential

unwanted interference. Due to their parasitic lasing and thus rapid death when exposed to back reflections, SLDs have to be properly shielded so that no light may be permitted to re-enter the cavity [Alphonse02]. This significantly improves the stability of the output light, reducing the transient noise that can occur with conventional laser diodes.

Bi-cell and Quadrant Photodiodes

The first successful beam deflection sensors used consisted of bi-cell photodiode monitoring the position of the incident beam [Alexander89]. Bi-cell detectors are silicon photodetectors consisting of two separate photodiode elements separated by a small gap (usually between 10–100 μm in width). These two elements are generally masked onto a common substrate where the cathode is shared, and each element has a separate anode. A light spot that illuminates a single element is photoelectrically characterized as being only in that element. Thus, as a light spot translates across the detector from one element to another, the electrical energy generated by one element is proportional to the incident light. The difference in electrical contribution of the two segments will define an exact position of the incident laser beam- relative to the center of the device; i.e. the vertical and horizontal deflections. This can be achieved with a small amount of analog electronics which will subtract the one signal from the other, and outputting the final signal as a voltage. These calculations work well at DC and medium frequencies, in some cases reaching a few MHz (see Section 2.7.7). The first applications of bi-cell photodiodes as position sensors was with photothermal deflection spectroscopy [Boccaro80], a technique where the change in refractive index of a medium can be measured with high precision.

Characteristic to every photodiode is the parasitic junction capacitance in parallel with the generated photocurrent. This capacitance, due to the stored charges that exist outside of the depletion region, dominates the high frequency performance of the detector system, and is dependent on the surface area of the photodetector [Graeme96]. If the detector allows the use of reverse biasing, this can reduce the junction capacitance by as much as 7–10 times. Biasing will increase the width of the depletion region, thus increasing the width of the hypothetical parallel plates on which this capacitance is based.

Similar to the bi-cell photodiode, the quadrant photodiode consists of four independent elements instead of two. The quadrant photodiode has the advantage of being able to detect deflections in two independent dimensions, adding to the information that can be recorded on cantilever behavior [Marti90]. It is the quadrant photodiode that enabled Frictional Force Microscopy (see Section 2.7.2) and the device present into most beam-deflection AFMs today.

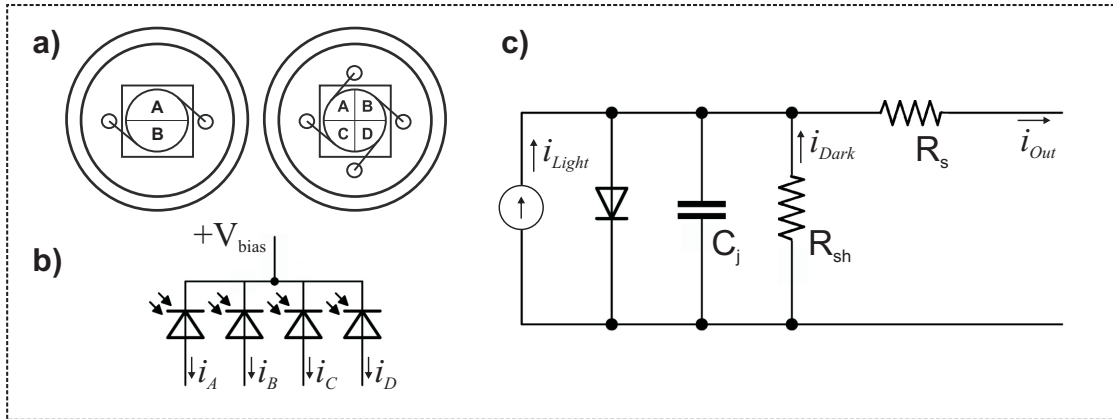


Figure 2.9: (a) Schematic of a typical bi-cell and quadrant photodiode. (b) Equivalent circuit of a quadrant photodiode; each segment A,B,C and D are unique photodiodes, outputting a light intensity dependent currents, i_A to i_D . (c) Equivalent circuit of a single photodiode, consisting of: the signal current i_{Light} in parallel with an ideal diode, the capacitance of the photodiode C_j (resulting from stored charges on the junction, value depends on bias; usually 10-100 pF), the shunt resistance R_{sh} (usually $> 100M\Omega$) and the resulting dark leakage current i_{Dark} , and the series resistance R_s (usually $< 100\Omega$).

Analog Signal Arithmetic

As mentioned in Section 2.6.3, in order to evaluate the vertical or horizontal deflections, a small amount of analog signal processing has to be conducted. This analog signal processing is entirely arithmetic, and equates to:

$$Vertical = \frac{A - B}{A + B} \quad (2.22)$$

for the bi-cell photodiode, and:

$$Vertical = \frac{(A + B) - (C + D)}{A + B + C + D} \quad (2.23)$$

$$Horizontal = \frac{(A + C) - (B + D)}{A + B + C + D} \quad (2.24)$$

for the quadrant photodiode, where signals A , B , C , D equate to the electrical contributions of each photodiode. The common cathode design of the quadrant and bi-cell photodiodes prohibits the direct connection of anode-to-cathode, i.e the diodes cannot simply be placed in parallel in order to compute the deflection; an analog processor is required. The schematic of a very common analog arithmetic processor for a quadrant photodiode is shown in Figure 2.10.

As the signal originating from any photodiode is an photo-intensity dependent current, all the outputs of the quadrant photodiodes are currents. These current signals are initially converted to voltage signals in the transimpedance stage; the arithmetic calculations of these voltages is subsequently done in the first (addition) and second (subtraction) arithmetic stages, using common operational amplifier layouts [Sedra09]. The sum of all four quadrants is extracted as well, as this delivers information on the stability of the light source and the sensitivity as a whole. It is common to divide the vertical and horizontal deflections by this sum, as shown in the Equations 2.23 and 2.24. If the light source is unstable, the normalization of these resultant signals is necessary to cancel out the effects of a varying source intensity, which might otherwise be falsely deemed an apparent shift in the spot position.

In many AFM setups it is common to physically separate the initial transimpedance or "preamplifier" stage from the rest of the arithmetic processor [Fukuma05d, Torbrugge08], connecting the preamplifier to the quadrant photodiode physically near. This is due to the assumption that currents are more susceptible than voltages to signal damaging interference originating from stray electromagnetic fields or parasitic leakage currents, resulting in the need to convert the signal to a voltage as quickly as possible.

2.7 Scanning and Control Techniques

Since the invention of AFM, various modes of operation have been introduced to specifically probe and sample variety of different characteristics with nanometer or even sub-nanometer resolution. These control techniques all aim to regulate the tip to sample interaction, ideally non-invasively and with a high precision, and generate contrast, whether it is of topographical, electrical, magnetic, or chemical nature. Such control techniques include (but are not limited to): contact mode scanning, frictional force microscopy, amplitude modulation (AM) scanning, and frequency modulation (FM) scanning. All techniques will scan a surface by using piezoelectric transducers (scanners) and typically PI control loops as discussed with the STM (Section 2.3). Fundamentally important to the operation of AFM are lock-in amplifiers and phase locked loops, whose operational concepts are discussed briefly.

Lock-in Amplifier

The lock-in amplifier, also known as a phase sensitive detector, was invented by Robert Dicke in 1946 as a technique to measure thermal radiation and atmospheric absorption at microwave frequencies using a measurement antenna and a corresponding "dummy" antenna [Dicke46a, Dicke46b]. The power of this device is that it can successfully extract a signal of a previously determined reference frequency from an extremely noisy input environment. This is achieved

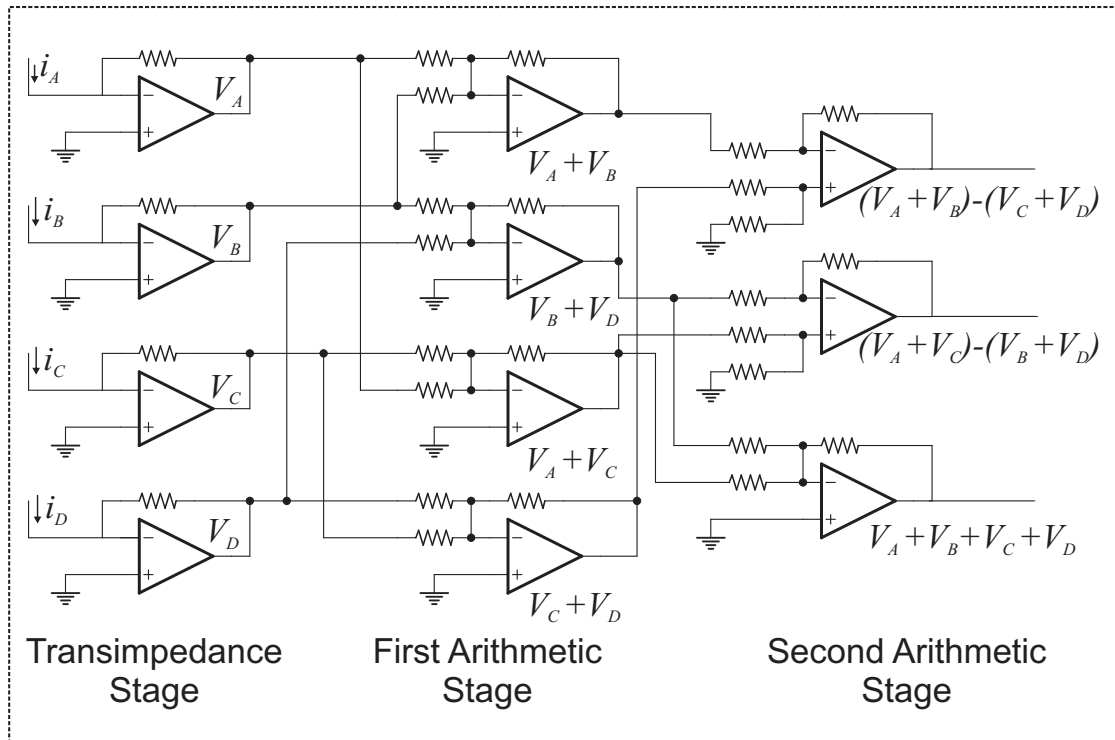


Figure 2.10: A typical voltage mode readout for two channel optical beam deflection, with photocurrents i_A to i_D originating from a quadrant photodiode. All outputs are voltages, all inputs are currents. The transimpedance stage converts the laser intensity dependent photocurrent into a voltage. The first arithmetic stage will add two relevant quadrants together. The second arithmetic stage will then conduct the necessary subtraction in order to arrive at the vertical and horizontal deflections. Additionally, the second arithmetic stage will also compute the sum of all four photocurrents. If required, the division stage comes after the second arithmetic stage (not shown).

by multiplying the noisy input by the clean reference signal, which will produce two DC outputs (i) whose value is proportional to the amplitude of the reference frequency signal of the noisy input, and (ii) the phase difference between the reference signal and the signal in the noisy input (for more information see [StandfordResearch]).

Phase Locked Loop

A phase locked loop is a device which will attempt to synchronize two separate oscillations, i.e. will try to synchronize the device's output oscillation with an input oscillation. The device compares the phase of the input signal (which is often demodulated by a lock-in amplifier) with the phase of the internally generated output signal, and locks this phase difference by adjusting the oscillation frequency of the output signal. In an ideal PLL, the frequency of the output signal

will thus always follow the frequency of the input signal perfectly, holding the desired phase offset.

2.7.1 Force Distance Curves

Force distance curves, also known as "approach and retract" or "Z-spectroscopy" curves, are used to evaluate the response of the cantilever as a function of the tip-sample separation distance. These curves give a wide variety of information; they can be used to locally probe the elasticity and mechanical properties of a surface, to recover the complete tip-sample interaction energy [Schwarz97], to characterize and measure bond-strengths of tip-functionalized biomolecules [Ando01], to characterize chemical and material contrasts by evaluating the interaction potential, to use the precision of the Z-piezo to calibrate optical lever sensitivities [Hutter93], and to find the optimal region for the setpoint of the Z-controller before initiating a scan. Generally the X and Y scanners are stationary, only the Z scanner is used to approach the tip to the surface. In Figure 2.12a, the behavior of the vertical deflection during an approach (blue curve) and retract (red curve) of a non-oscillating cantilever is recorded. At point 1, no tip-sample interactions are experienced. At point 2, the cantilever begins to experience surface forces, which will start to bend the cantilever as it further presses onto the sample. At point 3 the measurable deflection reaches a maximum due to the range limit of the readout at -5V. Shortly after this point the direction of motion reverses, and the tip will begin to retract from the surface. At point 4 the attractive forces between the tip and the sample are strong enough to pin the tip to the sample, until the recoil of the cantilever separates the tip from the surface and the cantilever returns to its principal relaxed position.

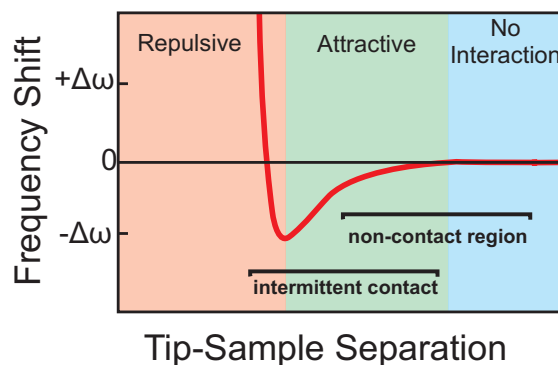


Figure 2.11: Operating regions of FM-AFM. The forces experienced by the tip when approaching the surface are correlated with the interaction potential, like the Lennard-Jones potential. Blue region: tip and sample are too far apart, cantilever oscillation experiences no external forces and thus no frequency shifts. Green region: non-contact operation. Negative interaction potential results in attractive tip-sample forces, and thus negative frequency shifts. Red region: Positive interaction potential results in repulsive forces and thus positive frequency shifts.

The dynamically actuated cantilever is more complicated when approaching a surface. Figures 2.12 b and c show the behavior of the oscillation when the tip approaches and retracts from the surface. At first the amplitude drops linearly from point 1 as the tip approaches, with a sudden jump in amplitude at point 2. Similarly at point 2, the phase suddenly jumps from a negative value to a positive one. At point 4 on the retract curve, the amplitude and phase will return to their original values before the surface approach.

These jumps can be attributed to the fact that there are two separate stable solutions to the harmonic oscillator when confronted with a non-linear interaction potential, like the Lennard-Jones potential. This effect has been termed bi-stability, and can cause unwanted chaotic artifacts in AFM images [Stark10]. Initially, the cantilever only experiences attractive forces (like in the green region of Figure 2.11) which will initially lower the phase offset. This region is known as the attractive regime. Once the oscillating cantilever is close enough to the sample, repulsive forces will dominate, causing the phase and amplitude to jump to a different, stable value; this region is known as the repulsive regime. In the attractive regime, a negative average interaction force dominates the amplitude reduction while in the repulsive regime a positive average interaction force dominates [Garcia99, Garcia00]. It is important to note that unbalanced charges between tip and sample can cause electrostatic forces that may influence cantilever behavior far from the surface of the sample. Ideally, such forces can be compensated by applying a potential on either the sample or the tip which acts to cancel the electrostatic force [Ziegler09] and can remove a significant amount of unwanted artifacts while imaging [Ziegler07]. Additionally, resonance frequencies can shift significantly when approaching a surface with the cantilever due to the effective "added mass" effect of the squeezed film between the cantilever and the sample [Naik03].

2.7.2 Contact Mode and Frictional Force Microscopy

When the cantilever tip approaches and contacts a surface, any forces the tip may experience (like those detailed in Section 2.5) will influence the mechanical behavior of the cantilever beam. In the case of contact mode scanning, the tip is brought so close to the surface that direct, repulsive contact dominates the observed forces. The entire cantilever will deflect, causing a measurable vertical deflection of the reflected optical beam on the quadrant photodiode. This effect is seen in Figure 2.13. This vertical deflection is directly proportional to the force applied to the surface by the cantilever; by holding a particular vertical deflection constant, the force the tip exerts on the sample is held constant as well. It is understandable that contact mode scanning is often referred to as "constant force" mode scanning. Thus, by holding the tip-sample force constant through a PI control loop when scanning over the sample surface, an exact image of the topography of a surface can be obtained.

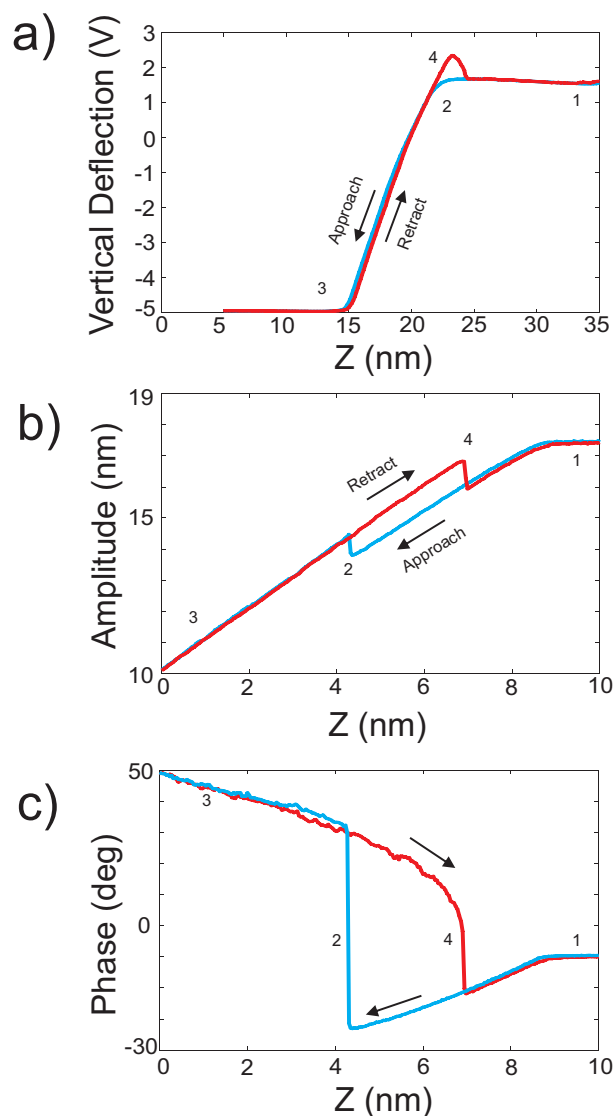


Figure 2.12: (a) Force distance curve of a static cantilever approaching (blue) and retracting (red) from a surface. At 1, the tip comes into contact with the surface. Continuing the approach will cause strong contact forces between the tip and the sample, causing the entire cantilever to deflect; a linear approach causes a linear deflection of the optical beam and thus a linear change in the vertical deflection signal. (b) and (c) When the cantilever is dynamically oscillated at an eigenmode, the amplitude will drop as the surface is approached, and the phase will decrease similarly. When repulsive forces start to dominate the interaction, the phase will jump to a positive value, and the amplitude will jump slightly in magnitude.

When a cantilever is scanning over a surface in contact mode, frictional forces can cause the cantilever to twist torsionally, as can be seen in Figure 2.13. These torsional movements will cause a horizontal deflection of the incident optical beam on the quadrant photodiode, resulting in information about the frictional behavior between the tip and the sample being recorded in addition to the topographic information from the regular contact mode scan. This technique is

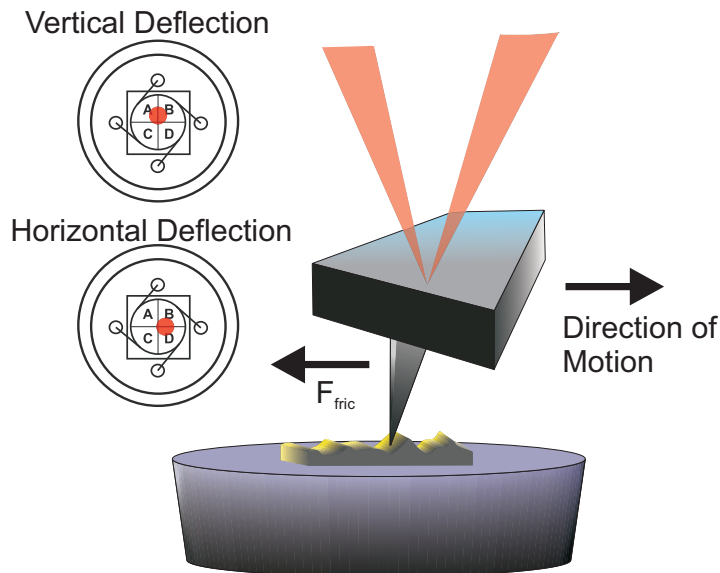


Figure 2.13: Schematic of a cantilever exposed to frictional forces as a result of motion over the surface while in contact. The frictional force causes a torsional twisting in the cantilever, which will cause the reflected laser beam to deflect horizontally on the quadrant photodiode.

known as Frictional Force Microscopy (FFM). The lateral forces measured can exhibit atomic-scale features, following lattice periodicity caused by stick-slip effects [Gnecco00, Medyanik06]. FFM is also capable of detecting regions of material and chemical contrast, due to different adhesion and interaction forces between the tip and the different chemical domains [Baralia06].

2.7.3 Cantilever Actuation

When the fundamental eigenmode of a cantilever is within the bandwidth of the quadrant photodetector and analog processor, the oscillation of a cantilever can be detected on the vertical deflection. The cantilever oscillation has to be induced by an external force, as mentioned in Section 2.6.1. This can be achieved in a number of ways; the most common method uses a small "dither" piezo located near the cantilever, onto which an electrical excitation signal of frequency ω_0 is applied. The resulting piezoelectric vibration propagates to the cantilever, inducing the oscillation. This is simple and non-invasive technique, however the response of the piezo is limited to just a few MHz in bandwidth, suffers from spectral non-linearity, and can induce additional, distorting oscillations when used in liquids, commonly known as "the forest of peaks" [Schaeffer96, Kokavecz07]. Additionally, a cantilever can be magnetically activated in order to induce an oscillation in an alternating magnetic field [Han96]. This magnetic actuation is usually done by adding a magnetic coating or attaching a magnetic particle to the end of the cantilever, from which the force of oscillation will originate. This technique is often used

in connection with biological samples in liquid environments [Ge07]. Alternately, a cantilever can be actuated using a second, intensity modulated laser beam [Fukuma09, Nain10, Ratcliff98, Umeda91]. The intensity modulated beam causes a local thermal heating of the cantilever, causing a mechanical distortion that will again induce an oscillation when actuated at ω_0 . Advantages of this technique include a significantly wider excitable bandwidth beyond just a few MHz and avoidance of the "forest of peaks" problem. See Chapter 8 for a more detailed analysis and applications of optical cantilever actuation.

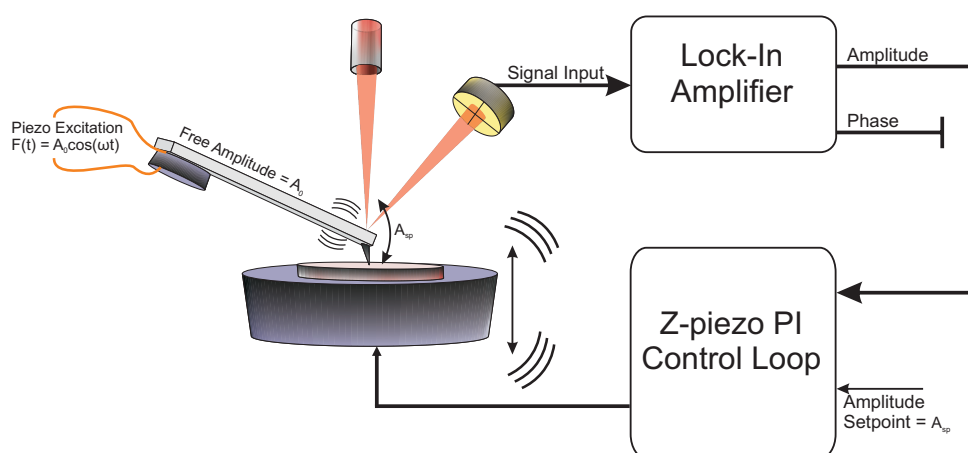


Figure 2.14: Principle of an AFM in the amplitude modulation control configuration. The excitation source is a dither piezo. The effective oscillation amplitude is recorded by the beam deflection sensor and subsequently rendered by the lock-in amplifier. The lock-in feeds the amplitude signal to the Z-dimension PI controller, which attempts to hold the true amplitude equal to the setpoint by moving the position of the z-piezo relative to the cantilever.

2.7.4 Amplitude Modulation

Amplitude modulation AFM (AM-AFM) or "tapping mode" is a technique in which the oscillating cantilever is used to scan over the surface in order to map the sample topography. This technique is relatively easy to implement, and significantly less invasive than contact mode scanning due to the elimination of lateral and frictional forces [Gotsmann99]. In order to avoid jump-to-contact, cantilevers operating in amplitude modulation are usually vibrated at relatively large amplitudes ($>10\text{nm}$). A lock-in amplifier is used to extract the precise amplitude and phase of the cantilever oscillation from the vertical deflection. In amplitude modulation, the PI control loop of the Z-Piezo attempts to hold the oscillation amplitude constant at a chosen setpoint while scanning over the surface. A schematic of this concept is shown in Figure 2.14. The

reduction in amplitude when the cantilever approaches the surface can either come from (i) conservative interaction forces, which occur when the eigenfrequency shifts due to the probing of long range interaction forces, or (ii) through dissipation, which occurs when the cantilever partially transfers its oscillation energy to the sample during the contact time of one oscillation cycle [Garcia99, Duerig99a, Paulo01].

The intensity of dissipation has a significant effect on the phase of the oscillating cantilever [Tamayo97]. When recording the behavior of the phase during repulsive amplitude modulation operation, the phase can give quantitative information on how much power is dissipated during tapping [Cleveland98], and thus regions of different material contrast or elasticity can be imaged [McLean97, Magonov97]. However, the phase is often dependent on numerous forces simultaneously, including the size of the free amplitude, setpoints and deviations in surface topography, which results in difficulties interpreting phase images quantitatively [Bar97].

For every measurement in amplitude modulation, the bandwidth of measurement may not exceed the time constant τ , given in Equation 2.18. This generally excludes using amplitude modulation in vacuum environments with traditional commercial cantilevers, as the time constants would exceed 10-100 ms, resulting in scan rates too slow for high resolution imaging. Higher frequency oscillations have recently been used to successfully circumvent this problem [Kawai06a], and open the possibility of using the amplitude modulation method in vacuum environments.

2.7.5 Frequency Modulation

In Figure 2.7 it was shown that the eigenfrequency of an oscillating cantilever will change when it is exposed to external forces. Additionally, the phase difference between an excitation signal and the actual motion of the cantilever at resonance is always 90° (Section 2.6.1). Thus, as the tip experiences forces through its interaction with a surface, the eigenfrequency of the oscillation and thus the phase of the oscillation will change. In frequency modulation AFM (FM-AFM) [Albrecht91], the cantilever is always oscillated at its eigenfrequency, regardless of the forces experienced by the system. This is done by feeding the phase signal into a phase locked loop (PLL) which will hold the phase of the system constant at 90° through feedback modulation of the frequency [Duerig97]. A schematic of this concept is shown in Figure 2.15. The Z-piezo control loop will thus attempt to hold a constant frequency shift $\Delta\omega$, whose value is either a positive or negative frequency shift from the fundamental frequency when no external forces are present. Thus, by choosing the proper setpoint, we can precisely expose the oscillating tip and cantilever to either attractive (negative frequency shift) or repulsive (positive frequency shift) tip-sample interaction forces. As seen in Figure 2.11, the sign of these frequency shifts gives rise to the particular FM operating mode; when the cantilever is only exposed to attractive forces

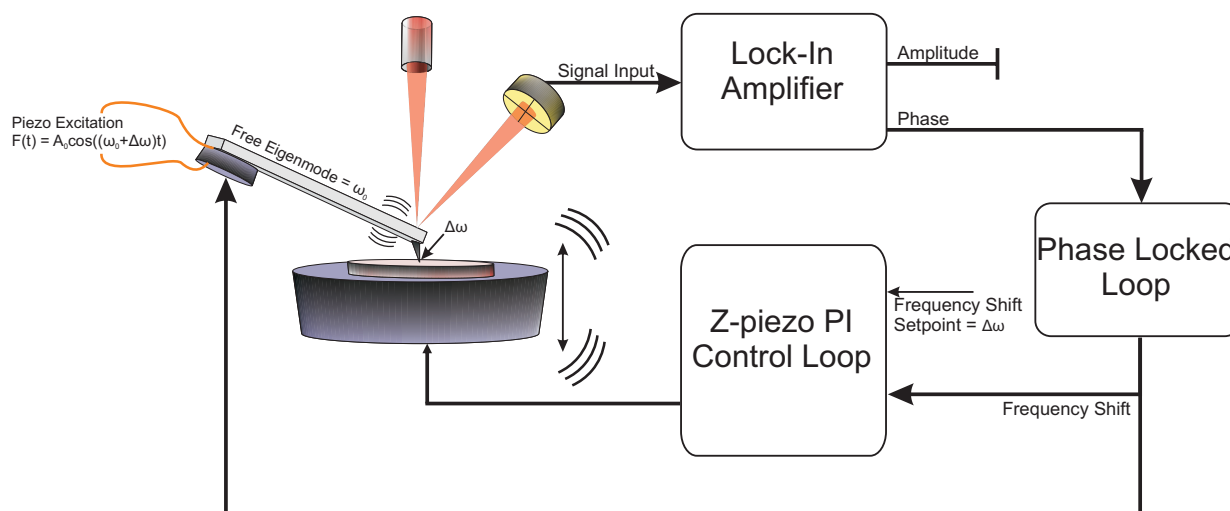


Figure 2.15: Principle of an AFM in the frequency modulation control configuration. The excitation source is a dither piezo. The effective oscillation is recorded by the beam deflection sensor, the resulting phase difference between the piezo excitation is rendered by the lock-in amplifier. The lock-in feeds the phase signal to a phase locked loop, which is an additional control loop that attempts to hold the phase at 90° by shifting the frequency. The Z-dimension PI controller will then attempt to hold the frequency shift equal to the setpoint frequency shift by moving the position of the z-piezo relative to the cantilever.

(negative frequency shifts), the potential for destructive interaction between the tip and sample is minimal. Scanning with a constant negative frequency shift has thus been termed the non-contact region of operation. As the tip moves closer to the sample, the oscillating cantilever will enter the repulsive region within the distance of oscillation, which will quickly tip the frequency shift to a positive value; this region is known as the intermittent contact region of scanning. In non-contact FM-AFM, the Z-piezo control loop will try to hold the tip-sample interaction at a constant negative frequency shift. Like in the case of the Lennard-Jones interaction (see Section 2.5.2), these attractive force regions can be extremely short ranged; if the cantilever were to enter the repulsive region, the slope of the control signal would change sign, causing a catastrophic crash of the tip into the sample due to the onset of positive feedback by the Z-piezo controller. Thus, non-contact FM-AFM is restricted to small scan areas and flat samples where the danger of unintentionally entering the repulsive region is minimized.

FM-AFM has significant advantages over other methods of scanning control. It is a highly sensitive dynamic technique that can be set to scan in non-contact, thus eliminating the destructive interactions that may occur with the tip or the sample in a direct contact mode scan; this enables true atomic resolution imaging on sensitive or chemically reactive surfaces [Giessibl95], and possibly even imaging of individual atomic orbitals [Giessibl01]. Additionally, the response

time of the cantilever is not limited by the Q-factor of the oscillation, making this technique the primary mode of operation in vacuum environments. FM-AFM technique has proven to be a useful technique for achieving high resolution imaging in liquid environments where true molecular and atomic resolutions have been achieved [Fukuma05d, Fukuma05a]

2.7.6 Small Amplitude AFM

Large amplitude dynamic force microscopy does not accurately represent the force gradient of the tip-sample interaction, as it will average the forces experienced by the tip throughout the total spatial distance of the oscillation [Duerig99b]. Small amplitude AFM techniques have proven useful in addressing the difficulties associated with the nonlinearity of the tip-surface interactions. Ideally, small amplitudes serve to linearize the interaction in the region of oscillation [Hoffmann09]. Arbitrarily large amplitudes will spend a significant amount of time in the long-range interaction region, and only a minimal amount of time in the short range interaction region, where atomic scale image contrast is obtained [Eguchi02]. For small amplitudes, the frequency shift of an oscillating cantilever is directly proportional to the tip-sample force gradient experienced by the tip throughout the oscillation amplitude [Giessibl97], increasing the Δf signal to noise ratio and simplifying tip-sample control.

However, as smaller amplitudes will increase the signal originating from short-range interaction forces, reducing the amplitude will always decrease the signal-to-noise ratio (SNR) of the oscillation detected by the frequency detector [Eguchi02]. This can be compensated by increasing averaging, however this would increase the time needed for scans and measurements, which will quickly increase the interference caused by thermal drifts [Abe07]. Decreasing cantilever dimensions will increase resonance frequencies without changing spring constants [Viani99], allowing faster measurements without a decrease in sensitivity in ambient environments. As optical beam deflection is an angle measurement technique [Labuda11], the true minimum detectable signal is an angle, not a displacement. As the length of cantilevers is reduced, the minimum detectable displacements increase when angle deflections remain constant [Walters96]. Use of these small dimensional cantilevers has generally been limited by instrumentation. Optical beam deflection sensors on commercial microscopes have limited bandwidths predominately due to the design of the electronic readouts. Small cantilevers with resonance frequencies beyond a few MHz have been measured in the past through interferometry or by using heterodyne down-sampling methods [Fukuma04, Fukuma05c, Kawai06b], however it has not been possible to measure these oscillations directly using beam deflection. Therefore, it is an ongoing interest in AFM to improve the bandwidth of beam deflection sensors [Frenken10, Khan10]. These improvements will increase the signal-to-noise ratio while simultaneously opening the possibility of using small cantilevers for high resolution scanning and will help decrease the gap that remains

between the experimental and theoretical [Putman92a] lower limits of detectable deflection.

2.7.7 Bandwidth and Noise Limits of the state of the art AFM

Noise Equivalent Deflection Density		
Method	Freq. [kHz]	Noise $\frac{fm}{\sqrt{Hz}}$
Piezoelectric	33	35 [Grober00]
	26	170 [Giessibl00]
Interferometric	290	1 [Hoogenboom05]
	274	2 [Rasool10]
	4.5	6 [Schoenenberger89]
OBD	303–435	26–56 [Hosokawa08]
	123–1660	5.7–9 [Fukuma06]
	110–620	4.7–7.8 [Fukuma09]

Table 2.1: A noise spectrum comparison of deflection detection techniques at different oscillation frequencies. Deflection noise values are generally reported by measuring the voltage noise floor around the eigenmode and then multiplying this with the lever sensitivity.

It is fundamental that the added noise generated by the electro-optical readout and frequency detection system remains minimal. Several scanning probe force detection systems are successfully used today with considerably different force detection sensitivities and noise levels. These include the piezoelectric force sensors [Karrai95, Giessibl00], interferometric sensors [Rugar88], and the optical beam deflection sensors (OBD) [Meyer90]. An analysis of the sensitivities reported to date is shown in Table 1, including the resonance frequencies at which these sensitivities were measured. The recent success of the piezoelectric or “tuning-fork” setups is less due to the low noise characteristics of the deflection detection, but for the signal generating capability of the extremely stiff sensors, reducing their susceptibility to snap-in.

Of all methods proposed to detect cantilever deflection, the optical beam deflection (OBD) method is the most widely used due to the ease of beam alignment and simple experimental setup [Putman92b]. Theoretical studies have suggested that OBD sensitivity should be equal [Rugar88] or even significantly better [Ng07] than interferometric sensitivity. However, experimentally, interferometric detection methods have proven to be more capable of satisfying low noise and bandwidth requirements.

Any well designed detection system will eventually reach the shot noise of the electro-optical system as the lowest possible noise floor. Maintaining this noise floor is crucial for high resolution imaging, particularly for low-Q environments [Kobayashi09]. When designing OBD readouts for use with smaller cantilevers, it becomes increasingly difficult not only to achieve the necessary bandwidth [Fukuma09], but also to maintain the shot noise level as a noise floor.

2.7.8 The Shot Noise Limit

Shot noise originates from the statistical uncertainty of the quantized nature of a measurable signal. Electronic shot noise is due to the finite number of energy carrying electrons that generate a signal by moving from one position to another. Shot noise from an optical beam originates from the zero-point vacuum fluctuations of the electromagnetic field, essentially the lower limit where the signal generation is limited by the uncertainty of the electromagnetic wave [Xiao87]. Shot noise is often cited as the limit for the lowest possible noise level. This is true, to a certain extent- shot noise is one of the most difficult limits to improve upon, so when the dominating noise of a device or system is shot noise, the system is said to have reached the limit of its potential for improvement. Adding signal power (brighter lasers, reducing the loss of light in the optical path, increasing signal currents) is generally the only method of further increasing signal-to-noise when shot noise is the limiting factor. In beam deflection setups that are considered shot noise limited, the system is limited by the shot noise of the optical beam [Putman92b]. Thus, it is important to evaluate and improve the amount of initial photocarriers and the loss of any photocarriers in the optical path, as powerful amplification on the detector side will not be able to improve on the signal-to-shot noise ratio [Hobbs09].

Chapter 3

Translinear Beam Deflection Sensor

In 1975, Barrie Gilbert came up with a new class of circuits whose behavior is dictated by the precise exponential current-voltage characteristic of the bipolar junction transistor. Bipolar junction transistors were previously only considered as linear current amplifiers, using the well known forward current gain characteristic, β . Subsequently Gilbert discovered the translinear principle, a simple algebraic notation which allows one to consider and calculate the signals as currents flowing through the circuits, instead of voltages. Many signal processing operations such as basic arithmetic computations can thus be done entirely on relatively simple BJT based current-mode circuits, entirely in the analog domain before digital conversion.

Circuits where the relevant signals are represented by currents, rather than voltages, have numerous advantages, including the realization of designs with a reduced number of components, a reduction in power consumption, and the avoidance of large voltage swings and thus parasitic capacitances, which will give significant improvements in bandwidth [Koli03]. The use of currents as the relevant signal in OBD has been attempted in the past [Spear96], but was implemented using multiple photodiodes; a similar solution does not exist for the common quadrant photodiode used in the vast majority of AFMs today.

3.1 Adding and Subtracting Currents: The Current Mirror

Kirchhoff's Current Law (KCL) states that at any circuit junction, the sum of currents flowing into that junction is equal to the sum of currents flowing out. The total sum of currents must always add to zero. This rule implies that if 2 currents are to be added together, one simply needs to sink them into the same junction, and they will add. Similarly, if one wants to subtract one current from another, one should source the subtracting current from the relevant junction.

When two signal currents are sourced from a device, as from the anode of a photodiode, one

is required to convert one signal current from source to sink in order to achieve a subtraction. This can easily be done using a current mirror based subtractor [Rosenthal77], a device which is shown in Figure 3.1. A simple current mirror consists of two NPN bipolar junction transistors (using PNP transistors will convert the reverse case). Both transistor emitters are connected to ground and the bases are connected together. One transistor has its collector connected to the base; this is generally termed "diode connected" since it converts the transistor to a simple diode. When the two transistors have the same device properties (they are matched) then the current sunk into the collector of the diode connected transistor is equivalently sourced by the collector of the second transistor. Thus, when inspecting node N in Figure 3.1 using KCL, it can be seen that the current i_A is subtracted from the current i_B , with the remaining difference either sourced or sunk through the transimpedance stage with resistor R , converting the signal current to a voltage.

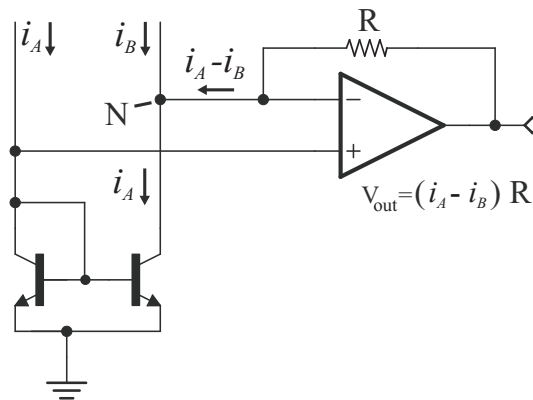


Figure 3.1: Schematic of a current subtractor as detailed in [Rosenthal77]. A simple current mirror is combined with an ideal transimpedance amplifier. The transimpedance stage only converts and amplifies the current difference, as can be seen when inspecting node N using Kirchhoff's rules.

3.2 Translinear Principle

Translinear circuits are circuits generally comprised of BJT transistors operating in the forward active domain where the collector current is exponentially dependent on the base-emitter voltage [Gilbert96]. Since voltage swings are thus logarithmically related to currents, a large dynamic range when used in low voltage environments is permitted. Conceptually they can be considered as circuits where the relevant signals are comprised of currents, instead of voltages. They are often used for analog signal processing operations, such as multiplication, division, integration, log-domain calculations and hyperbolic functions [Huijsing99]. Translinear circuits follow the behavior dictated by the translinear principle, given as [Gilbert75]:

$$\prod_{CW} I_{c,i} = \prod_{CCW} I_{c,i} \quad (3.1)$$

where I_c is the collector current of the transistor i . The translinear principle states that the product of the currents of two hypothetical loops in a closed-loop circuit of even transistor elements will equal each other, where one loop is comprised of clockwise (CW) pointing elements and one comprised of counter-clockwise (CCW) pointing elements. This stems from the fact that voltages through the loop must sum to zero, i.e. an equal number of positive (clockwise) and negative (counter-clockwise) elements. Through the logarithmic current to voltage relationship this sum translates to a product of currents.

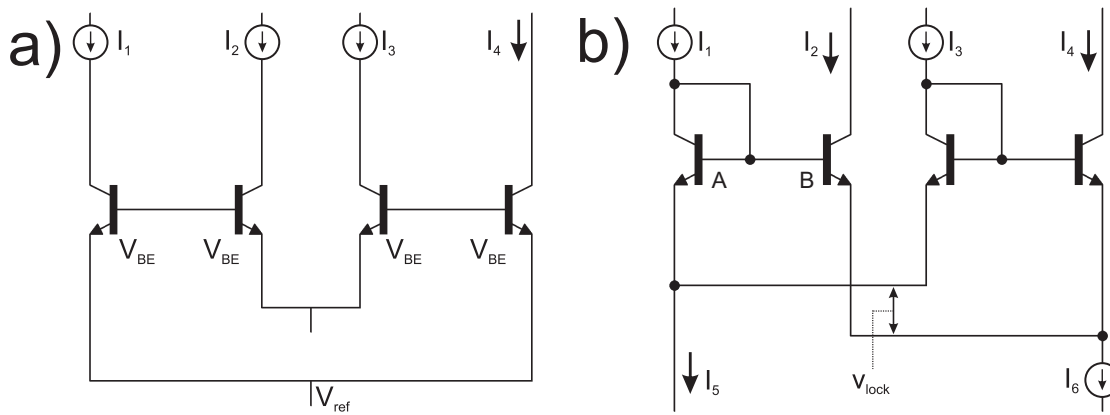


Figure 3.2: A basic translinear a) multiplier and b) divider.

A simple current multiplier is shown in Figure 3.2a. The voltage loop from V_{ref} through the transistors and back to V_{ref} must equal zero [Fan Fei09]:

$$V_{BE1} - V_{BE2} + V_{BE3} - V_{BE4} = 0 \quad (3.2)$$

and

$$V_{BE} = V_t \ln\left(\frac{I_c}{I_s}\right) \quad (3.3)$$

where V_t is the thermal voltage, I_c is the collector current, and I_s is the reverse saturation current. Thus the voltage loop in Figure 3.2a consists of

$$V_t \ln\left(\frac{I_1}{I_s}\right) - V_t \ln\left(\frac{I_2}{I_s}\right) + V_t \ln\left(\frac{I_3}{I_s}\right) - V_t \ln\left(\frac{I_4}{I_s}\right) = 0 \quad (3.4)$$

resulting in

$$\ln\left(\frac{I_1 \cdot I_3}{I_2 \cdot I_4}\right) = 0 \quad (3.5)$$

or simply

$$I_1 \cdot I_3 = I_2 \cdot I_4 \quad (3.6)$$

Thus, the simple circuit given in Figure 3.2a is a basic current multiplier, with current inputs I_1 , I_2 , I_3 and current output I_4 . Similarly, a circuit performing analog division (normalization) can also be implemented using translinear elements, and is given in 3.2b. This circuit is known as a translinear normalizer, as proposed by Gilbert [Gilbert84]. Here, I_1 , I_3 , and I_6 are signal inputs, and I_2 , I_4 , and I_5 are outputs. The difference in base-emitter voltages of transistors A and B has to equal V_{lock} , which must be true for every additional transistor pair added into the system. Thus:

$$V_{lock} = V_t \ln\left(\frac{I_1}{I_s}\right) - V_t \ln\left(\frac{I_4}{I_s}\right) = V_t \ln\left(\frac{I_1}{I_4}\right) \quad (3.7)$$

and

$$\frac{I_1}{I_2} = \frac{I_3}{I_4} \quad (3.8)$$

The ratios of the currents flowing through each transistor pair is equal when the locking effect of V_{lock} is not disturbed. With ratios equal, the following can be deduced:

$$\frac{I_2}{I_1} = \frac{I_2 + I_4}{I_1 + I_3} = \frac{I_6}{I_1 + I_3} \quad (3.9)$$

resulting in

$$I_2 = I_6 \frac{I_1}{I_1 + I_3} \quad (3.10)$$

The current resulting at I_2 is thus a copy of I_1 , normalized by the common mode signal of the inputs on all channels, and scaled by the magnitude of the normalizing current I_6 .

3.3 Translinear Optical Beam Deflection Sensor

Translinear circuits can also be used to execute the analog signal processing steps necessary to compute the analog arithmetic of a quadrant photodiode [Enning11]. The relevant signal extracted from a photodiode is an intensity-dependent current, as mentioned in Section 2.6.3. The equivalent model of a typical photodiode is shown in Figure 2.9a. The bi-cell photodiode device has two anodes, each with the signal current relative to the intensity of light corresponding to its quadrant.

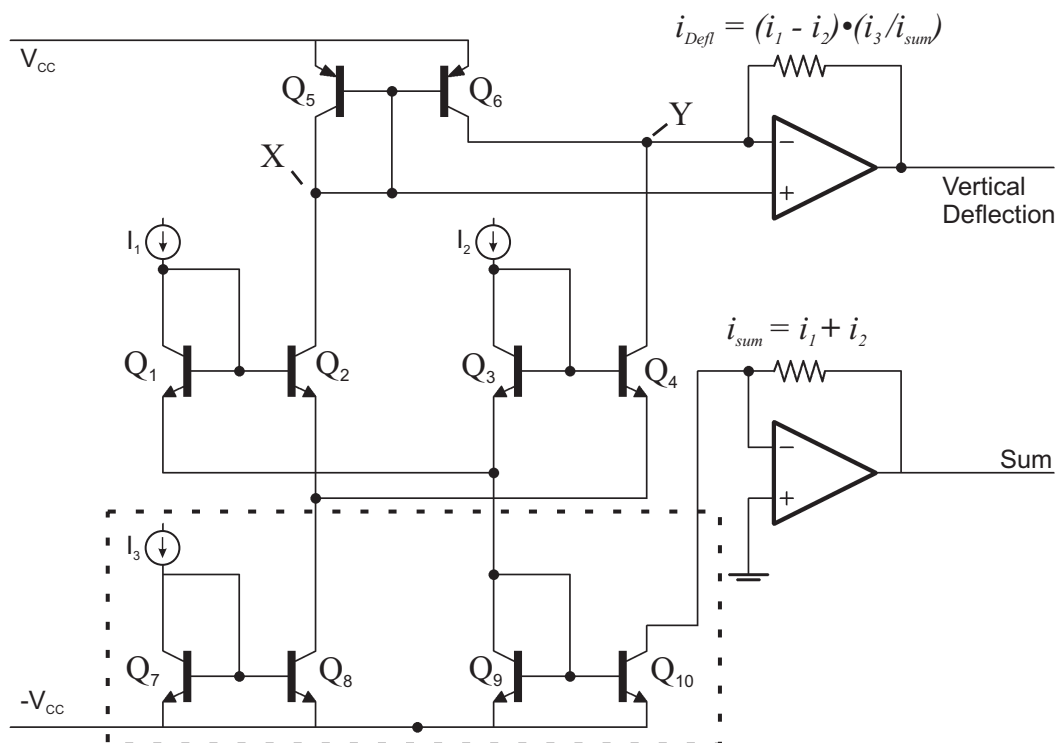


Figure 3.3: A basic translinear beam deflection readout for a bi-cell photodiode.

In the design of figure 3.3, each initial diode current (I_1 and I_2) is copied using bipolar NPN

transistors ($Q1$ to $Q4$), similar to the current mirror in Figure 3.1. The copied I_1 current is subsequently sourced from node X, extracting it from the diode connected transistor of the PNP current mirror. The PNP current mirror will attempt to sink the same amount of current into node Y. Simultaneously, the copied I_2 current is sourced from node Y; any imbalance in the copied I_1 and I_2 currents is either sunk or sourced through the resistor of the transimpedance amplifier, converting the current signal into a voltage. The subsequent output is the effective vertical deflection, as given in Formula 2.22.

3.3.1 Extracting the Sum

In the circuit of figure 3.3, the currents originating from each anode of the photodiode are gathered and inserted into the current mirror made up of transistors $Q9$ and $Q10$. The collector of $Q10$ feeds the second transimpedance amplifier, resulting in a sum signal. An alternative method to quantify the sum would be to mirror the current running through the cathode of the quadrant photodiode.

3.3.2 Signal Normalization and Amplification

In many AFMs laser intensity fluctuations can be a significant and unnecessary source of noise. Intensity fluctuations are common to all quadrants the laser falls upon, and thus common to each photocurrent. In many optical readouts the vertical and horizontal deflection signals are subsequently divided by the sum signal (or common mode rejected using instrumentation amplifiers), removing the intensity fluctuations and other common noise entirely. The relatively slow analog dividers or instrumentation amplifiers [Fukuma05d] used will again significantly reduce bandwidth. In our setup, we use a translinear normalizer [Gilbert84] (which is created when transistors $Q7$ and $Q8$ are added as shown in the dotted box of Figure 3.3). It is noteworthy that this normalization method is very fast, limited only by the bandwidth of the transistors. This overcomes the significant bandwidth bottleneck mentioned previously. In addition to removing common mode signals from all four photodiode currents, the translinear normalizer causes a non-unity current ratio in the mirrored currents by the externally applied input current I_3 , which can be an order of magnitude larger than the photocurrents, depending on the transistors used. This introduces a large transistor level gain, in which small differential currents are significantly amplified before the signal is further buffered by the transimpedance stage. Active control of this current will allow the user to set the desired beam deflection sensitivity, without the need of exchanging any hardware. Thus, a complete single channel beam deflection sensor requires only 10 bipolar transistors and 2 transimpedance stages.

3.3.3 Dual Channel Translinear Readout

Quadrant photodiodes offer the possibility of detecting deflections in 2 dimensions, namely vertical and horizontal deflections. In this case, each signal current needs to be copied twice; one for each channel. In the dual channel design (Figure 3.4), the current from each anode is copied twice using multiple output current mirrors [Loh97], once each for the horizontal and vertical calculations. However, as more transistors are added to the current mirrors, the base input currents will increasingly drain and distort the photodiode current. Furthermore, the base-emitter capacitance of each new transistor indirectly adds to the junction capacitance of the photodiode, which will reduce bandwidth. In order to bypass these problems, beta helper transistors Q1-Q4 are added, effectively reducing the base-emitter capacitive loads on the photocurrents. Ground connected resistors R1 and R2 serve to set the transistor level gain i_3 of the translinear normalizers on the horizontal and vertical channels, respectively.

3.3.4 Implementation

The circuit designs shown in Figures 3.3 and 3.4 were layout on a 28.5 x 34 mm² printed circuit board, which was fabricated by a precision mill (Step Four Basic 540, Wals-Siezenheim, Austria). The circuit board was deliberately held small in order to reduce the possibility of current leaks and parasitic capacitances increasing noise and reducing bandwidth. A dual channel (Figure 3.4) board with completed layout can be seen in Figure 3.5a. The single and dual channel circuits were implemented with discrete components, and consisted of the following parts: the quadrant photodiode used was a SD 085-23-21-021 by Advanced Photonix; HFA3127 and HFA3128 by Intersil for the NPN and PNP transistors; the resistors governing i_3 (R1 and R2 in figure 3.4) were adjustable potentiometers between 10 - 500 Ω , and the transimpedance feedback resistors were 5.6 k Ω . The feedback capacitors (transimpedance feedback capacitors, not shown in the schematic of Figure 3.4) were set at 2 pF. The operational amplifiers used were THS4011. +V was adjustable from 1.2V to 4V and -V was -3.5V; the transimpedance stages were powered with $\pm 12V$. Additionally, the small size allowed the circuit board to be attached directly to the side of the Multimode AFM head (Bruker AXS Inc., Madison, WI, USA), as can be seen in Figure 3.5b. Both imaging and noise analysis were performed on the modified Multimode AFM in combination with an E-scanner and a Nanonis (SPECS, Berlin, Germany) controller. The microscope was enclosed in a home-built acoustic and electric shield on a vibration isolation table. The optical lever sensitivity of every cantilever was calibrated by a surface approach measurement in which the amplitude of the first eigenmode is recorded against tip sample distance. By increasing the translinear normalizer reference current i_3 (Figure 3.3), we can significantly increase the signal gain, and through this the optical lever sensitivity.

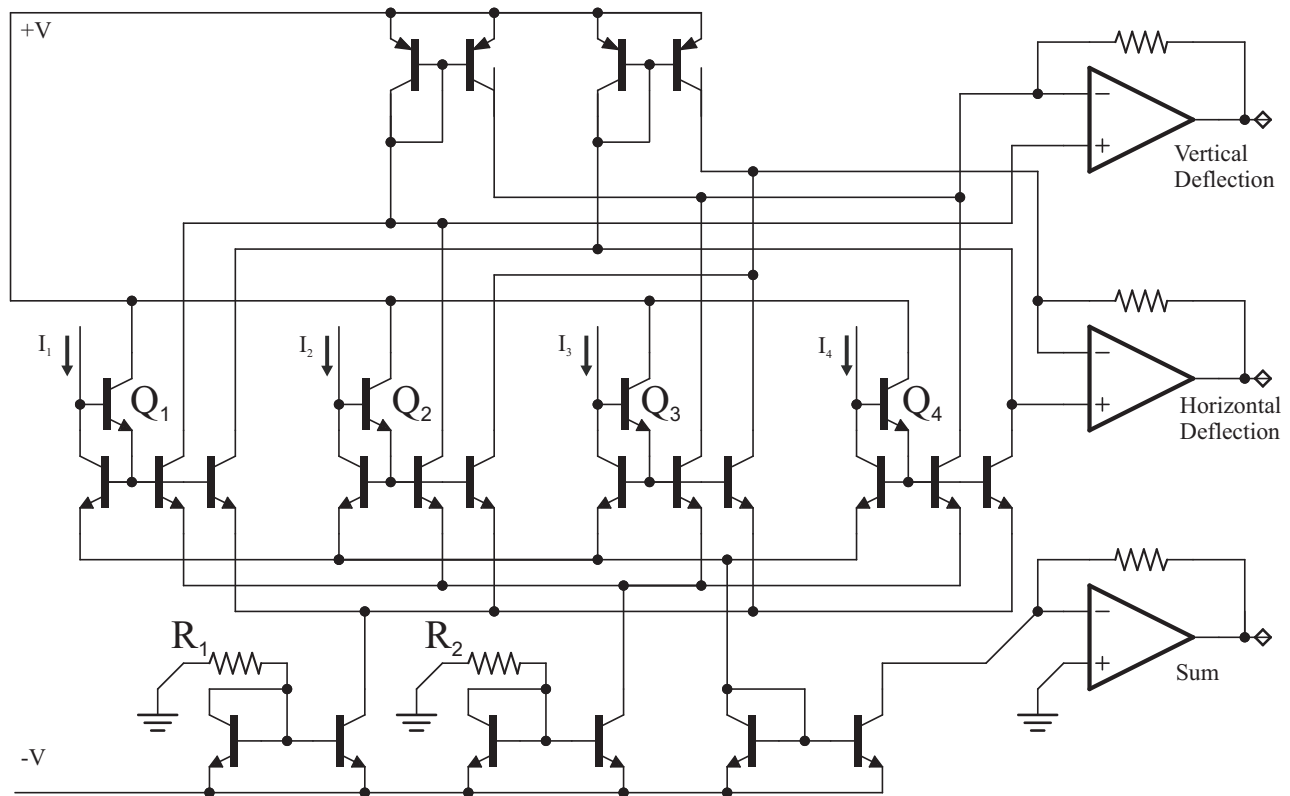


Figure 3.4: A dual channel translinear beam deflection readout for calculating vertical and horizontal deflections on a quadrant photodiode.

3.3.5 Bandwidth Measurements using Emulated Photodiodes

In order to measure the electronic bandwidth of the system, the photodiodes were emulated by using a high bandwidth current source with a linear frequency response in the region of interest. In addition, adding capacitances in parallel to the "ideal" current source, brought the setup closer to the true operation of a photodiode. This excitation circuit can be seen in figure 3.6a. Capacitors of 10pF were used, as these were close to the manufacturer stated junction capacitance (9pF) of the quadrant photodiode when properly reverse biased. A vertical deflection was simulated by applying an oscillating current signal to the quadrants A and B, and applying the same 180° phase shifted signal to quadrants C and D. The bandwidth of the current source, consisting primarily of an AD8132 differential output amplifier, was well over 50MHz (tested separately). The AD8132 allows the application of a DC offset with an added AC signal, which was

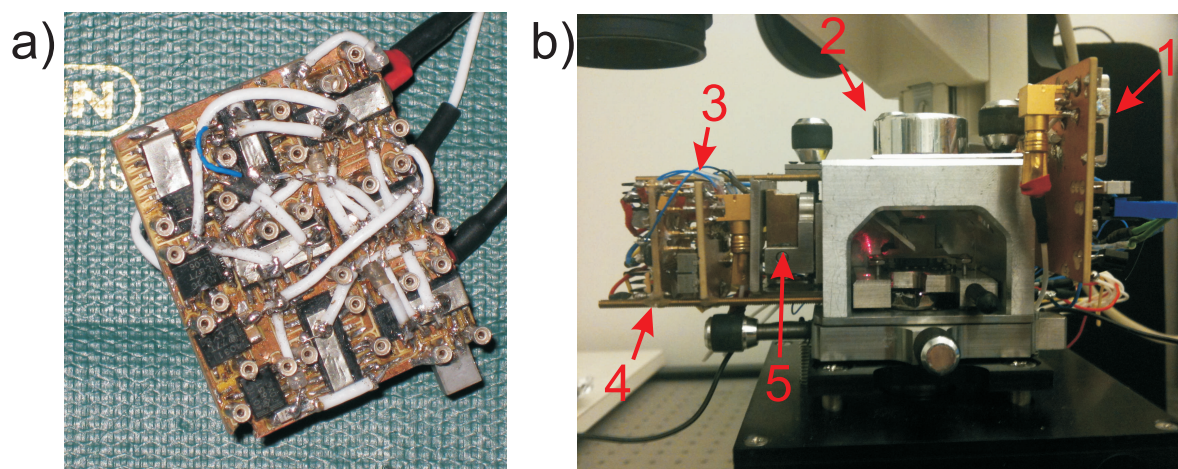


Figure 3.5: a) Board layout and setup of a dual channel beam deflection readout. Due to the sensitivity of current leaks in board layouts, most important lines consisted of very thin shielded coaxial wire. b) The modified Multimode AFM head with a translinear readout. 1) Laser diode driver board, with high frequency modulation circuits, 2) The original Digital Instruments Multimode AFM optical head, 3) The circuit board hosting the translinear readout circuit, equivalent to the board seen in a), 4) the power supply stabilization board, 5) the brass micropositioner containing the quadrant photodiode (see Figure 7.5).

necessary for simulating the true operating nature of a quadrant photodiode. The bandwidth of the combined excitation circuit and readout was analyzed using a network analyzer (Hewlett Packard 8753E with 41802A 1M Ω terminated input adapter).

Figure 3.6b shows that as we increase the current, which corresponds to an increase in photocurrent due to increasing laser intensity, the bandwidth of the system will increase as well, up to 20MHz. This is due to the photodiode junction capacitances charging more rapidly due to the increasing photocurrent. When total currents (sum of all quadrants) are below 1 mA ¹ the bandwidth is limited by the junction capacitance of the quadrant photodiodes, as the bipolar transistors chosen have significantly larger bandwidths. At higher intensities, the transimpedance stage assumes the role of limiting factor. Care must be taken to minimize the resistance of a line connecting any two transistors, as this will quickly increase voltage swing along the lines, degrading bandwidth performance. Our SPICE simulations suggest that the bandwidth can be increased to over 70 MHz through the use of smaller quadrant photodiodes and faster transimpedance stage amplifiers without a significant reduction in signal-to-noise. Additionally, it has been shown both theoretically and experimentally [Torbrugge08, Fukuma05b] that the shot noise floor decreases as laser intensity is further increased. With regard to electronics, it would

¹using a 650 nm laser, 1 mA is approximately equal to a laser intensity of 2.5 mW. This is dependent on the photodiode responsivity and the laser wavelength chosen.

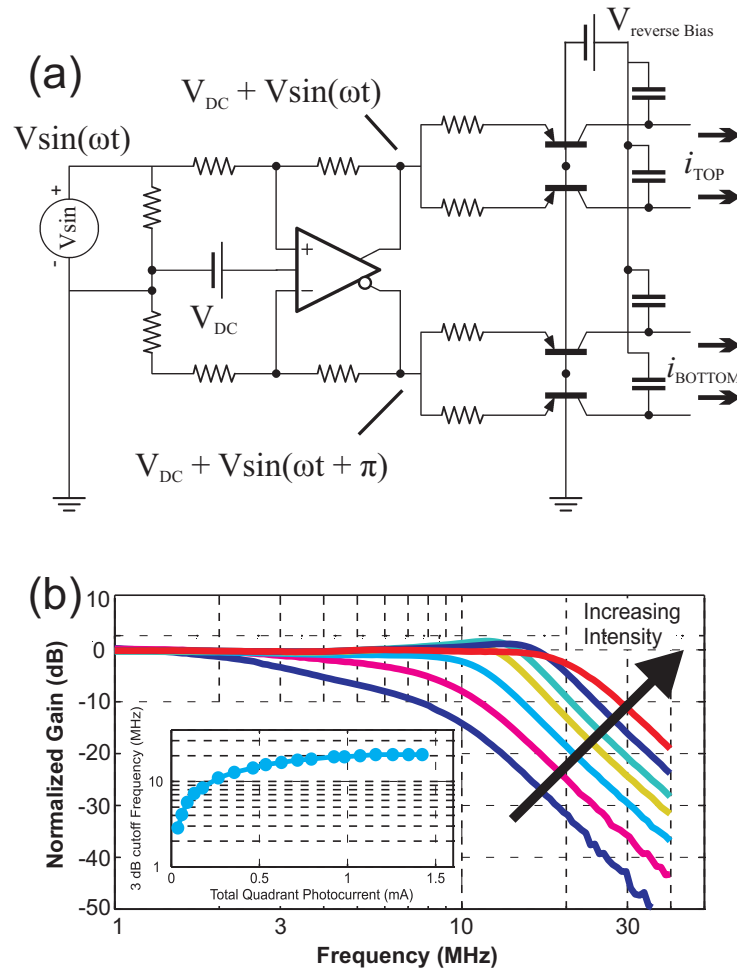


Figure 3.6: (a) The quadrant photodiode emulation circuit. Current signals between i_{TOP} and i_{BOTTOM} are phase shifted by π . (b) The frequency response of the translinear circuit using the emulated quadrant photodiode as a function of irradiation. As the total photocurrent is raised, the bandwidth (3 dB) of the circuit is increased, up to a maximum of 21MHz.

be desirable to have the brightest possible light source, as long as the optical noise in the light source remains shot noise limited.

3.4 Application

3.4.1 Bandwidth Measurements of Selected High Frequency Cantilevers

In order to accurately measure the response of the deflection sensor with small dimension high frequency cantilevers, an optical tabletop OBD setup was designed with photothermal excitation capability (See Chapter 8). The diameter of the laser spot on the backside of the cantilever was measured to be less than $4\mu\text{m}$. The frequency response of three prototype USNMCB cantilever

(Nanosensors, Neuchâtel, Switzerland) can be seen in Figure 3.7a. A SEM image detailing the lateral dimensions of these cantilever is seen in the inset. The fundamental eigenfrequencies of these cantilevers were measured at 1.61 MHz (red), 3.57 MHz (blue), and 5.10 MHz (yellow). In addition to the fundamental, the second eigenmode of the 1.61 MHz and 3.57 MHz cantilevers can be seen at 10.6 MHz and 21.4 MHz, respectively. The amplitude and phase v.s. frequency curves of the first and second eigenmodes of the 3.57 MHz prototype cantilever are seen in figure 3.7b and figure 3.7c. The capability to detect these high frequency oscillations confirmed that the bandwidth capability of the complete beam deflection detector was very close to the one measured with the emulated photodiodes in Section 3.3.5.

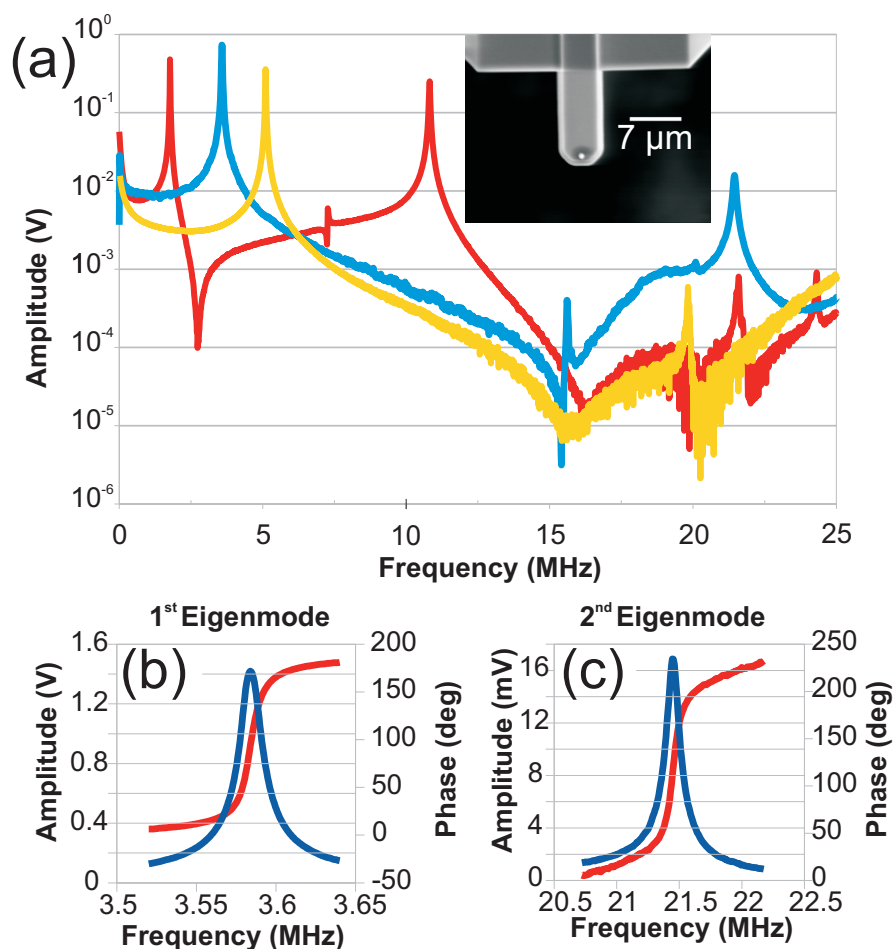


Figure 3.7: (a) Frequency response (0-25 MHz) of a high frequency cantilevers (Nanosensors USNMCB-3.5MHz prototype); inset is a SEM image of the cantilever. The first 2 eigenmodes of the 3.5 MHz cantilever are shown at (b) 3.57 MHz and (c) 21.4 MHz, using optical excitation.

3.4.2 DC Stability

The system provides very high stability and sensitivity at DC as well. In order to measure these effects at DC, an Arrow UHF cantilever was mounted in the microscope which was enclosed in the acoustic and electric shield and was allowed to stabilize thermally for 5 hours before measurement. The DC sensitivity of the beam deflection was measured to be $1.046 \frac{V}{nm}$. In a time interval of 5 seconds (sampling rate 20 ms) the RMS noise in the vertical deflection was recorded as 3.145 mV (15.493 mV peak to peak). In a time interval of 5 minutes (sampling rate 484 ms), the RMS noise jumped to 9.293 mV (53.790 mV peak to peak). Finally over an interval of 5 hours (sampling rate 5 s), the RMS noise was recorded as 20.947 mV (106.913 mV peak to peak).

3.5 Noise Evaluation

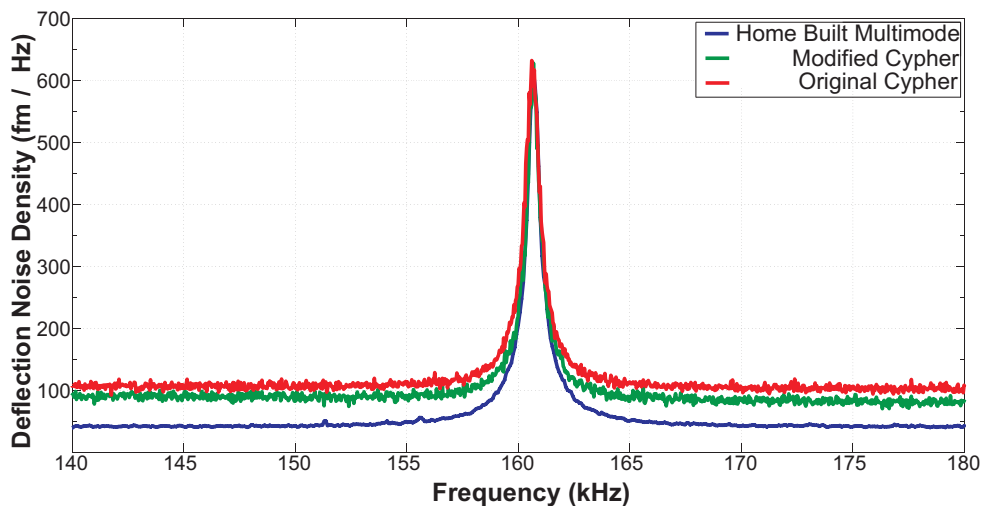


Figure 3.8: A thermal peak based noise comparison of the translinear beam deflection readout installed on different microscopes. The cantilever used was an Olympus AC200, centered at 161.4kHz. Red curve: thermal peak on the original Asylum Research Cypher beam deflection readout; noise floor at $122 \frac{fm}{\sqrt{Hz}}$. Green Curve: Thermal peak of the same cypher microscope with a translinear beam deflection readout attached to the photodiodes; noise floor at $86 \frac{fm}{\sqrt{Hz}}$. Blue curve: Thermal peak of the same cantilever using the Multimode AFM head with a translinear readout; noise floor at $43 \frac{fm}{\sqrt{Hz}}$. The roughness of the red and green curves is due to insufficient averaging by the Cypher's software.

In addition to the bandwidth, the noise floor of the system was measured. This is usually done by measuring the height of the noise floor around the spectrum of a calibrated thermal Brow-

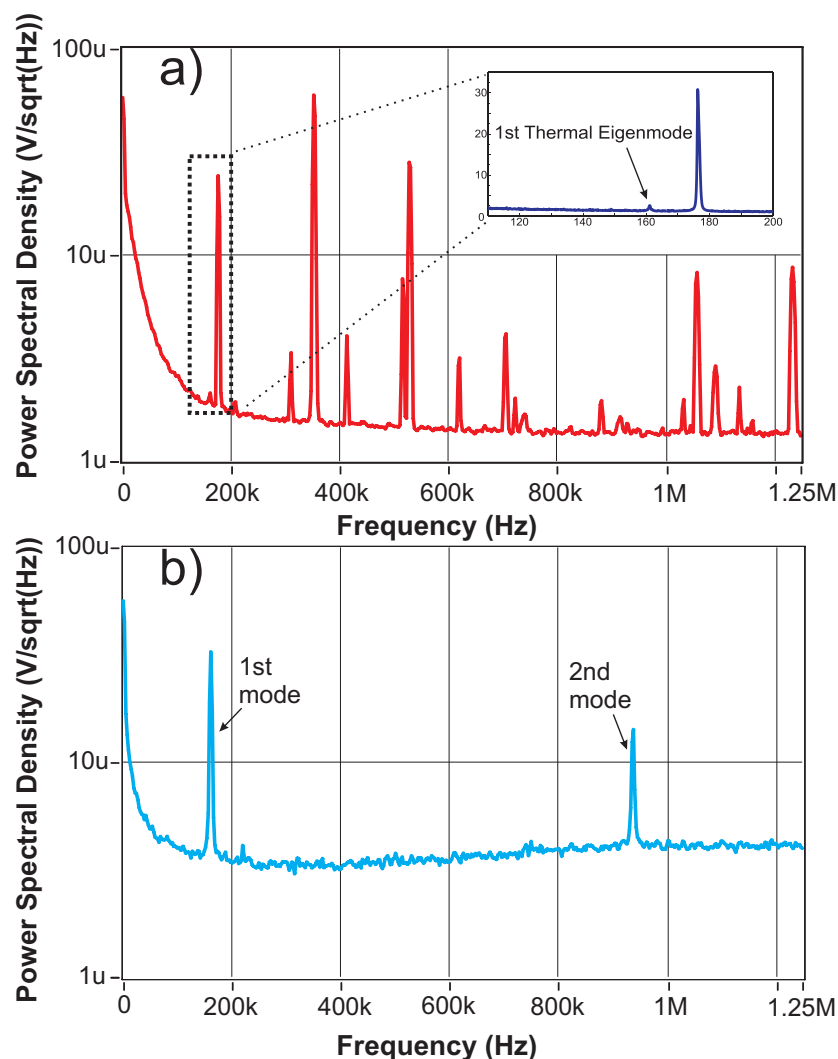


Figure 3.9: Spectral comparison of the original Multimode AFM readout (a) with the translinear readout (b). Most of the peaks in (a) are generated by spurious signals from the insufficiently shielded electronics, the first eigenmode can barely be seen; it is pointed out in the inset. The second eigenmode is close to the bandwidth limit of the readout, and is not detected. The peaks generated in (b) are the true thermal peaks of the first two eigenmodes of the oscillating cantilever. Cantilever used was an Olympus AC200.

nian peak (see Section 5.1 for more information).² Thermal Brownian motion of the cantilever sets the limit for the smallest drivable eigenmode amplitudes and smallest detectable forces [Butt95, Walters96, Mamin01]. Small, stiff cantilevers have significantly less Brownian motion than large or soft cantilevers. Thus, it is desirable to have the lowest possible noise values in order to detect the smallest oscillations of even stiff and small cantilevers, and to reduce phase noise in frequency modulation systems. In order to evaluate the noise performance of the translinear readout, the device was installed on two different microscopes; a home built

²The thermal peaks described in this section were acquired using a NI-5911 PCI signal capture card.

Multimode AFM microscope, as mentioned previously in Figure 3.5, and on a Cypher (Asylum Research, Santa Barbara, CA, USA) microscope. The original beam deflection readouts of these microscopes are voltage-mode and have a similar schematic as in Figure 2.10. In order to evaluate the performance of the translinear readout on all three machines, the same Olympus AC200 cantilever was used to measure all noise values. The results of these evaluations can be seen in Figure 3.8.

From this Figure it can be seen that the translinear readout slightly improves the noise floor of the Cypher system from 122 to $86 \frac{fm}{\sqrt{Hz}}$. The performance of the same cantilever on the Multimode AFM based readout is significantly improved to $43 \frac{fm}{\sqrt{Hz}}$. Similar improvements can be seen when comparing the readout of the original Multimode AFM with the translinear readout as detailed in Figure 3.9; in a) the thermal peak of the first eigenmode is barely visible through the peaks generated by the inefficiencies of the electronics, while the second eigenmode is already outside of the measurement bandwidth. In b), the spectrum is clean, showing only true eigenmodes and thus the true motion of the cantilever.

3.5.1 Input Bias Current Gain

The input bias current (i_3 in Figure 3.3) is a fundamental parameter of the translinear sensor. If input bias is too low, the gain of the primary current mirrors will be too small and noise from adjacent components will be relevant, reducing the Signal-to-Noise Ratio (SNR). When increasing the input bias current to 7–8 mA, beam deflection sensitivities will increase linearly up to 0.3 to $0.4 \frac{V}{nm}$, depending on the cantilever used. Further increasing the input bias current i_3 will not improve SNR (and thus the deflection noise density), as the system will begin to amplify photodiode noise with the same gain as the signal; this effect can be seen when observing the deflection noise density as a function of input bias current in Figure 3.10a. Arrow-UHF cantilevers (Nanoworld, Neuchatel, Switzerland) produce inverse lever sensitivities at $1 \frac{nm}{V}$. In combination with a noise floor of approximately $4.5 \frac{\mu V}{\sqrt{Hz}}$, this results in a total noise deflection density of $4.5 \frac{fm}{\sqrt{Hz}}$ which can be seen in Figure 3.10b.

3.5.2 Emitter Resistor Gain

An alternate method to achieve increases in gain is to add resistances to the emitters of the diode connected bipolar transistors in the primary current mirrors, as seen in the dotted box of Figure 3.11a. This causes an increase in small signal voltage swing on the shared base of the current mirrors, increasing the gain in the primary amplification stage. However, the increase in voltage swing reacts negatively with the base-emitter junction capacitance of the bipolar transistors, causing reductions in bandwidth. Figure 3.11b shows that as the resistance of both

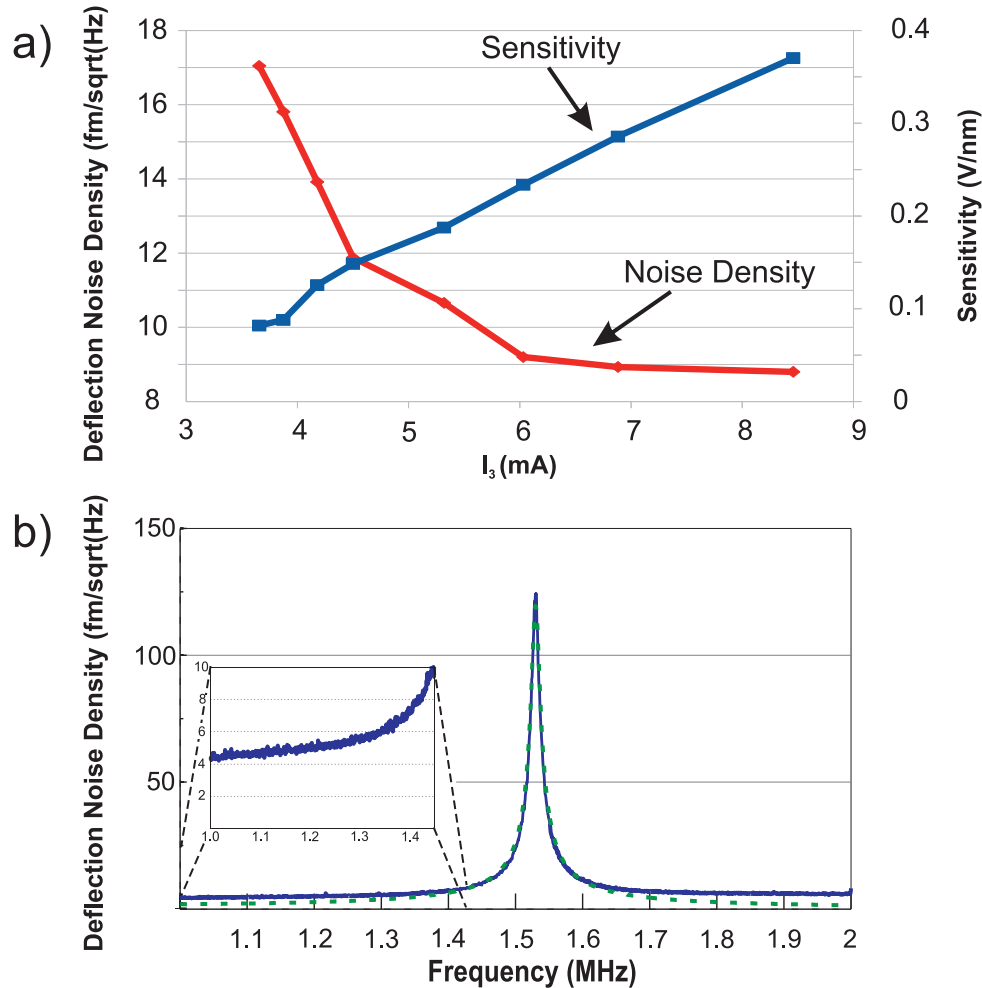


Figure 3.10: a) Sensitivity and deflection noise density of an Arrow UHF high frequency cantilever as a function of input reference current I_3 . Increasing the input reference to a few mA drastically improves the noise floor, reaching a maximum around 7–8 mA. The noise improvements will bottom out, while the sensitivity continues to increase linearly. The actual values for noise floor and sensitivity are dependent on the cantilever used, and can vary from cantilever to cantilever. b) The thermal peak of an Arrow UHF cantilever centered at 1.53 MHz with a spectral noise floor of $4.5 \frac{fm}{\sqrt{Hz}}$. The inset is a zoom on the noise floor. The dotted line corresponds to the theoretically calculated value ($Q=115$, $k=30$ N/m).

potentiometers in the dotted box is increased, the equivalent input current noise of the complete translinear readout circuit will drop significantly initially, only to level out at higher resistances, primarily due to the increasing Johnson-Nyquist noise caused by the resistors themselves³. Additionally it is shown that as the resistance is increased, the 3dB bandwidth of the system

³It is often difficult to measure the input noise of any circuit or amplifier. The simplest way this is achieved is by using the amplifier itself to estimate the noise. When the exact gain of an amplifier is known, the equivalent input noise can be calculated by dividing the noise measured on the output by the gain. Since there are multiple stages that can create gain in the translinear readout (transimpedance stage, emitter resistor gain, bias current gain), the equivalent input current noise of Figure 3.11b is an measured value that includes all gain stages.

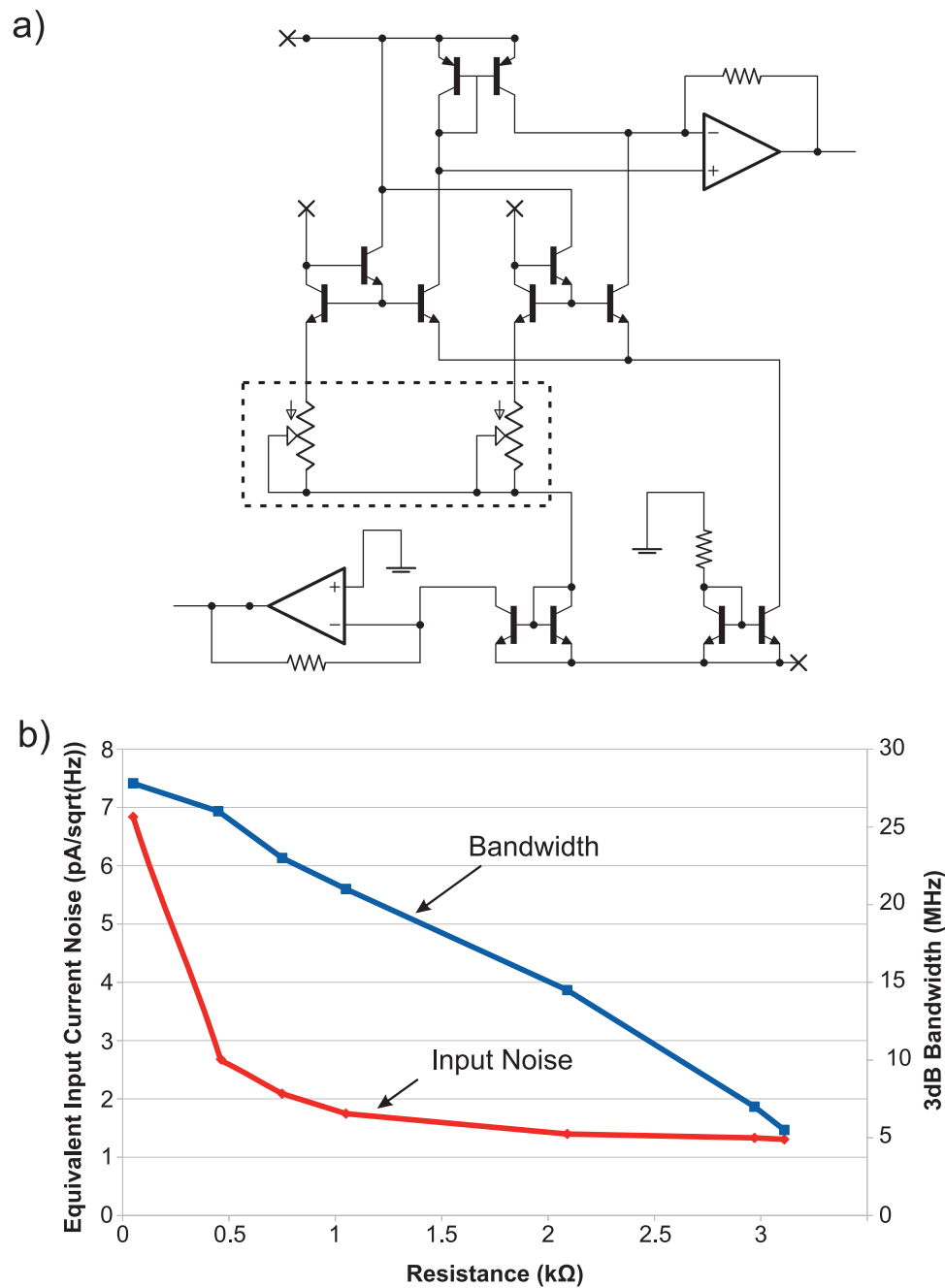


Figure 3.11: a) A simple one channel translinear beam deflection readout, in principle equivalent to the readout presented in Figure 3.3. Two potentiometers are added in the signal path of the original photocurrent (dotted box); this increases signal gain in the primary current mirrors, as the base-emitter small signal voltage swing on the diode connected bipolar transistors is amplified. b) Increasing this resistance will increase gain and thus input noise of the circuit, however this method also increases voltage swing on all nodes in the signal path, causing reductions in bandwidth from junction capacitances. The input noise and bandwidth measurements were taken by creating a known input (and thus gain) using the emulated photodiode of Figure 3.6a.

is continuously reduced. The potentiometers detailed in this section are also a useful tool in zeroing any transistor or any other device mismatch.

3.5.3 Calculating Noise Factor

Every amplifier will add it's own noise to an input signal; translinear circuits offer no exception. This reduction in SNR caused by the internal shot and thermal noises of an amplifier is termed noise factor (or noise figure) and quantifies the drop in SNR when the signal passes through the stage under normal operating conditions. When multiple stages are cascaded in series, the noise factor of each individual stage will propagate noise according to Friis's formula for electronic noise [Friis44]:

$$nf_{tot} = nf_1 + \frac{nf_2 - 1}{G_1} + \dots + \frac{nf_N - 1}{G_1 \cdot G_2 \cdot \dots \cdot G_N} \quad (3.11)$$

where nf_N is the noise factor of the respective cascaded stage and G_N is the gain of that stage. Thus, a strong gain in an early stage will significantly reduce the noise contributions of all subsequent stages.

The initial amplification of the photodiode signals takes place in the primary current mirrors (Q1 - Q4 in Figure 3.3). Noise analysis of BJT current mirrors has been done in the past [Bilotti75]; the most predominant sources are shot noise due to current flow of carriers in the base and collector and the thermal noise of the base resistance, termed limiting noise, and the frequency dependent flicker noise inherent to most electronic devices, termed excess noise. The unity gain spectral output current noise of a typical BJT current mirror is given as:

$$N_o^2 = 2 \frac{I_{cs}^2(1 + 2b + b^2/\beta) + I_{bx}^2(1 + (mb)^2)}{(1 + b/\beta)^2} \quad (3.12)$$

where I_{cs} is the spectral collector current noise, I_{bx} is the spectral base current noise, m is a constant detailing the intensity of the excess noise, β is the small signal current gain, and b is the normalized intrinsic base resistance. Thus, the noise factor of the device is then given as:

$$f = \sqrt{1 + \frac{N_o^2}{N_i^2}} \quad (3.13)$$

where N_i is the equivalent input noise. When a device has a defined input impedance, the input is normally connected to a sensor with an equal output impedance in order to maximize signal power transfer. Thus, the noise can never be lower than the thermal noise of a resistor with the same impedance, given as $\sqrt{2k_BTR}$. With knowledge of transistor characteristics and input impedances, the noise factor of a current mirror can be calculated.

The current mirror of the divider transistors (Q7 and Q8, Figure 3.3) are cascaded with the primary current mirrors of each channel. Thus, the noise generated by the divider will add directly to the total noise of the system as given by Friis's formula. Setting the primary current mirrors to unity gain is the worst case scenario, as noise propagation is at maximum. By increasing the primary transistor's gain by adjusting the reference current i_3 , the noise caused by the divider and all subsequent stages is significantly reduced and the SNR is increased.

3.6 Conclusion

In this chapter we explained the concept and functionality of a translinear optical beam deflection sensor. The translinear principle, on which many current-mode circuits are based on, offers the ability to execute a considerable amount of arithmetic signal processing with the use of a few entirely analog components. We demonstrate that the signal currents can be directly subtracted from one another using Kirchhoff's current law, and only the differential currents are amplified and extracted, which will yield the same vertical deflection signal. The devices themselves consist of primarily a few simple bipolar transistors. We presented a single channel and a dual channel translinear readout, from which a complete beam deflection readout for a bi-cell or quadrant photodiode supplying the vertical deflection, horizontal deflection and sum can be recreated. Translinear circuits offer the power to divide the common, laser generated noise out of the signal channels, without any significant reduction in bandwidth. We detailed the bandwidth gains such a readout has, showing that directly measuring high frequency cantilever oscillations in regions not measured previously is possible. We directly compared the performance of the translinear readout with readouts from commercial devices, and showed that there are significant improvements to conventional readouts. We presented a method to calculate the noise generated by each transistor, and how it adds in to the noise of the complete readout as a whole. Finally we showed that the noise performance of the device is competitive with the most advanced cantilever deflection readouts in use today.

Chapter 4

Optoelectronics

4.1 Laser Diodes

The quality and stability of the light source is as important as the sensitivity of the readout in optical beam deflection. Without a proper stable, low noise optical beam, any improvements in readout design are entirely lost to inefficient or noisy light sources. Laser diodes are one of the most common light sources for AFM. Their small size, high efficiency and high optical beam quality make them a perfect source of light to incorporate into an AFM optical head. They are manufactured in a hermetically sealed metal-can like package, with a small window in the top from which coherent radiation is emitted. The laser itself is a small chip of a semiconductor like Gallium Arsenide, whose band-gap and physical structure determines the wavelength of the emitted light. Most laser diodes are of the Fabry-Perot type, where the die is cleaved, and the cleavage plains form the cavity mirrors. The rear cleavage plane is coated with a highly reflective coating, while the front cleavage plain is left uncoated [Hobbs09]. Popular consumer products that contain laser diodes, like CD and DVD players, have significantly reduced the cost of these devices.

Many commercial laser diodes are manufactured with an integrated photo-sensor to determine the intensity of the radiated light. This is useful when designing laser diode drivers, as the "monitor" signal can be used in an electronic feedback loop to stabilize the intensity of the output light, which can vary significantly with temperature. Thus the package generally has three leads- one for injecting current into the laser diode, one for the signal originating from the monitor photodiode, and a ground common to both lines. The response time of a laser diode to a change in input current is extremely fast; gigahertz transmission rates with fiber-optic cables over long distances are a common application for diode lasers.

Although mechanically rugged, laser diodes are extremely sensitive to static discharge, significantly more than "normal" semiconductor devices. The relatively small charges that can build

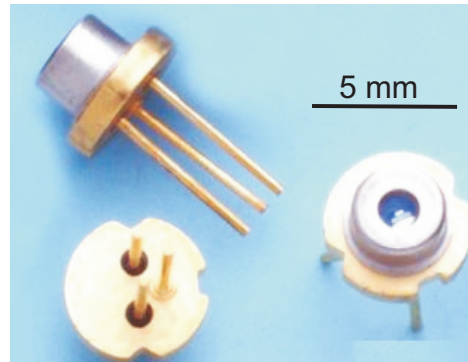


Figure 4.1: A typical laser diode.

up in a small pair of plastic tweezers can be strong enough to cause catastrophic optical damage [Goldwasser11]. It is absolutely necessary when handling these devices to prevent static build-up, preferably by using only metalized or conductive tools and by wearing an anti-static wrist strap. Care must be taken when designing a laser diode driver circuit never to exceed the manufacturer's specifications.

Due to the divergent nature of the emitted beam, laser diodes must be collimated and focused using one or more lenses. However, without additional correction, the beam profile will have an elliptical shape due to a different divergence angle on the X and Y axis, and will suffer from astigmatism on these same axis. When these problems are corrected with the proper optical components and an ideal, single mode beam is emitted, diffraction limited optical performance can be achieved [v.Pfeil02].

4.1.1 Laser Diode Noise Origins

Laser diodes can suffer from a variety of different types of noise which, if left uncorrected, will quickly become the performance bottleneck of any AFM. Their noise is caused by different effects: the intensity dependent shot noise, noise due to optical feedback originating from reflections in the optics, noise due to temperature drifts, and the often observed flicker noise inherent to all electronic devices. Shot noise can only be reduced when the intensity of the laser is increased. However, the noise originating from optical feedback and temperature drifts can be controlled. Both the noises of optical feedback and temperature drift influence the stability of a particular longitudinal laser mode [Lau84]. In semiconductor lasers, many different modes, each with slightly shifted wavelength, can be stable. These modes will compete, so only one mode will be active at a time, and which mode this is will be determined by the injection current, the temperature and the optical reflectivity- all at the same time. If these parameters are not precisely regulated, uncontrollable "jumps" from one mode to another can occur.

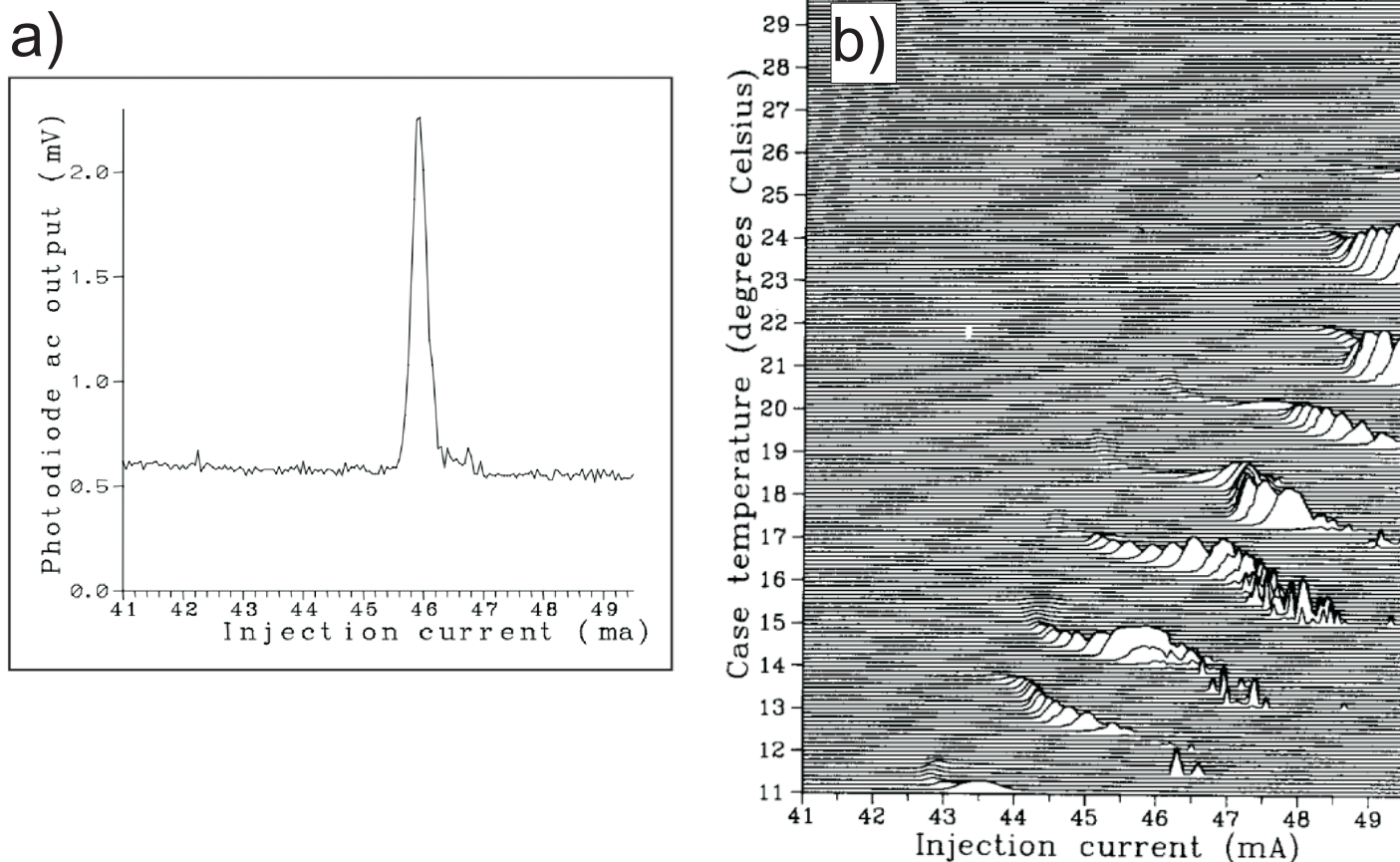


Figure 4.2: a) By sweeping the injection current, a region of laser instability can be found, where the temperature, back reflections and injection current combine ideally to initiate mode hopping. This is detected as an AC signal from an observing photodiode. b) By additionally sweeping the temperature, a 2-dimensional "stability map" can be created, showing the locations of the regions of instability. ©[1993] IEEE. These images are unedited with permission from [Heumier93].

Figure 4.2a details exactly how such a mode hop can occur on an arbitrary laser diode (images taken from [Heumier93]). At some point during a sweep of the injection current, the three parameters reach a critical point where mode stability is no longer guaranteed. This happens when the injection current reaches the value around the peak of the curve. In figure 4.2b, a series of the injection current sweeps from Figure 4.2a is shown, where the temperature is controlled and slightly increased after each sweep. All optical surfaces used for the measurement were slightly tilted in order to minimize laser back reflections. A "stability map" is generated, showing precise locations where the laser is stable, and where the regions of highest mode hopping are. When the operating point is in one of these unstable regions, slightly tweaking the temperature or injection current one can push the laser out of these regions of instability. Similarly, Figure 4.3 shows the onset of mode hopping in a calibrated AFM when the laser power is increased. The

height of the thermal peak in the spectrum of an Olympus AC200 cantilever is recorded, which is essentially an alternate method of measuring signal to noise and noise floor values. With increasing laser power, shot noise decreases and signal to noise levels increase. At a certain point (in this case at laser power ≈ 1 mW) the injection current is high enough to induce mode hopping, which will causes sudden drops and recoveries of the thermal peak height.

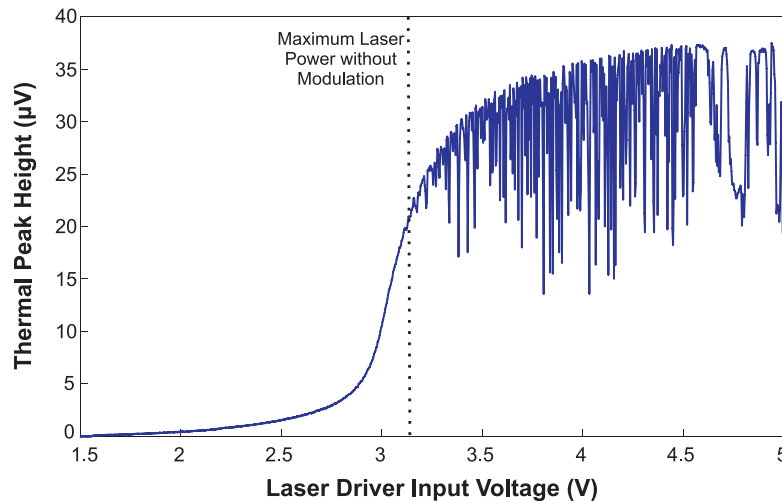


Figure 4.3: The onset of mode-hopping as the laser is power is increased. While the input voltage of the laser diode driver board is increased, the height of the thermal peak (peak height minus noise floor) is recorded. As the intensity is increased, the signal to noise is increased (i.e. the thermal peak gets taller). Mode hopping occurs after a particular laser diode output power level (dotted line, approximately 1 mW output power for current laser diode) is surpassed, resulting in sudden jumps of the noise floor and thus sudden decreases in the height of the thermal peak.

4.1.2 Effects of Mode Hopping in AFM

Mode hopping will have two particularly intrusive effects in optical beam deflection AFM. During the mode hop, the intensity of the output laser light will fluctuate. This intensity fluctuation will be removed by the normalizer in discussed in Chapter 3.3.2. Secondly, the mode hop will cause slight angle changes in the output light, which will propagate all the way to the photodiodes and will incorrectly be interpreted as discrete shifts of a deflecting cantilever. The frequency of these hops is unpredictable. Additionally, optical feedback caused by the incident laser light will occur when scanning large scan areas with a significant amount of topography.

This is visualized in the time domain representation of the vertical deflection in Figure 4.4a, where the lower curve shows a low frequency mode hopping effect, and the upper curve visualizes higher frequency mode hops. Figure 4.4b shows the effect of mode hopping through observation of the vertical deflection spectrum. The blue curve is the spectrum of the vertical deflection when no mode hopping takes place. It can be seen that the noise floor around the

thermal peak of an Arrow-UHF cantilever rises when mode hopping occurs.

In Figures 4.4c and d, force distance curves are displayed. Mode hopping, which is active in Figure 4.4d, will significantly distort the measured amplitude when compared to the clean approach curve in Figure 4.4c. This will be coupled into any controller, causing significant noise on all measured images.

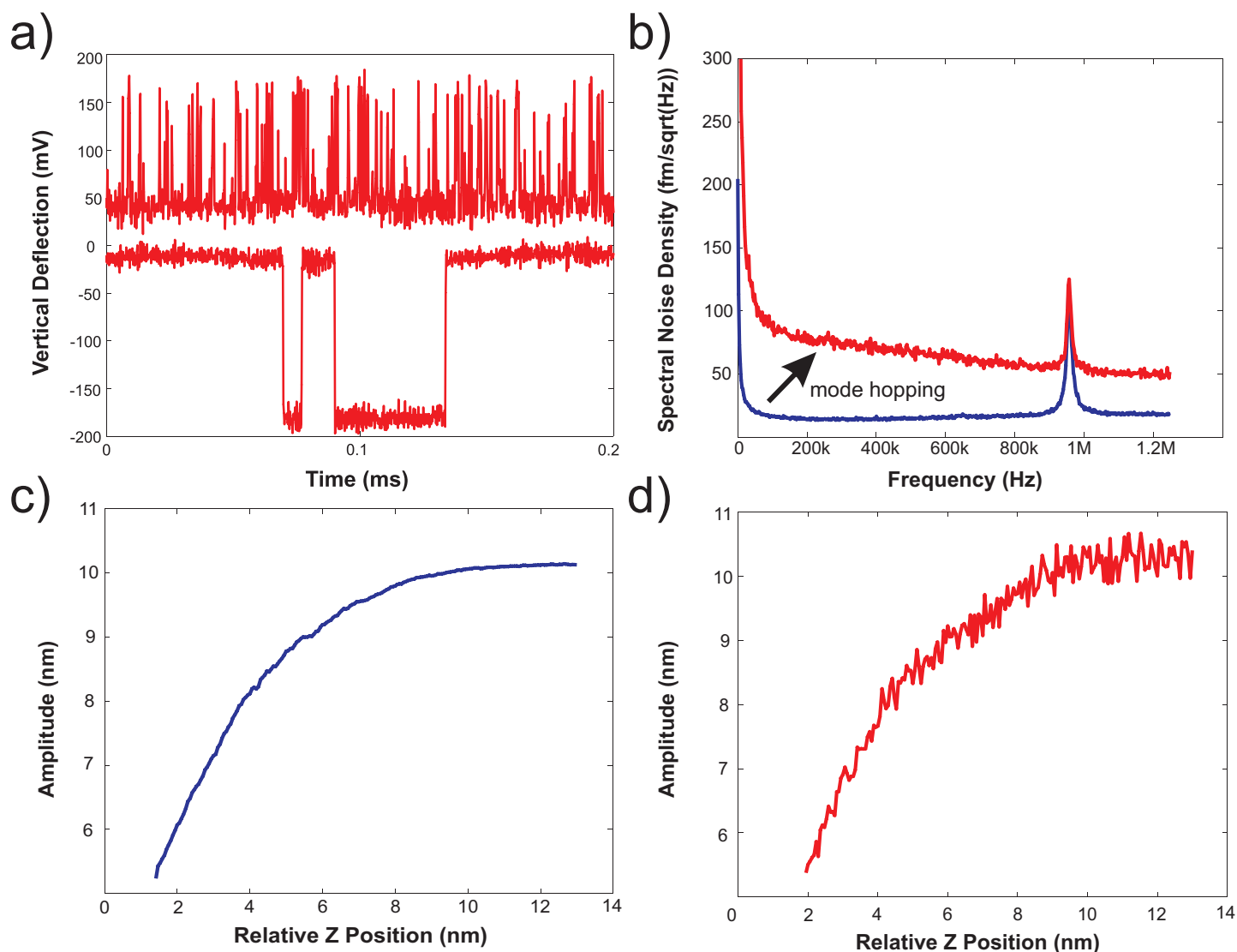


Figure 4.4: a) Time domain visualization of laser mode hopping. Mode hops will usually displace the vertical deflection signal by a few hundred millivolt. The probability of a mode hop occurring is entirely random, with a high-frequency hopping occurring on the upper line, and lower frequency hops occurring in the lower line. b) Frequency domain visualization of mode hopping, which will cause shifts in spectral noise, significantly increasing the noise floor. The blue curves shows a thermal spectrum of an Arrow-UHF cantilever with a silent laser, while the red curve is experiencing mode hopping. c) A mode hopping free force distance curve, and d) the same curve when mode hopping is occurring.

4.1.3 Laser Diode Driver

Laser diodes are extremely efficient at converting electrical signals into optical signals. It is very important to have a proper diode driver circuit that is a) low in current noise, as this would couple directly into the beam deflection noise, and b) never exposes the diode to conditions outside of the specifications, as this can cause instant laser diode damage or death [Libbrecht93, Lazar03].

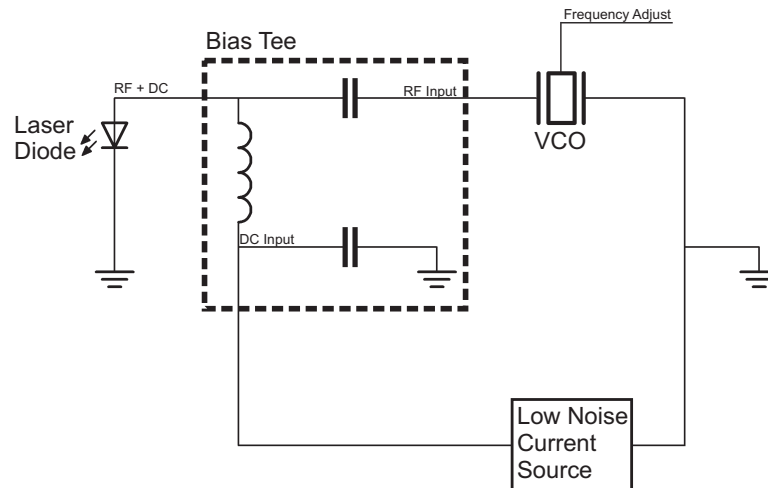


Figure 4.5: Schematic of a laser diode driver with the potential for high frequency modulation. A bias tee will add the high frequency oscillation (produced by the voltage controlled oscillator) on top of a low-noise DC signal (produced by the low noise current source).

Figure 4.5 shows the principle of the laser diode driver designed for reducing mode hop noise. A bias tee is used in conjunction with a Voltage Controlled Oscillator (VCO) and a low noise current source (based on the low noise laser diode driver proposal given in [Hobbs09]). The bias tee will add the high frequency signal originating from the VCO to the low current noise DC signal generated by the current source, resulting in a modulation of the laser diode, centered at the value of the DC current. For more details on the design of the laser diode driver, see Chapter 7. This high frequency modulation is very effective in reducing the mode hopping instabilities described previously. In addition, operation of the driver circuit using batteries is effective, removing power supply noise and line transients [Bradley90].

4.2 High Frequency Modulation

Modulating the laser diode with a high frequency signal is a method with which the intensity of mode-hopping can be reduced [Arimoto86, Nagai94, Fukuma05b]. Single mode laser diodes will initially oscillate in multiple modes for a few nanoseconds when the threshold is passed and lasing begins [Ojima86]. If the laser is driven by a high frequency train of pulses, these "turn-on" transients can be maintained continuously [Lau84].

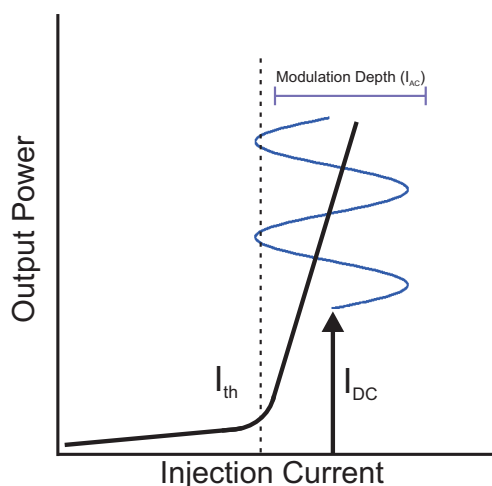


Figure 4.6: Schematic of a laser diode input current to output power relation. Below the threshold current lasing has not begun, and only very little light is produced. Above threshold, lasing begins, and the output light increases linearly with the injected current.

If multiple modes are oscillated simultaneously, it is not possible for mode hopping to occur; simultaneously the modulation signals will not cause unwanted spectral interference, as they are usually around 100 MHz - 1 GHz, well outside of the bandwidth of any deflection sensor. This modulation signal is added on top of an existing low noise DC injection current, which will determine the operating point of the laser and the intensity of the output light, as seen in Figure 4.6. To induce multimode operation the modulation depth of the signal should pass close to or below the threshold current; otherwise single mode operation will return [Lau84] and mode hopping will resume. This limits the maximum intensity of the laser where multimode operation is achieved to the depth of the modulation, and thus the output power of the high frequency oscillator used to generate the modulation signal.

4.2.1 Interference Reduction through Modulation

Due to the large coherence of the single mode laser diode radiation, sharp interference fringes can occur, causing artifacts in images and force distance curves. Multi-mode laser operation through diode modulation can significantly reduce the amount of interference [Kassies04], separating this noise out of the measurements.

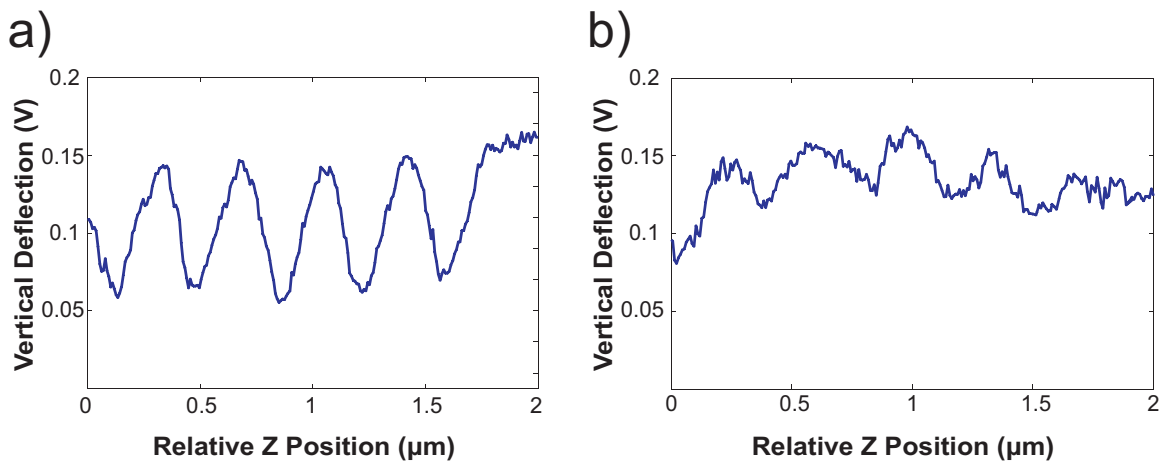


Figure 4.7: a) A force distance curve far above the sample. The oscillations are due to interference which is created between the cantilever and sample reflective surfaces. b) High frequency modulation of the laser diode causes the output to contain multiple laser modes, and leads to a reduction in coherence length, greatly reducing the artifacts created by interference.

This is due to the fact that when multiple laser modes are active, the coherence length is significantly reduced. Application of this method to eliminate interference reduces the need for post measurement processing, which can often lead to new, externally induced errors, if it is not entirely impossible. In Figure 4.7a, a force distance curve is executed far away from the surface, where no surface forces can influence the behavior of the cantilever. The pattern seen on the vertical deflection is due to the interference that is generated between the cantilever and the sample. In Figure 4.7b, the same curve is recorded with laser modulation running, showing only a small remaining interference pattern.

4.2.2 Noise Relationship

As with any system where shot noise is relevant, increasing the intensity of the output light will reduce the shot noise of the optical beam deflection system.

Modulating the laser diode, will reduce the effects of noise generated through thermally induced or optical feedback based mode hopping. However, we have repeatedly observed that modulating the laser diode will increase noise levels when compared to silent single mode operation. This is detailed in Figure 4.8, where the thermal spectrum of an Arrow-UHF cantilever is shown with (red) and without (blue) high frequency laser diode modulation. We believe this is due to an increase in aberration when multiple modes are oscillating, as the source light from the laser diode is no longer diverging from a single point, resulting in a departure from Gaussian optics. This optical blurring will propagate all the way to the photodiode, reducing the signal-to-noise ratio.

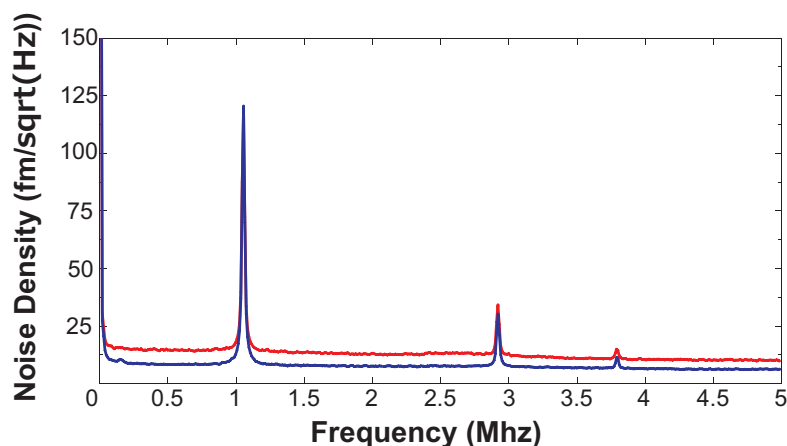


Figure 4.8: Effect of high frequency modulation on readout noise. The blue curve shows the thermal behavior of an Arrow-UHF cantilever without high frequency modulation, while the red curve is with modulation running, showing increased noise levels.

4.3 Conclusion

When properly controlled, laser diodes are an excellent, noise-free source of light for optical beam deflection atomic force microscopy. Their small size, simple integrability and high efficiency allow them to be placed directly in most AFM heads, reducing the potential for noise and vibrations originating in long mechanical paths. Laser diodes are extremely sensitive electrically, so proper care must be taken when designing a low noise laser diode driver. Ideally, the brighter they are, the lower the shot noise of the optical beam deflection setup will be, and the faster the readout will be. However, a laser diode will begin to mode hop when the injection currents reaches high values (and the case temperature and optical feedback parameters are

at the proper values), which will invariantly happen during regular operation of an AFM. Thus, it is a good solution for most applications to modulate the laser diode with a high frequency signal, in order to force the diode into a multi-mode operation where mode hopping can no longer take place. In addition, laser modulation decreases the interference noise in scanned images and force distance curves. The noise levels of a modulated laser will increase, as the beam quality of a multi-mode laser is inferior to that of a single mode laser. Thus, when scanning small scan ranges of only a few nanometers for high resolution imaging, it is beneficial to disable modulation and wait for the laser to stabilize thermally into single mode operation. Due to the small scan ranges in X, Y and Z dimensions, the optical feedback originating from the cantilever and sample will not change significantly enough to induce laser mode hopping.

Chapter 5

Small Cantilevers and High Resolution Imaging

It is necessary for a sharp tip to be in very close proximity to the surface in order to achieve high resolution topography images. However, this in itself is difficult to achieve due to a number of problems. In ambient conditions, when the attractive force gradient of the surface surpasses the spring constant of the cantilever (for example, due to a water film), the tip will jump to contact, potentially damaging the tip apex [Gan09]. Schwarz summarized the conditions necessary for atomic resolution scanning, as: 1) the interacting tip should be preferably atomically sharp, 2) the tip sample interaction in Z direction should drop rapidly, in order to avoid averaging by the increasing radius of the tip, 3) the sample provides a measurable, atomic scale lateral deviation, and 4) the interaction signal is stable enough over a small distance so that no instabilities occur when the feedback controller deviates slightly from the chosen setpoint [Schwarz00]. Schwarz continues by stating that by using frequency modulation with large amplitudes ($>1\text{nm}$), the jump to contact is avoided due to the increase in force caused by the oscillation amplitude of the cantilever (Hooke's Law), allowing the point of closest approach between the tip and the sample to reach 0.3 to 0.6 nm, in the non-contact region of operation.

However, as mentioned in Section 2.7.6, when oscillation amplitudes can be held small and in the short range interaction region of the surface, the spatial resolution will improve. It has been shown experimentally that reducing cantilever amplitudes to fractions of a nanometer (the length of a chemical bond) the spatial resolution of topography imaging can significantly be improved [Fukuma05a]. Strong repulsive contact forces cause elastic or even plastic deformations and should be avoided if true atomic resolution is desired; thus, cantilevers with force constants larger than the largest potentially experienced force gradient are necessary to avoid jump to contact during small amplitude imaging [Heuberger96, Giessibl99, Hoelscher00, Gotsmann01]. This can be done by either using stiffer cantilevers, or by reducing the tip sample attractive

force gradient. An example of the latter would be to image in an aqueous electrolyte solution in order to neutralize the effect of water film induced capillary forces and interfacial double layers [Ohnesorge93, Sokolov00]. Reducing cantilever length or increasing cantilever thickness will significantly increase spring constants (according to Equation 2.11), which will simultaneously increase resonance frequencies and improve the detection of small amplitudes. Additionally, a strong increase in lever stiffness can be achieved by using higher order eigenmodes [Melcher07, Knoll10, Lozano10], which can be advantageous for high resolution imaging [Kawai09]. Using higher eigenmodes it is possible to probe the surface using very small amplitudes without the danger of jumping-to-contact.

5.1 Spectral Noise Density Measurements

Thermal Brownian motion of the cantilever sets the limit for the smallest drivable eigenmode amplitudes and smallest detectable forces [Butt95, Walters96, Mamin01] in ambient conditions. The spectral response of a cantilever induced by thermal energy as a function of frequency f is given as [Albrecht91]:

$$N_{Thermal} = \sqrt{\frac{2k_B T}{\pi f_0 k_z Q [1 - (\frac{f}{f_0})^2]^2 + [\frac{f}{f_0 Q}]^2}} \quad (5.1)$$

where $k_B T$ is the thermal energy, f_0 is the fundamental resonance frequency, k_z is the spring constant, Q is the oscillation's Q factor. As f_0 and k_z are increased, the effective cantilever motion due to thermal energy is reduced, allowing the operation of smaller cantilever amplitudes. Figure 3.10b shows the thermal induced peak of an Arrow-UHF cantilever in air, and the corresponding theoretical fit of Formula 5.1 using f_0 of 1.53 MHz, k_z of 30 N/m and a Q of 115. Similarly, Figure 5.1 shows the thermal peak of a prototype USC-Si 5MHz small dimensional cantilever (Nanoworld AG, Neuchatel, Switzerland), which is to our knowledge the highest frequency thermal peak ever measured directly.

5.2 Small Dimensional Cantilevers

Three different types of small dimensional cantilevers were available for characterization and imaging. All were provided by Nanosensors, namely the "Ultra Short Quartz-like" (USNMCB) series of prototype cantilevers, the "Ultra Short Silicon" (USCSi) series of prototype cantilevers, and the commercial Arrow-UHF cantilevers. The tips of the USNMCB and USCSi cantilevers

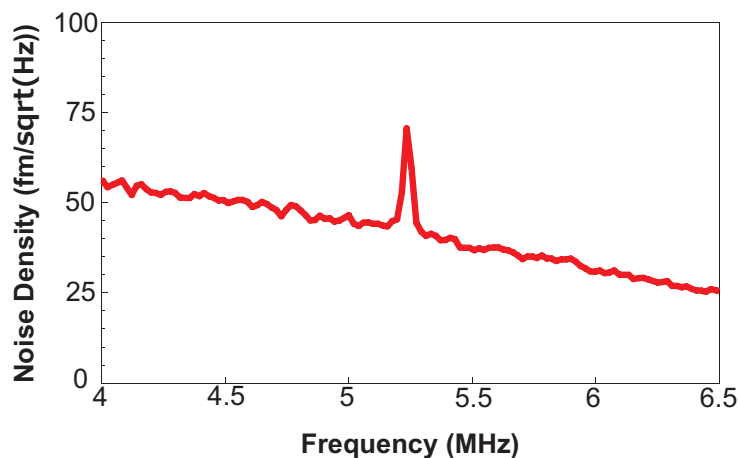


Figure 5.1: Thermal Peak of a USCSCI-5MHz prototype cantilever, centered at 5.235 MHz.

are single spike high density carbon, generated by a focused ion beam (Nanotools GmbH, Munich, Germany). The fundamental frequencies of these cantilevers were all designed and rated between 1.5 and 5 MHz (the most recent data sheets offer cantilevers up to 25 MHz). The USNMCB and USCSi cantilevers are rectangular, while the Arrow-UHF type is a solid triangle. The lateral dimensions of the beam shaped cantilevers are relatively small (Length: 10-20 μm , Width: 3-7 μm) when compared with the dimensions of "normal" cantilevers (Length 150 - 250 μm , Width: 40 - 60 μm). The tip radii of these cantilevers is given as $<10\text{nm}$, while the tip height is given as $\sim 2\ \mu\text{m}$. In addition to the benefits of higher resonance frequencies and more sensitive angle detection mentioned previously, smaller cantilever surface areas will improve the Q-factor of the oscillation due to the reduction in drag [Bhiladvala04] and squeeze film damping when approaching a surface [Hosaka95, Sulchek00, Basak06]. Q-factors of well over 1000 have been recorded for small dimensional cantilevers in air, confirming expected values calculated by Bhiladvala.

Figure 5.3 details the effective reduction in noise as the length of the cantilever is reduced. When the cantilever size is smaller than the focal spot size of the incident laser beam, much of the light will pass over the beam and be lost, resulting in a drop in the total light reaching the photodetector (i.e. a drop in the sum signal), and thus an increase in noise. Without any improvements in beam deflection optics of the Multimode AFM, scanning with very small cantilevers remains difficult; aligning the laser with the cantilever is sensitive, and thermal drifts in the optical head and beam positioning mechanics can cause the onset of misalignment and signal loss in the middle of a scan. The most effective small dimensional cantilever for our system was found to be the Arrow-UHF type of cantilever. The triangular shape of this small cantilever increased the surface area relative to the rectangular beams, which aided in beam positioning and the stability of optical alignment. In addition, its 1.5 MHz region is within the bandwidth of

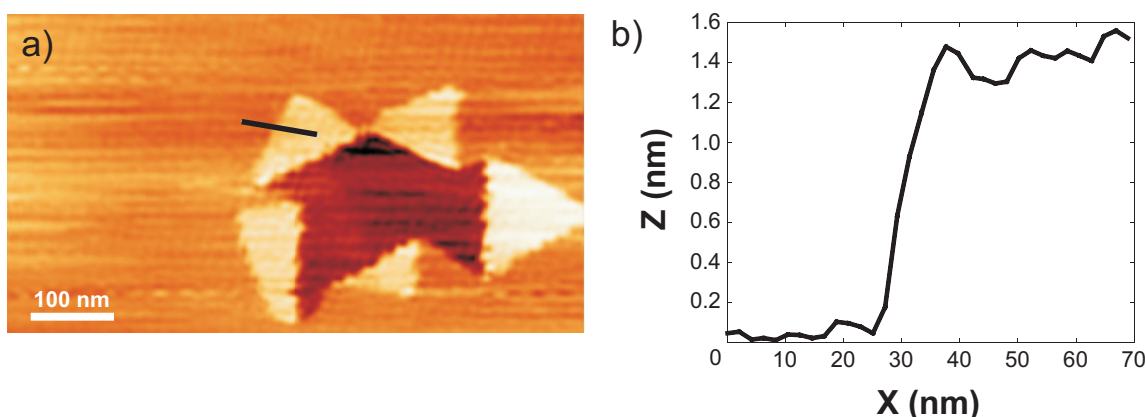


Figure 5.2: a) Topography image of an HOPG "flower" using a USNMCB cantilever where approximately 4 layers of graphite have been broken and folded, most likely during sample cleaving. Scan size: 690 nm x 380 nm; $f_0 = 3.73\text{MHz}$, $Q = 3749$, $A = 4.24\text{ nm}$. b) Line profile of the dark bar in a), showing approximately 4 layers of graphite in topography.

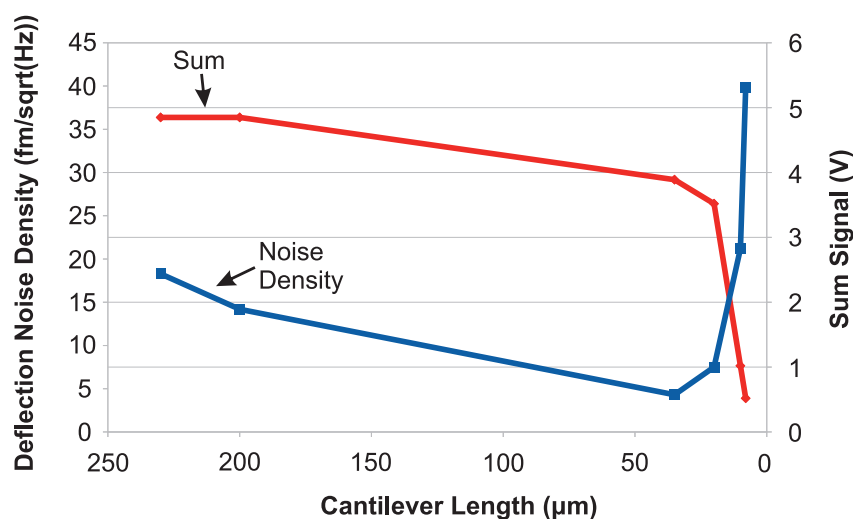


Figure 5.3: As the length of the cantilever is reduced, the deflection noise density will drop accordingly, until the cantilever is significantly smaller than the focal spot size of the incident laser beam. With cantilevers smaller than the beam waist ($\sim 20\mu\text{m}$), the total intensity of the light reaching the photodiode will drop, resulting in a significant loss of signal-to-noise.

the dither piezo used to actuate the cantilever; cantilevers with frequencies beyond 2 MHz become increasingly difficult to excite mechanically. An alternative would be to use photothermal actuation [Ramos06], a technique that has been used to excite mechanical resonators beyond 100 MHz [Verbridge06]. See Chapter 8 for more information.

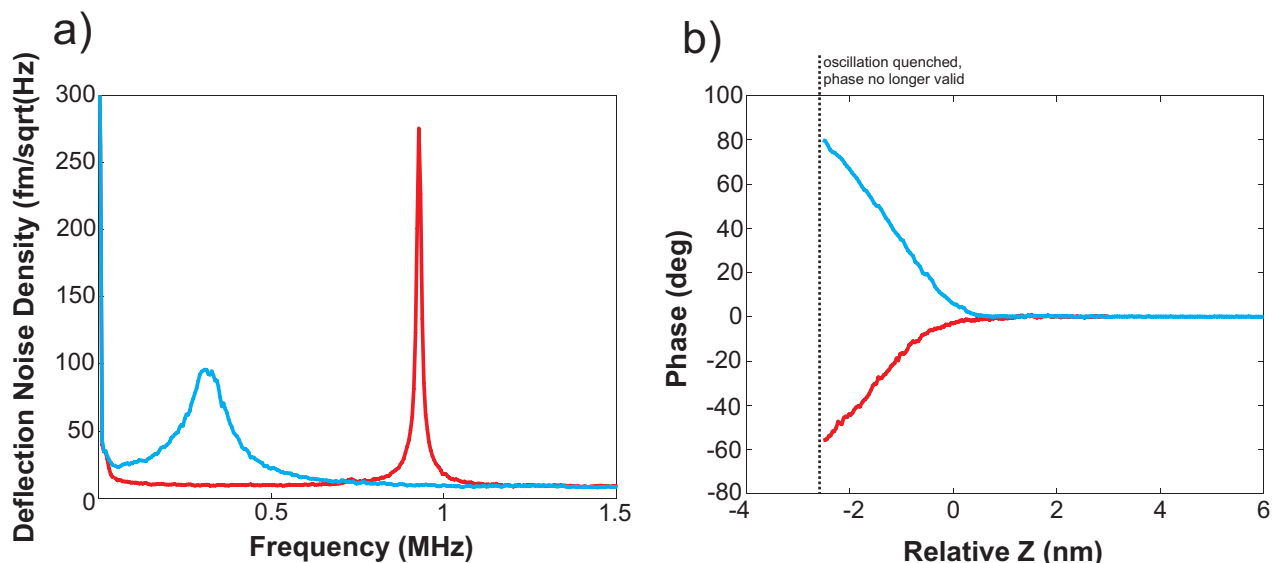


Figure 5.4: a) Thermal Brownian motion of an Arrow-UHF cantilever in air (red) and aqueous solution (blue). When the environment is switched from air to water, both the resonance frequency and Q-factor drop. b) A force-distance curve where the phase response of a dynamic cantilever in air (red) and aqueous solution (blue) is recorded. The free amplitude of both oscillations is 2.5 nm. In air, the cantilever never leaves the attractive (negative phase) region, while in solution the cantilever immediately enters repulsive (positive phase) region. Dotted line is where oscillation is quenched and phase becomes invalid. Aqueous solution consisted of 150mM KCl and 20mM Tris-HCl made using 18.2M Ω deionized water.

5.2.1 High Resolution Scanning in Ambient Environments

Achieving high resolution in air remains very challenging. High resolution images with contact mode scanning in air have been made on a variety of different ionic crystals [Shluger94], and on sheet silicates like muscovite mica (from this author's own experience with the Cypher microscope). Maganov has presented the only results where dynamic mode imaging produced high resolution in air on polydiacetylene crystals [Klinov04, Belikov06]. Using sharp, "carbon spike" probes with large amplitudes (~ 10 nm) and very light set-points (7-8nm) in AM scanning, images were achieved with true molecular resolution.

Tip - surface forces, most notably caused by capillary forces due to the water film in air environments, is the most commonly cited hindrance at achieving high resolution images in air [Gan09, Fukuma05d, Fukuma05a]. When approaching a surface with small amplitudes, it is not uncommon for the cantilever oscillations to decay within the attractive regime of the water film. This is shown in the force distance curve of Figure 5.4b, where the phase of an oscillating cantilever (free amplitude = 2.5 nm) is shown as a function of Z distance. When in air (red curve) the oscillation will never leave the attractive regime, until it is quenched; when the environment is switched to an aqueous buffer solution, the oscillation will immediately enter the repulsive regime of the surface. This indicates that in air the oscillating cantilever never reaches

a proximity close enough to the surface to generate contrast on the lateral atomic scale.

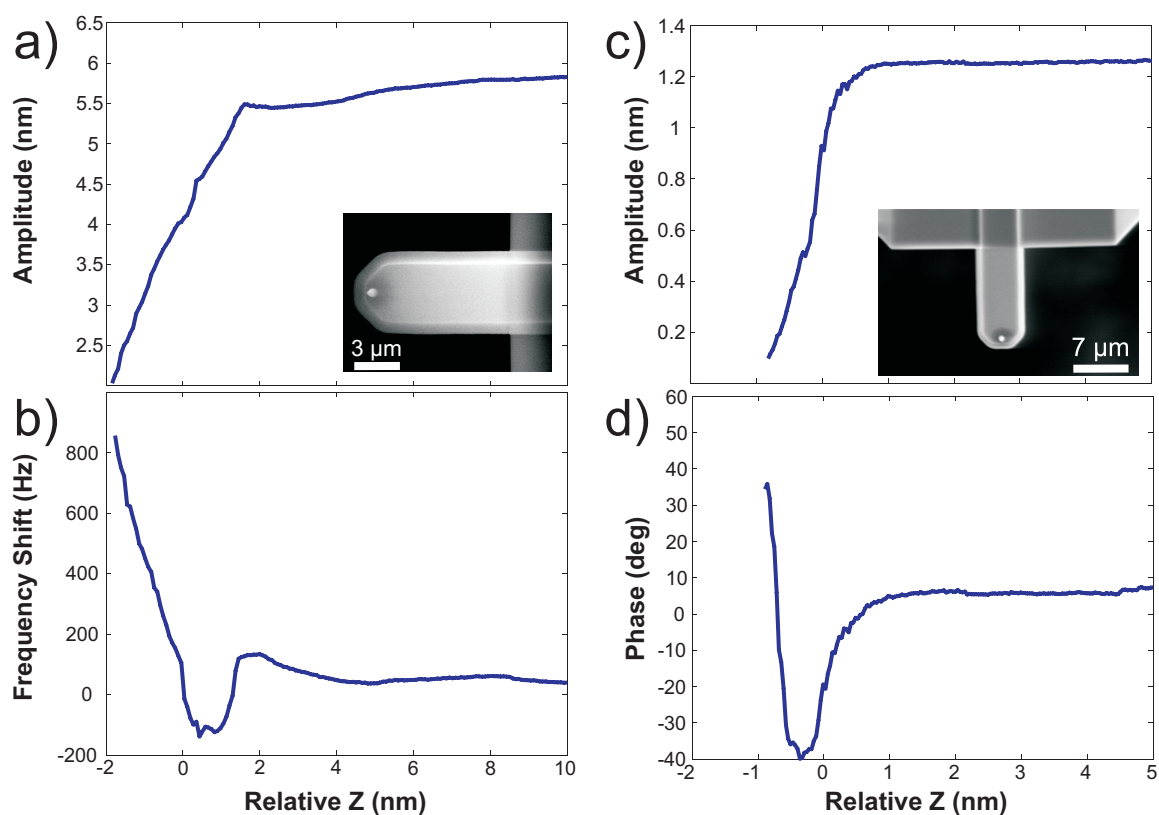


Figure 5.5: Small amplitude force distance curves of two USNMCB cantilevers. a and b): Amplitude and Frequency Shift of a USNMCB Prototype $f_0 = 5.17\text{MHz}$ c) and d): Amplitude and Phase of a USNMCB Prototype $f_0 = 3.58\text{MHz}$. Insets in a) and c) are SEM images of the corresponding cantilever.

Increasing the oscillation amplitude will increase the peak cantilever force enough to reach the repulsive region, as in the force distance curves of Figure 2.12, however this would be counterproductive for achieving a higher signal-to-noise ratio. Changing the scanning environment to liquid or aqueous environments resolves the problems associated with the water film; high resolution scanning in this environment is possible (see Section 5.2.3), however not all samples may be stable in aqueous environments, and the reduction in Q-factor, as seen in in Figure 5.4a, will again decrease the sensitivity and thus signal-to-noise of the oscillation. However, it was repeatedly seen that the Q-factor of small dimensional cantilevers in water remained well over 100, as opposed to dropping to 30 - 50 as is common with traditionally sized cantilevers.

Interestingly it was repeatedly observed that the USNMCB prototype cantilevers operating in air were able to reach the repulsive region, even with small oscillation amplitudes, as detailed in the force distance curves of Figure 5.5. In a) and b), a 5MHz USNMCB cantilever (a SEM image is shown in the inset) approaches the surface with the PLL running. An attractive and repulsive region can clearly be seen in the frequency shift signal. Similarly, in the phase of the 3.5MHz

USNMCB prototype shown in d), a steep repulsive region after a short range attractive region is shown. It is known that carbon surfaces have a reduced water film when compared with silicon oxide [Binggeli94]; a reduced water film on the carbon based cantilever and tip would reduce the susceptibility to capillary forces. This suggests that the USNMCB class of small, high frequency cantilevers could be used to achieve small-amplitude, high lateral resolution imaging in ambient AFM.

5.2.2 Atomic Resolution Imaging

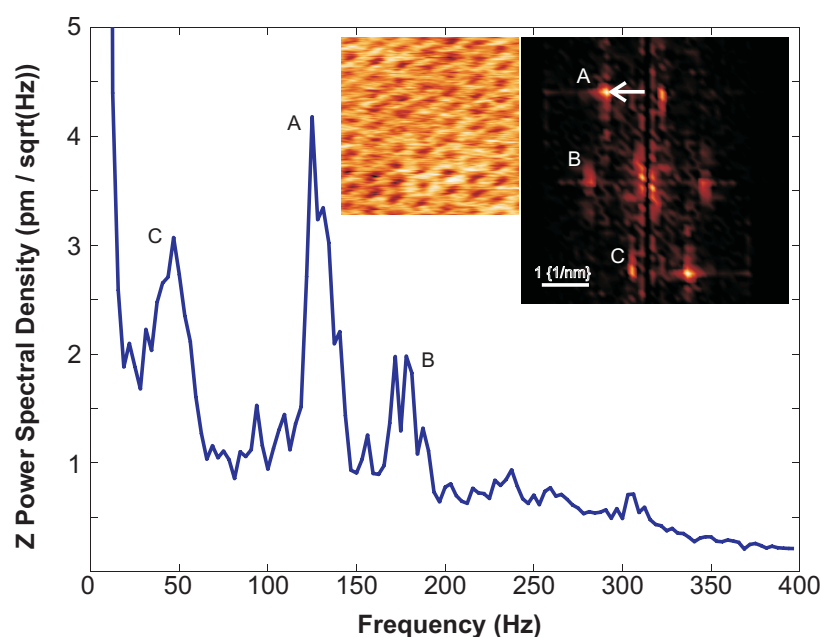


Figure 5.6: The spectral response of the Z-control loop during high resolution scanning of a mica surface with an Arrow-UHF cantilever. Small inset: Corresponding image; Scan size: 10nm x 10nm; Tip velocity: 160 nm/s; $f_0 = 511.9$ kHz, $A = 1.91$ nm; setpoint = +1657 Hz; Z-scale = 343 pm. Large inset: 2D-FFT of the image, showing the points A, B, and C, corresponding to the peaks shown in the spectrum at: $A = 125$ Hz, $B = 178$ Hz, $C = 47$ Hz.

To discriminate atomic resolution images from other periodic noise sources can be difficult and misleading. Improperly adjusted feedback loops can oscillate, however small, and can give the impression of a false positive atomic resolution image. Additionally, electronic noise originating from power supplies (50 Hz in Europe) can never be excluded entirely, and either the supply oscillation itself or a higher harmonic can quickly question the validity of the measured images.

Using frequency modulation in aqueous environments has proven an effective method to achieve high resolution images; here the Z-control loop holds the frequency shift to a constant value, giving true topography images. An alternate method is to measure with a constant height from the sample, where the atomic scale contrast would remain in the frequency shift sig-

nal [Fukuma05a]. In constant height mode, the Z-control loop is set very slow and passive, which will correct any slow thermal drifts, but will ignore any topographic features. It is important to always observe the behavior of the control loop that is attempting to generate the image; either the frequency shift in constant height mode, or the Z-control loop, when topography images are desired.

Figure 5.6 shows a spectral snapshot (0-400Hz) of the Z-control signal during atomic resolution topography scanning. The small inset shows the image of muscovite mica that was generated with this scan. The larger inset shows the 2-dimensional fast Fourier transform of the corresponding image. Both the image and the 2D-FFT seem somewhat elongated approximately in the Y-axis, this is most likely due to a lateral thermal drift of the sample during scanning. It is interesting to note that the peaks in the spectrum at 47 Hz, 125 Hz and 178 Hz correspond to the X-components of the three contrast points in the 2D-FFT (symbolized by the white arrow), when the tip velocity of 160 nm/s is taken into account. When changing the tip velocity, these peaks will shift in frequency; this is one direct indication that the periodicity is due to the surface, and not due to some unnamed noise source.

5.2.3 Selected High Resolution Images

The surfaces analyzed here are all well known and well characterized crystalline surfaces. HOPG, first seen in Figure 2.2 for STM, is an allotrope of carbon arranged in a hexagonal lattice which forms atomically flat sheet-like surfaces that can easily be cleaved with a piece of scotch tape. Muscovite mica is a hard mineral (commonly referred to as a sheet silicate) which is often used as a non-conductive, atomically flat substrate for AFM. Like HOPG, it has a near perfect basal cleavage plain, allowing cleaving with a piece of tape. It is with these simple and easy to use surfaces with which the capability of the low noise AFM is evaluated. All high resolution images shown in this section are FM-AFM images measured in 150mM KCl and 20mM Tris-HCl made using 18.2M Ω deionized water, using the original Multimode E-series scanner. Figure 5.7 shows a constant height atomic resolution image of muscovite mica, the first high resolution image obtained with this redesigned microscope. The cantilever used was a Nanosensors SSS-NCHR, which has a guaranteed tip radius <5nm.

HOPG has approximately half the lattice separation as mica, making it somewhat more difficult to image in ambient conditions. Lattice resolution was achieved using an Arrow-UHF cantilever in solution, as seen in Figure 5.8a. Figure 5.8b shows the 2D-FFT of the image in a, and when comparing it to the 2D-FFT of an STM image of HOPG (Figure 5.8c), it can be seen that a fundamental spectral component is missing to recreate a full hexagonal lattice; this can be due to an improperly terminated tip. Thus, only lattice resolution was achieved on HOPG.

A true topography image of muscovite mica was achieved, and can be seen in Figure 5.9a.

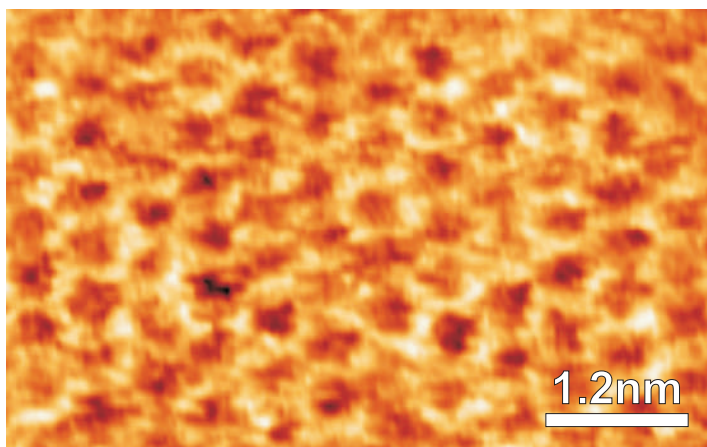


Figure 5.7: Atomic resolution image of freshly cleaved mica in solution. The image was acquired with a commercial cantilever (Nanosensors SSS-NCHR) using FM constant height mode ($f_0 = 126.4$ kHz, setpoint = +288 Hz, $A = 0.63$ nm, tip speed = 166 nm/s, scan size = 6 nm x 4 nm, Z-scale = 260 Hz).

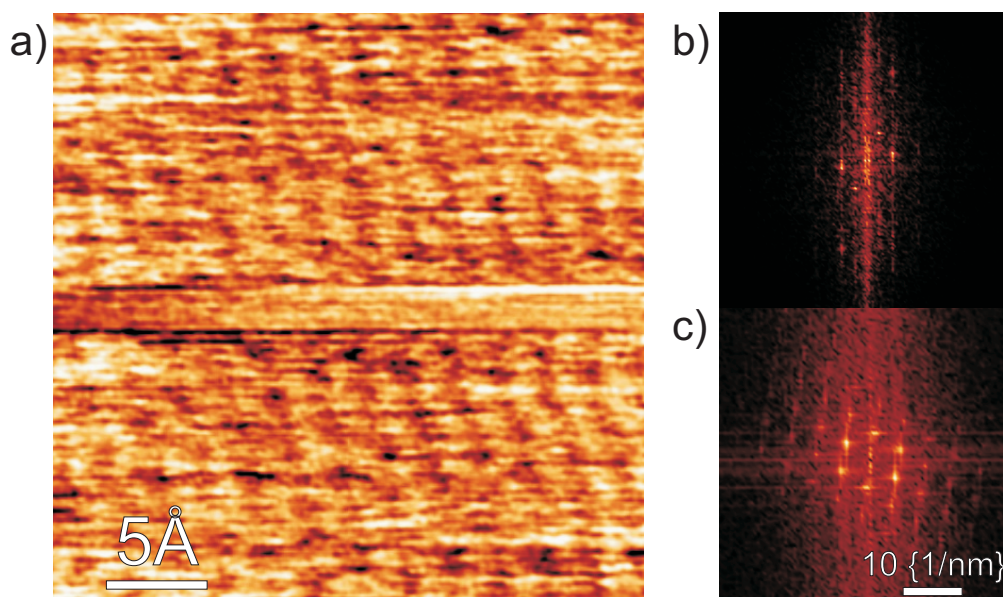


Figure 5.8: a) Lattice resolution image of freshly cleaved HOPG in solution. The image was acquired with a commercial cantilever (Nanosensors Arrow-UHF) using FM constant height mode ($f_0 = 469.6$ kHz, setpoint = +1097 Hz, $A = 0.48$ nm, tip speed = 175 nm/s, scan size = 3 nm x 3 nm, Z-scale = 71 Hz). b) 2D-FFT of image a). c) 2D-FFT of HOPG in Figure 2.2. When comparing b) with c), b) shows only two of the three spectral components needed to recreate a full hexagonal lattice. b) and c) have equal scale.

Again, the image was acquired in repulsive FM using an Arrow-UHF cantilever in solution. Figure 5.9b shows a ball-and-stick model of the mica surface, comprised primarily of silicon and oxygen.

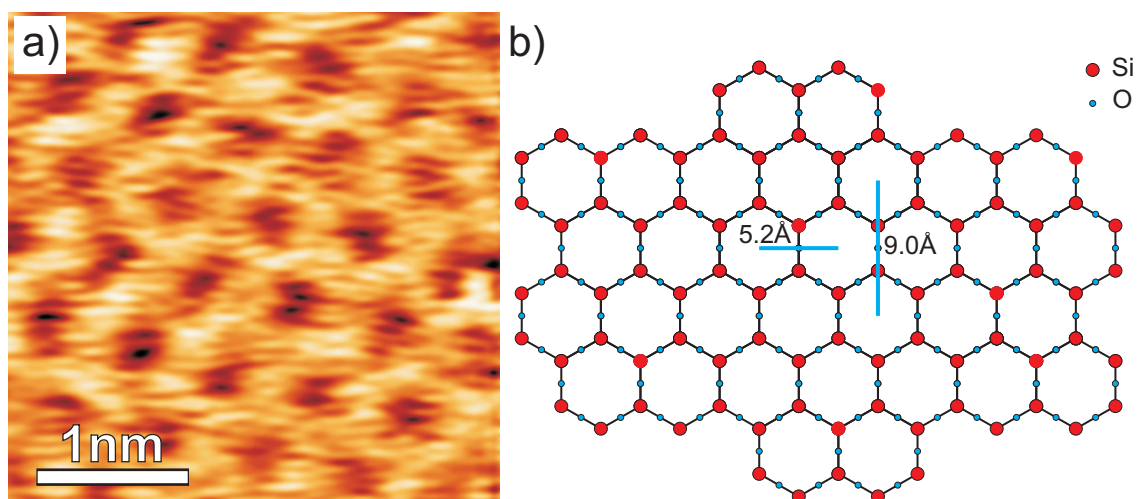


Figure 5.9: a) FM topography image of freshly cleaved mica in solution (150mM KCl and 20mM Tris-HCl in 18.2MΩ DI water). The image was acquired with a commercial cantilever (NanoSensors Arrow-UHF, $f_0 = 511.9$ kHz, setpoint = +1650 Hz, $A=1.58$ nm, tip speed = 160 nm/s, scan size = 3.5 nm x 3.5 nm, Z-scale = 83 pm). b) Ball-and-stick model of the mica surface.

5.3 Conclusion

In this chapter we demonstrated the practical realization of the translinear readout for AFM measurements and scans of the highest sensitivity. By using shorter, stiffer, higher frequency cantilevers, a spectral noise floor of $4.5 \frac{fm}{\sqrt{Hz}}$ was achieved. Such low noise levels permit the easily repeatable atomic resolution imaging of muscovite mica in liquid, which clearly demonstrates the potential of the new readout electronics. In addition, we show that small cantilevers can have significantly larger Q-factors in air, which would improve their FM sensitivity considerably. Surface water films remain a significant problem when attempting to scan high resolution in air. Small amplitudes are quenched by the capillary forces and thus not able to reach the surface. High density carbon cantilevers and tips are significantly more hydrophobic than the traditional silicon oxide cantilevers and tips, which may improve the limitations set by the water film. Using small dimensional carbon based USNMCB cantilevers, it has been repeatedly seen that the oscillation will enter the repulsive regime in air, even with small amplitudes. In combination with the measured high Q-factors and stable, efficient optics, these cantilevers may be capable of achieving very high resolution scanning in air. Finally, we show that it is a useful tool to observe the spectrum of the control loop during atomic resolution scanning, which can quickly reveal if the scanned image is an artifact or true topography. Maximizing the power of these peaks relative to the floor improves image quality, which can be done by adjusting control loop parameters and setpoints accordingly.

Chapter 6

Summary and Outlook

In AFM, contrast is generated by the mechanical interaction of a very sharp tip and an underlying sample. These interaction signals are undoubtedly small, and it is the task of the optical lever and electro-optical readout to amplify and convert these interactions into interpretable signals. The work presented in this thesis addresses the desire to continuously enhance the instrumentation of the atomic force microscope in order to achieve measurements with the highest possible sensitivity. Bandwidth and noise are the primary performance limitations of AFM signal processing electronics, and thus a significant bottleneck for the most demanding state-of-the-art applications.

The optical beam deflection readouts contained in most AFMs all require some form of arithmetic computation to generate a usable signal. This computation can be either analog or digital; analog computation is significantly closer to the continuous laws that govern physical interactions than digital computation, and can significantly improve bandwidth and noise values when skillfully implemented. When performing analog computations with currents as signals, a significant reduction in the amount of components is achieved- when compared to analog circuits with voltages as signals or digital circuits that perform the same computations [MacLennan07]. In addition, all computations occur virtually instantaneously with very little voltage variations, significantly increasing bandwidths of otherwise complicated computational setups [Fabre96]. This holds true for AFM instrumentation as well, as we have shown. In addition to AFM, the beam deflection technology developed here may be applied as a readout for MEMS resonators or other nano-mechanical devices, and any other technique requiring sensitive and fast measurements of laser deflection. A complete translinear readout outputting the vertical and horizontal deflections and sum signals was created using a small fraction of the components traditionally used in optical beam deflection AFM. Additionally, we show that the novel readout is low in noise and very fast, and predominately restricted only by the physical characteristics of the laser light source and the quadrant photodiode optical sensor.

Modulation of the laser diode will stabilize one of the most invasive sources of noise in optical beam deflection, the longitudinal mode-hopping of the output light. This is achieved by forcing the turn-on transients to exist continuously, where mode competition has not yet generated a dominant mode, any many modes are output simultaneously. Additionally this will reduce coherence length, resulting in a reduction in artifacts caused by laser interference. However, the beam quality is reduced, resulting in larger focal beam waists on the cantilever backside, and reductions in signal on the quadrant photodetector. Laser modulation is necessary when scanning large samples or when scanning significant amounts of topography, as the motion of the scan reflects the stray light passing the cantilever into the laser diode, which would otherwise induce significant mode hopping. The necessity for laser modulation can be avoided if the temperature of the laser source can be properly controlled, and optical back reflections are avoided, through the additions of (for example) active thermal feedback control and an efficient optical isolator.

Crosstalk and capacitive coupling between two contiguous, closely packed photodiode elements will reduce the sharpness of the signal and reduce signal to noise [Holloway86, Lee03, Moore06]. Removing crosstalk by separating the photodiodes from one another using a temperature drift compensated reflector as recently implemented by Prof. Paul Rutten of Maypa Technology [Rutten11] may further improve bandwidths and signal to noise by reducing crosstalk and junction capacitance. Additional improvements in bandwidth, noise and power dissipation will be obtained by integrating the entire translinear readout onto one integrated circuit chip, which will remove stray capacitances, line inductances, and noise created through imperfect soldering and contact points.

The beam deflection optics apart from the source and readout remain a severe limitation of the setup described in this work. The optics in this microscope do not correct the astigmatism of the X and Y axis of the laser diode light source, and the deviation in divergence angles is not corrected until directly before the quadrant photodiode, using a cylindrical lens. Inefficient optics and large focal spots will cause the loss of potential signal generating light, and can cause interference fringes in measurements and back reflections into the laser diode when light that passes the cantilever is reflected back from the sample. Improvements on this optical design would significantly reduce the current size of the focal spot ($\sim 20\mu\text{m}$, Figure 5.3) further stabilizing and improving the use of small dimensional cantilevers. Focal spot diameters of $\sim 1.3\mu\text{m}$ are possible using laser diode based optics, as we have shown with our optical tabletop photothermal excitation setup (see Section 8.2).

As the optical beam deflection measurement method is an angle detection method, the use of shorter cantilevers will improve the Z-deflection sensitivity without changing angular deflections and thus the measured signal strength. Additionally, the surface area of the prototype USNMCB and USCSi small dimensional cantilevers is reduced by two orders of magnitude when com-

pared to regular commercial cantilevers. This would improve resolution in local electric potential measurement techniques, as unwanted contributions by the cantilever beam are reduced [Jacobs98, Jacobs99]. Additionally, damping is reduced as well, improving Q-factors and thus the force sensitivity of the cantilevers [Viani99]. As Bhiladvala calculated [Bhiladvala04], long cantilevers with several micrometers in width will be significantly damped in air, while smaller scale beams will not.

Solving these remaining challenges will further improve the sensitivity and reproducibility of atomic force microscope measurements. Contrast is generated by the tip-sample interaction. In ambient conditions, predominately uncontrollable factors like thermal drifts, scanning environments and surface contaminations play a significant role at quenching a potentially strong interaction signal. It is the difficult role of the instrument developer to defuse these adversaries of high resolution imaging in ambient.

Chapter 7

Appendix A: AFM Instrumentation

7.1 Base Redesign

In order to achieve the goals set forth in this research project, a significant amount of the original Multimode AFM instrumentation had to be redesigned and improved upon. The Multimode 3a controller had already been replaced with a Nanonis controller by my predecessor [Ziegler09] and was interfaced with the original Multimode AFM base (Figure 7.1a) through the Nanonis Adaptation Kit for Multimode AFM microscopes. The Nanonis controller quickly revealed the weaknesses of the original Multimode base, which added numerous unwanted peaks to the vertical deflection, even with a disabled laser (Figure 7.1b). It was apparent that in order to utilize higher bandwidths, these peaks would create significant hurdles in the proper detection of oscillations.

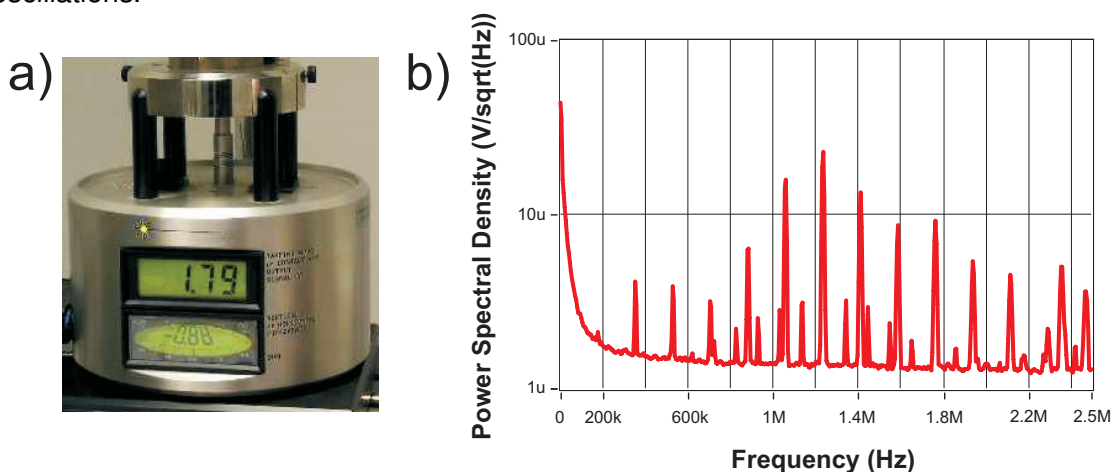


Figure 7.1: a) The original Multimode AFM base. In addition to a significant amount of electronics, the base contained a stepper motor for coarse tip - sample approach, and a socket holder for the scanner. b) Spectral response of the vertical deflection of the translinear readout on the original Multimode base with the laser disabled. Numerous undesired peaks and harmonics are generated by the internal electronics of the base, and are transmitted into the new readout through the common ground.

The base would have to be removed in order to relieve the problem of these spurious peaks. In order to do this, a replacement holder for the original Multimode AFM scanner had to be produced; this device was to include the scanner mount itself and an additional mount containing the stepper motor for coarse approach, which would be directly attached with the first mount using four 30 mm optical posts (Thorlabs, TR30/M-JP). The small brass tube with an internal hex key for M5 sized hex screws was obtained from Hartmann Modellbau (Dittelbrunn, Germany). Both the aluminum scanner mount and the base were manufactured in-house. The scanner mount can be seen in Figure 7.2, and the base which contained the stepper motor in Figure 7.3.

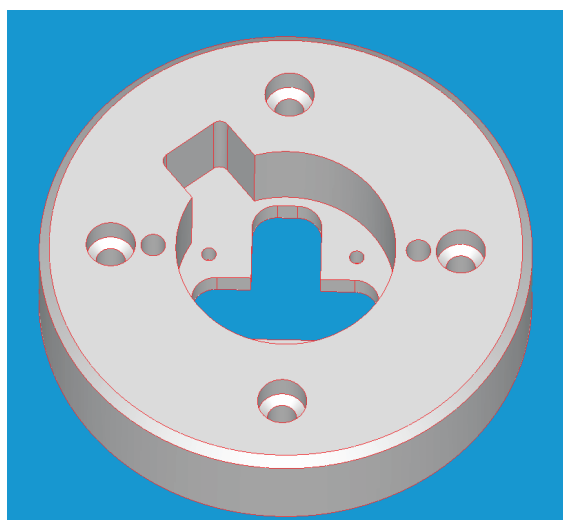


Figure 7.2: Replacement mount for the XYZ piezo scanner.

The stepper motor controls a fine micrometer screw that determines the tip sample distance. The stepper motor itself consisted of a Trinamic PD1-013-42 stepper motor with controller board. Sine cosine microstepping can be activated on this stepper, significantly increasing the resolution ($^{\circ}$ /step) which subsequently reduces the minimum step height per pulse of the approach. In Figure 7.4 we show that the average step height of one click when microstepping is active is approximately 18-20 nm.

The control board of the stepper was flashed using the technique detailed in [Tri08] with the following commands: AC 13 (reduce current to 13% of maximum, this will prevent stripping of the micrometer thread by the stepper) AM 1 (chopper mode 1) AZ 0 (maximum resolution) AA 0 (acceleration to 0, turn on step / direction mode) AW (save everything to the flash).

The combination of these components as a new base for the Multimode AFM solved all the problems the original base was creating. The complete base, with the scanner and microscope attached, can be seen in Figure 7.12.

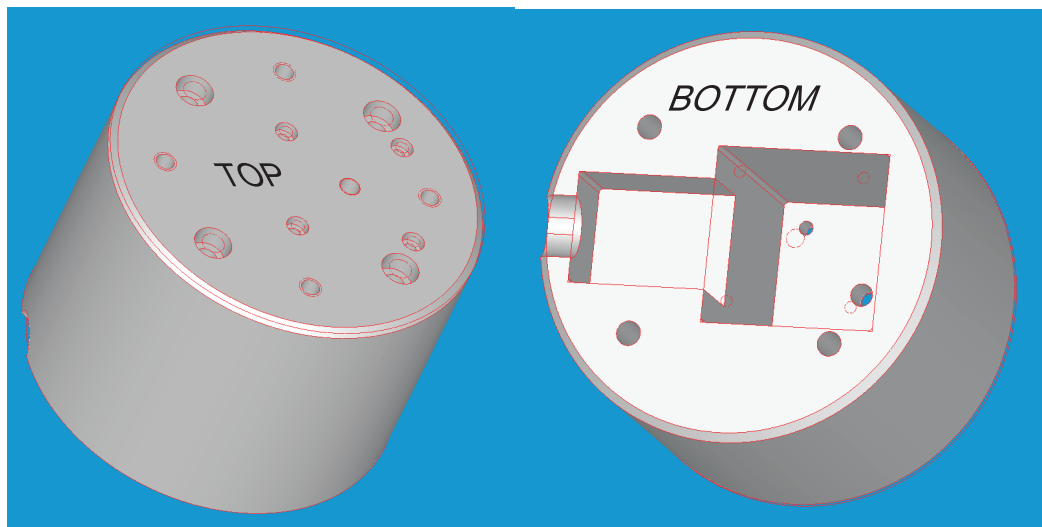


Figure 7.3: Replacement mount containing the stepper motor, which is attached below the XYZ piezo scanner replacement mount.

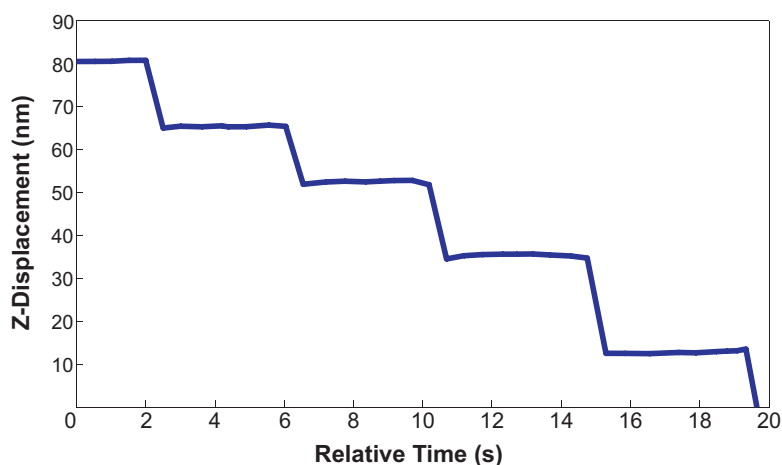


Figure 7.4: Step height of a the re-designed stepper motor for coarse approach. Smallest approach height is ≈ 18 nm. The Z-controller is regulating the tip-sample interaction in simple AM mode, while the stepper slowly retracts the sample.

7.2 Optical Redesign

In addition to the base, parts of the electro-optical system had to be redesigned as well. The original Multimode AFM quadrant photodiode was replaced with a commercial SD 085-23-21-021 by Advanced Photonix. The original custom made photodiode was directly mounted onto the micropositioner that is used to center the beam deflection optics; in order to accommodate the new photodiode, this micropositioner was redesigned, and is shown in Figure 7.5. The new, brass photodiode holder was again manufactured in-house. The hole spanning the length of the

device is threaded with a #6-80 micrometer thread, on which a stationary screw will move the micropositioner horizontally for beam deflection centering.

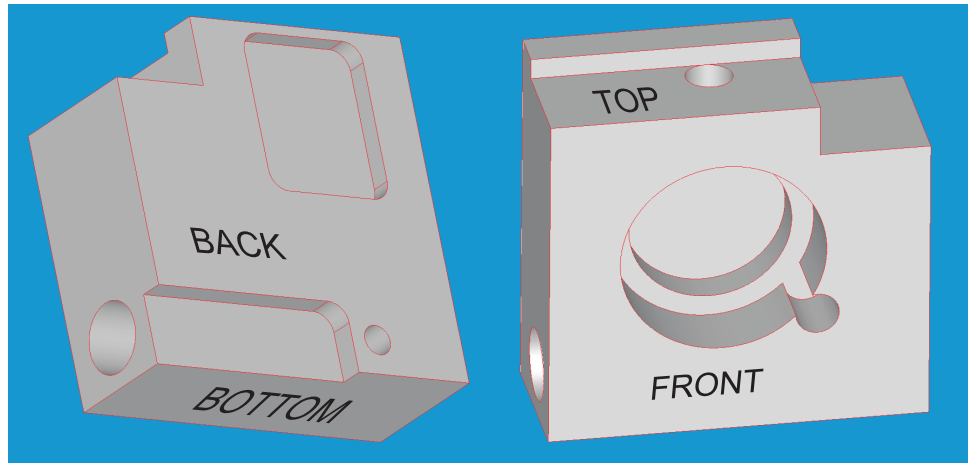


Figure 7.5: The re-designed photodiode holder. The trenches on the backside are for containing the motion stabilizing ball bearings (backside top), and for positioning the stabilizing spring (back bottom). The hole through the length of the device is threaded for a #6-80 (non-metric) micrometer thread. This thread controls the horizontal adjustment of the photodiode.

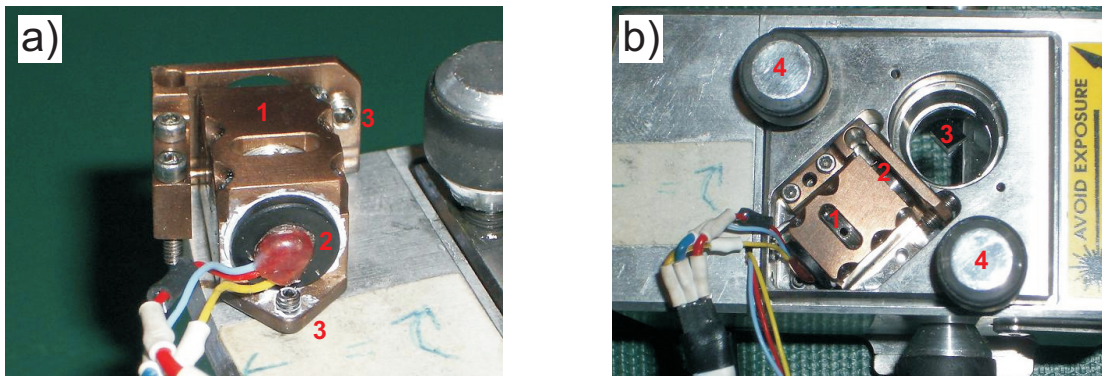


Figure 7.6: The collimator and optical positioning system for the beam deflection optics. a) The laser collimator (1), containing the optics for focusing the beam originating from the laser diode (2). The two grub screws (3) allow coarse adjustment of the X and Y laser pointing vector. b) Further insight into the optical system. An aspheric lens (1) collimates the laser beam, and passes it to a focusing lens (2), which will further pass the beam to the mirror (3). This mirror reflects the beam onto the cantilever below. The micrometer adjustment screws (4) act to position the beam onto the backside of the cantilever.

Although the original collimation and focusing optics remained, the laser diode used was an ADL-65055TL (Laser Components, Olching, Germany) and was replaced numerous times. In Figure 7.6a, the small tube which contained the laser diode is shown (2) inserted into the collimation mount (1). Due to the need for thermal stability when using laser diodes as light sources,

the diode was glued into the small tube using a heat conducting epoxy (EpoTek 930-4, Billerica, MA, USA), and the small tube was covered with a heat conducting paste before insertion into the collimation mount. Once inserted, the lenses need to be adjusted in order to properly focus the spot on the back of the cantilever. This is done by mounting one of the small dimensional cantilevers mentioned in Chapter 5 in the microscope. The lenses of the collimator are mounted inside of a threaded tube, which can be moved relative to the position of the laser diode (Figure 7.6b, (1) and (2)); these are adjusted, focusing on the small cantilever until a maximum in the Sum signal is reached. Apart from the laser source and the quadrant photodiode, the optics of the Multimode AFM were not modified in any other way.

7.3 Electronic Redesign

A schematic of the laser diode driver circuit used in this setup is shown in Figure 7.7, and the corresponding layout is in Figure 7.8. The concept is the same as the one that was explained in detail in Section 4.1.3; a low noise DC current source is interfaced with a high frequency signal originating from a Voltage Controlled Oscillator linked together through a bias tee. The VCO is a POS-400 (MiniCircuits, Brooklyn, NY, USA), linearly tunable from 200 to 380 MHz. The bias tee is a PBTC-1G (MiniCircuits) Wideband (10 - 1000 MHz) device, directly connected to the VCO and laser diode at its inputs and outputs. The feedback stabilized low noise current source is constructed based on the design given in [Hobbs09]. The DC current and thus the laser intensity is controlled through an external input signal drives the setpoint of the low noise feedback control. This input signal originates on an onboard optocoupler; thus, the capability of driving the laser diode driver circuit with an independent power source (such as batteries) remains, decoupling the laser from a potentially noisy power source.

The schematic design of the translinear readout used in this setup is shown in Figure 7.9. Figure 7.9a is the schematic of the voltage stabilizer, and consists of the following parts: A: Positive Transistor Voltage Regulator, LP2954 (National Semiconductor), for +3.5V supply for the transistors; B: Negative Transistor Voltage Regulator, LM337 (National Semiconductor), for the -4V supply of the transistors; C: high speed differential amplifier (AD8132, Analog Devices) for the photodiode emulation circuit; D: Positive op-amp voltage regulator, MC78M12 (ON Semiconductor), for +12V supply of the op-amps; E: Negative op-amp voltage regulator, MC79M12 (ON Semiconductor), for -12V supply of the op-amps; F: Positive +10V low noise voltage reference, LT1236 (Linear Technology), for reverse biasing of the quadrant photodiode. Figure 7.9b is the schematic of the translinear readout, and consisted of the following parts: Ultra high frequency transistor arrays HFA3127 and HFA3128 (Intersil) for the NPN and PNP transistors, respectively; the transimpedance amplifiers for the vertical, horizontal, and sum signal lines were the THS4011 (Texas Instruments) class of voltage feedback amplifiers.

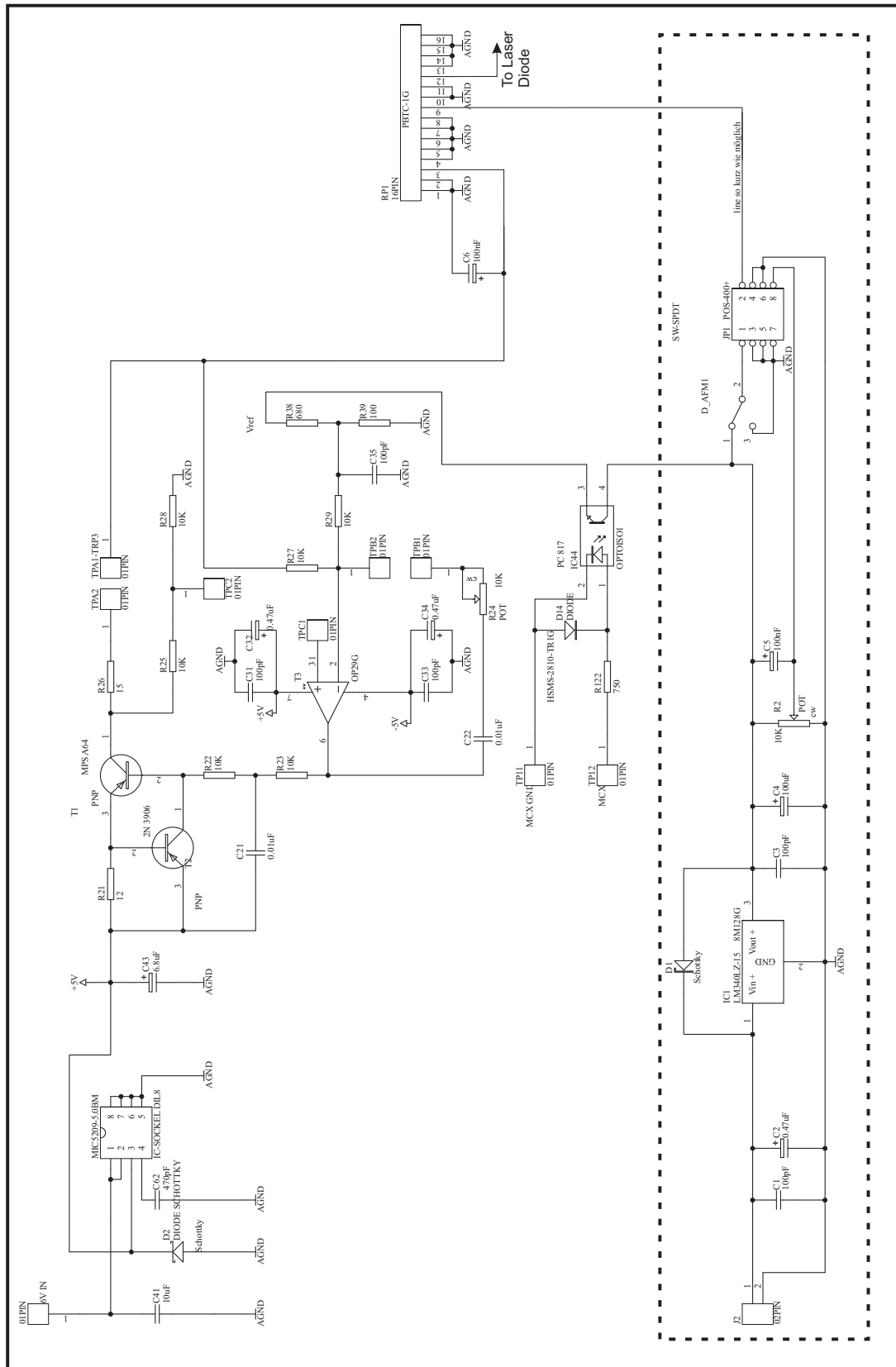


Figure 7.7: Schematic of the low current noise laser diode driver used in the setup. The dotted box details the circuit for high frequency laser diode modulation for elimination of mode hopping. The remaining circuit details the feedback stabilized low noise current source for the DC portion of the laser diode injection current. To the right is the bias tee, which combines both DC and AC signals together and feeds them to the laser diode.

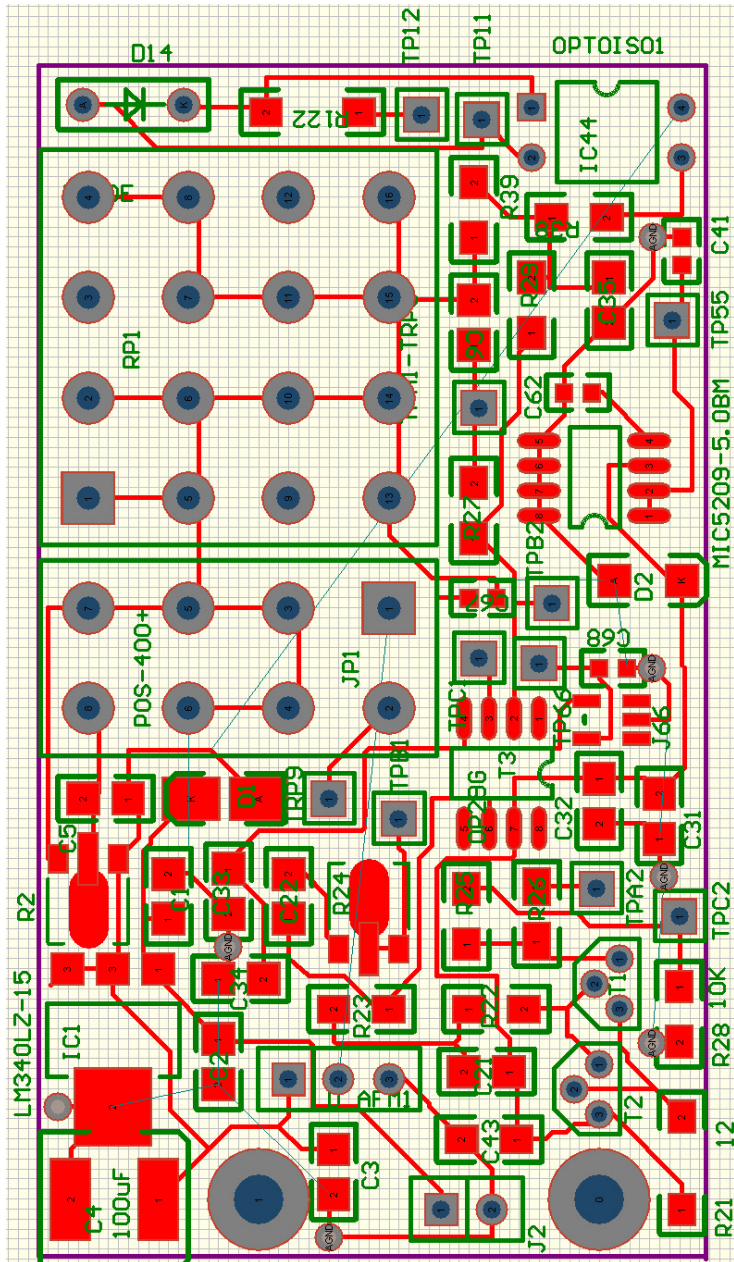


Figure 7.8: Layout of the low current noise laser diode driver used in the setup. The large square component in the upper left corner is the bias tee, right below that is the VCO. The remaining circuit is for power supply stabilization and generating the feedback controlled low noise DC injection current.

The layouts of the power stabilizer and dual channel translinear circuit are shown in Figure 7.10 a and b, respectively. These layouts were prototyped with a precision mill, and cut from a copper double sided printed circuit board. Red lines indicate paths on the top board, while blue lines indicate paths on the opposite side. The lower side of the translinear readout does not host any signal paths at all, it is intended as a ground reference plain. This ground plane is crucial for

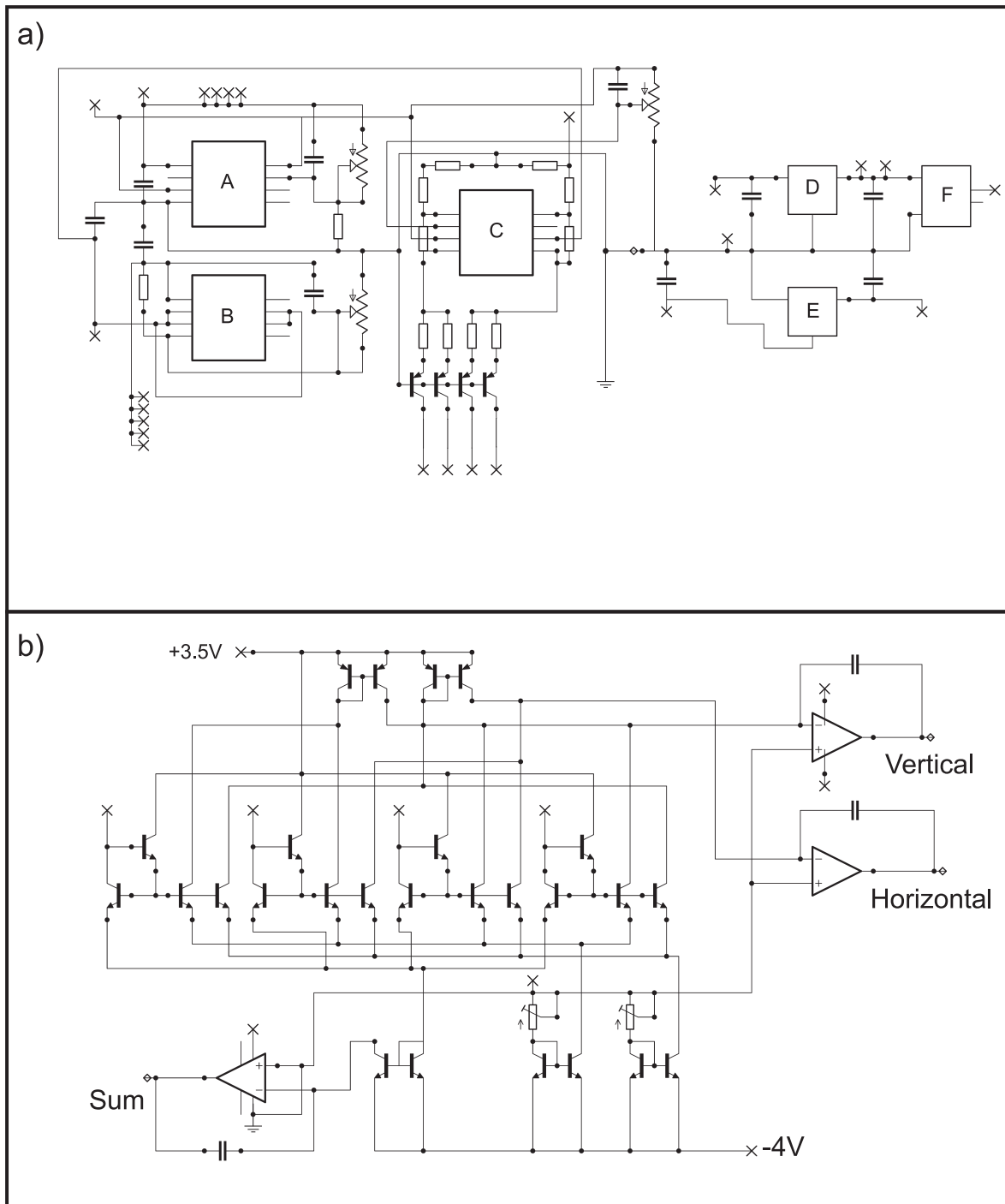


Figure 7.9: Translinear Readout schematic. a) Power supply stabilization board, including photodiode emulation circuit of Figure 3.6a. b) Complete two channel translinear readout.

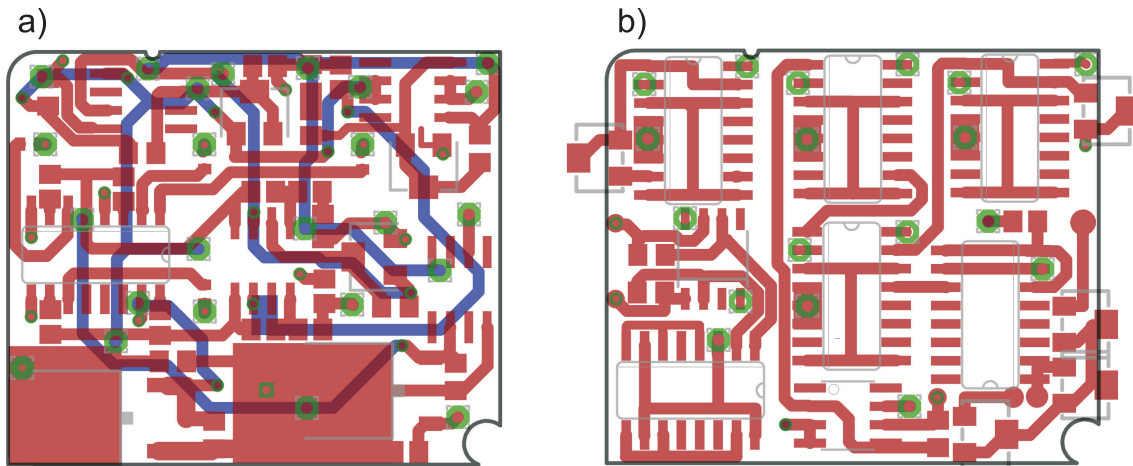


Figure 7.10: Translinear Readout layout. a) Power supply stabilization board, and b) complete two channel translinear readout.

the stable operation of translinear circuits, as the ill-defined voltages of the signal paths (after all, it's a current mode circuit, not voltage mode) will float and drift, which will be forwarded directly to the transimpedance amplifiers, causing low frequency drifts over the entire output range of the amp. Additionally, line inductances will be reduced, as currents traveling through the ground plane will travel in opposite direction as the signal currents. Only the shortest of lines on the translinear circuit have been designed into the board layout in b), as the line inductance is proportional to the length of the lead. More lines would not fit onto the PCB, thus all remaining lines were applied using miniature coax cable (Nexans 5633).

Figure 7.11 shows the plug which connects the AFM Head to the outside of the acoustic isolation box. lines A1 - A7 are independently shielded coaxial lines, while lines 1-17 are direct lines. All sensitive signals are routed through the coaxial lines, and follow the layout:

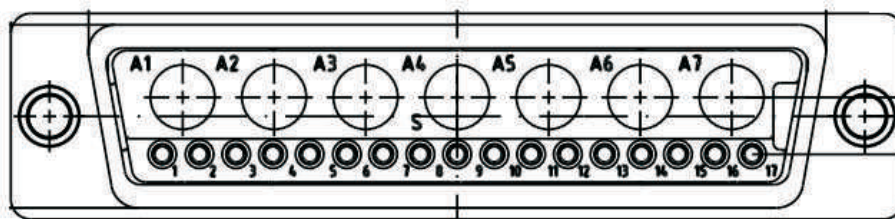


Figure 7.11: Interface plug between the AFM Head and the Nanonis controller.

Coaxial lines: A1: Sum (Output) A2: Vertical Deflection (Output) A3: Laser Intensity (Input) A4: Tunnel (Output) A5: Shake (Input) A6: Tip (Input) A7: Cap (Input, Mini D-sub Pin7, only for

Multimode scanners!)

Direct lines (all Inputs): 1: Laser +5V; 2: Readout +8V; 3: Laser -5V; 4: Readout -8V; 5: Readout GND; 6: Laser GND; 7: Readout +15V (reverse bias of photodiode); 8: Laser +15V (supply for high frequency modulation); 9: Auxilliary Yellow wire (NC); 10-17: Mini D-sub Pin1 - 9 (high voltage inputs for scanner control). In order to avoid ground loops, all output lines should be connected to the Nanonis controller with BNC cables with disconnected shields, while all input lines should feed the shield all the way to the microscope.

7.4 Conclusion

In this chapter we describe the method of how we solved many of the engineering problems that were keeping the original Multimode AFM microscope from becoming a truly low noise and sensitive AFM. Initially, we described how we removed the base, which plagued many measurements with unwanted noise, and replaced it with a simple homemade base, containing a commercial stepper motor. Subsequently we removed all of the original electronics from the head of the microscope, added our own laser driver and laser diode, and finally added the novel translinear readout to the system as well.

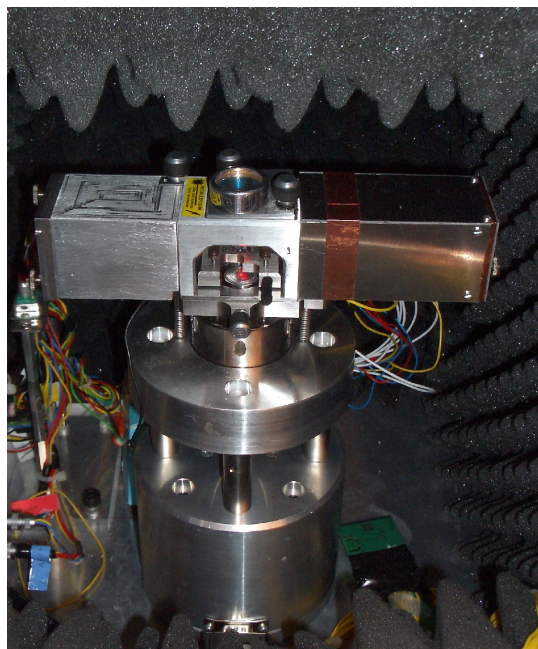


Figure 7.12: Complete microscope housed inside a homemade acoustic noise isolation box.

The complete microscope with all new parts can be seen in Figure 7.12. The new electronics are protected and shielded through the addition of aluminum covers, where are mechanically

sturdy and directly connected to the original Multimode head. The sensitive electronics are thus protected from any outside interference or mechanical mishandling.

Chapter 8

Appendix B: Photothermal Excitation

Mechanical excitation of cantilevers beyond a few MHz is challenging. Dither piezos not only shake the cantilever but also the entire chip, and, in worst case, the chip holder and other parts of the microscope as well. This is especially pronounced in liquid environments, where it is often difficult to determine the true cantilever oscillation peaks due to spurious off-resonance peaks [Kokavec07], known as the “forest of peaks”. This problem can be effectively bypassed by actuating the cantilever directly, which occurs when cantilevers are excited by a second, independent optical beam, which is a method known as photothermal excitation [Umeda91, Ratcliff98, Fukuma09, Nain10]. In addition to actuation, it has been shown that photothermally excited cantilevers can be used to regulate the tip to sample distance [Yamashita07], resulting in a faster response than can be achieved with conventional piezo actuator based Z-scanners. In order to accurately measure the bandwidth of the deflection sensor with small dimension high frequency cantilevers, a new optical tabletop OBD setup was designed with a near diffraction limited spot size. Due to the difficulty of actuating cantilevers beyond a few MHz using adjacent piezo shakers, the excitation method was switched to photothermal excitation¹.

Common CD/DVD players require lasers of two different wavelengths in order to conform with both the CD and DVD recording standards. Most commercial CD/DVD heads have two built-in semiconductor lasers, one with a wavelength around 785nm (CD) and the other with wavelength around 665nm (DVD). The CD/DVD Burner optics are composed of two different high power laser diode sources (max intensity >5mW) in which both beams are collimated with the same beam diameter and perfectly superimposed. In our setup, we use the 665nm laser to detect the

¹**Acknowledgments:** The results achieved in this section were gathered in cooperation with Dr. Dominik Ziegler, and Mr. Adrian Nievergelt of the Nanotechnology Group. Mr. Nievergelt was assigned to create a setup with which one could photothermally actuate cantilevers at frequencies significantly above a few MHz, in order to truly test the potential bandwidth of the novel readout. To simplify the task, my idea was to remove the light source from a CD/DVD player and mounted onto an optical tabletop system, which Mr. Nievergelt designed, prototyped and built following Dr. Ziegler’s and my guidelines. Dr. Ziegler’s idea to make a “scanning” setup using microsteppers was a valuable addition. Dr. Ziegler, Mr. Nievergelt and I spent much effort on the Labview programming and general debugging in creating such a system.

angle of cantilever deflection, while modulating the 785nm laser for simultaneous photothermal excitation. Such drives have been used in AFM optical setups in the past [Hwu06], however not in combination with photothermal excitation. We show that it is possible to excite higher eigenmodes of commercial cantilevers beyond the frequencies achievable with traditional acoustic excitation.

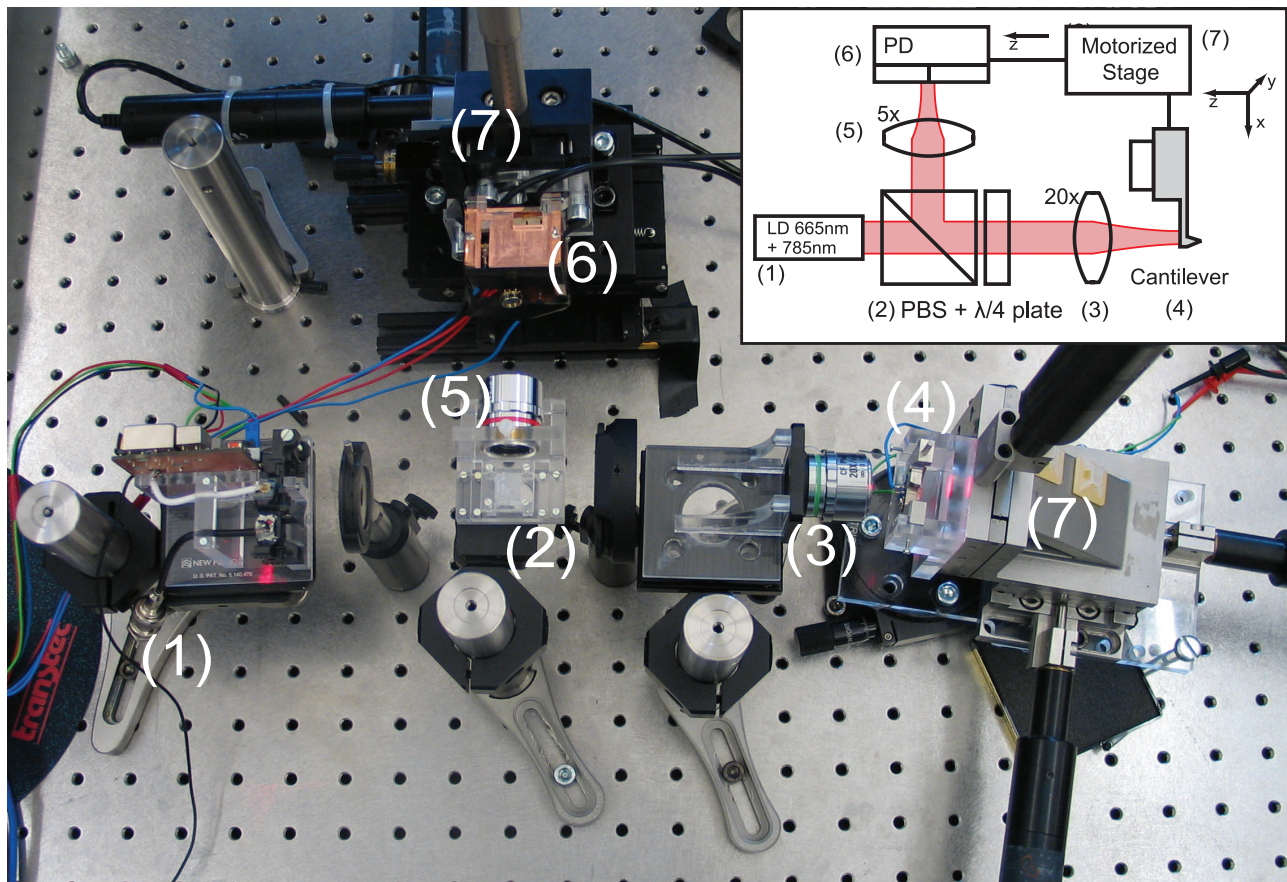


Figure 8.1: Illustration of focused beam reflection on a cantilever through a lens with focal length f . An incoming beam along the optical axis gets deflected on a surface inclined at angle α . The returning beam has an angle 2α relative to the incoming beam, which is returned through the lens at a offset Δx from the optical axis. Inset: Schematic of the optical tabletop setup which is equipped for photothermal excitation. A CD/DVD writer head (1) provides the collimated infrared and red laser beams necessary for photothermal operation and readout respectively; a polarizing beam splitter (2) with a $\frac{\lambda}{4}$ retarder plate, a $20\times$ microscopy lens (3), the cantilever holder (4) mounted on a three axis stage and actuated by linear actuators (7) in x , y , and z directions, a $5\times$ microscopy lens (5) contracts and focuses the beam towards a 665nm bandpass filter (6) and quadrant photodiode with a homebuilt deflection readout.

8.1 Experimental Setup

In conventional beam deflection setups the cantilever is not perfectly orthogonal to the incident laser beam, but offset by a few degrees [Meyer88]. Thus the incident laser is reflected at the same angle from the backside of the cantilever, and onto a bi-cell or quadrant photodiode. Such a configuration is not only sensitive to angles changes of the cantilever backside but to deflections of the cantilever as well; depending on the laser spot size and position this can cause pole-zero cancellations which lead to a significantly reduced sensitivity in the detection of higher mode vibrations [Stark04]. In order to prevent this, we build a setup for angle sensitive detection where the incident optical beam is perfectly orthogonal to the cantilever backside at rest. In such a setup, the reflected beam returns along the incident path, collected by the same lens used for focusing (See Figure 8.1)). Ideally, angle-less deflections result in an offset along the incident optical axis, which does not affect the signal received on the quadrant photodiode. The resulting deflection is solely a function of the cantilever angle α and is illustrated as Δx , where

$$\Delta x \approx f \tan(2\alpha).$$

The optical table-top setup built to characterize and measure cantilever thermal excitation is explained following the laser beams from source to detection. The laser source (1), was an optical head removed from a commercial CD/DVD RW drive (LG Super Multi DVD G24). Both diode laser sources inside this drive are prealigned, and thus perfectly superimposed and coherent at the output of the optical head, with a beam diameter of approximately 5 mm. Since the wavelengths are a priori unknown, we analyzed the wavelength of both lasers using a Michelson interferometer (WA-1500, Burleigh Instruments) and found that the IR laser was at 780 nm, and the red laser at 667 nm. We decided to use the 667 nm laser for the beam deflection, and the 780 nm laser for optical excitation. The excitation laser can be tuned to a modulation depth of more than 80 mW which is more than sufficient. The excitation laser diode is driven using the output generated by the lock-in amplifier, and is thus limited by the bandwidth of the lock-in (50 MHz). The output intensity of the readout laser is about 6 mW of unpolarized light. The readout laser is modulated around 300 MHz to prevent mode hopping noise, using the laser diode driver detailed in Section 7.3.

Both collimated laser beams are fed into a polarizing beam splitter with an antireflective coating (2) (NT47-777, Edmund Optics) which passes light of only one polarization direction while discarding the orthogonally polarized beam. Only light of the primary linear polarization is used to operate the rest of the setup. Additionally at (2), a $\frac{\lambda}{4}$ wave retarder with an anti-reflective coating (NT43-700, Edmund Optics) is utilized to achieve a quarter wavelength phase shift on the linearly polarized light. The beam enters a 20 \times microscopy objective (Nikon CF Plan EPI 20 \times , 0.35 NA) at (3), focusing the collimated beam onto the back of a cantilever (4), where the light

is reflected and returned to the same objective. The cantilever is mounted in a standard Multi-mode AFM holder with a built-in dither piezo at position (4). The cantilever holder is mounted on a micrometer stage (Newport M-462) with 3 degrees of freedom at an angle of 11° so that the incident beam is truly orthogonal to the surface.

The returning beam is again shifted in the $\frac{\lambda}{4}$ wave retarder, and then directed to a $5\times$ microscopy lens (Nikon CF Plan EPI 5x, 0.13 NA) by the beam splitter. The $5\times$ microscopy lens (5) will focus the beam onto a OD6 bandpass filter centered around 665nm with a bandwidth of 30nm (Z665/30x, Chroma) and quadrant photodiode SD 085-23-21-021 (Advanced Photonix) (6) to an acceptable size. Motorized linear steppers (Newport 850B) (7) are added to the micrometer stages to move the position of the focused spots relative to the cantilever and the quadrant photodiode (in X and Y dimensions).

A digital high-frequency 6-channel lock-in amplifier (Zurich Instruments HF2) is used to simultaneously excite and demodulate five channels. The lock-in amplifier generates the excitation signal as a superposition of sinusoidal waves whose frequencies match the cantilevers lateral eigenmodes. The high-pass filtered vertical deflection signal from a homebuilt photodiode readout, with a high bandwidth [Enning11] is fed into the lock-in amplifier's input. The lock-in will demodulate and record the amplitude and phase of all 6 channels (all 6 eigenmodes) simultaneously. The lock-in amplifier and all mechanical stages are fully steered using LabView.

8.2 Photothermal Excitation of Higher Eigenmodes

The spot size on the backside of the cantilever was measured using the razorblade technique on the lever edge. The sum signal was recorded as the cantilever was passed through the beam. Assuming a Gaussian beam profile, we found the smallest achievable spot size of $1.33 \mu\text{m}$, which is in good agreement with the theoretically predicted value of $1.1 \mu\text{m}$ for the objective and laser wavelength used. Since the excitation laser is superimposed on the readout laser, both wavelengths will be in focus in the same area on the backside of the cantilever.

Figure 8.2 compares the spectral responses of an acoustically and photothermally excited Olympus AC200 cantilever (with backside aluminum coating). The bandwidth of acoustic (piezo driven) excitation is clearly limited to ~ 3 MHz. The photothermal excitation on the other hand (see Figure 8.2) shows no limit in bandwidth; it can excite frequencies up to 20 MHz where the photodiode readout electronics begin to limit the system [Enning11]. The readout and excitation laser spot was positioned at the center of the cantilever, for both sweeps. From Figure 8.2 we can see the first seven lateral eigenfrequencies at 160.5 kHz, 955.5 kHz, 2.478 MHz, 4.564 MHz, 7.236 MHz, 10.420 MHz and 17.267 MHz. The peaks labeled with 't' are identified as torsional modes. Note that unless the readout laser is perfectly centered on the tilt axis, tor-

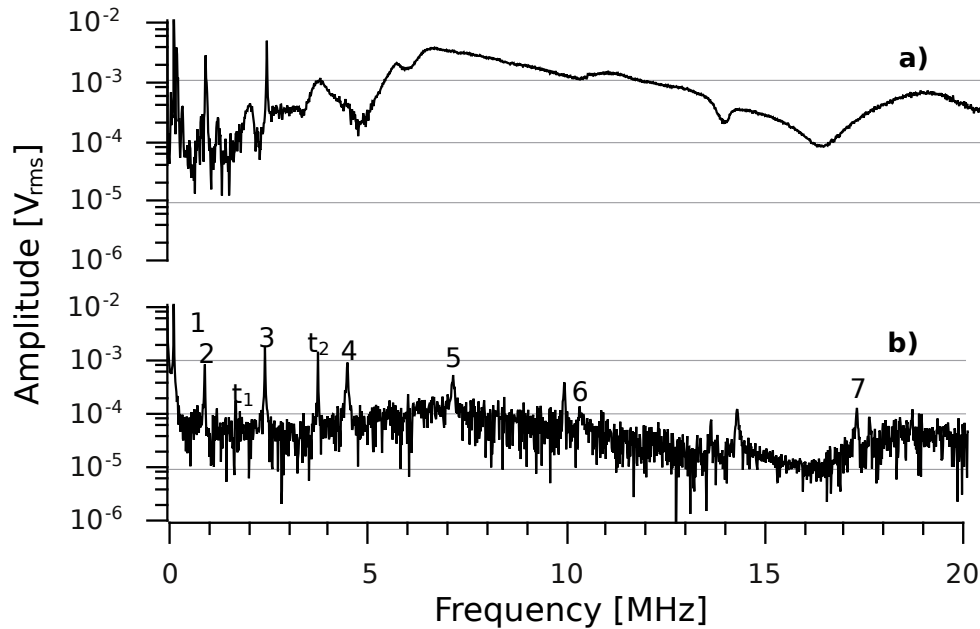


Figure 8.2: Comparison of amplitude frequency responses of a Olympus AC200 cantilever using a) piezo and b) photothermal excitation. The piezo bandwidth is clearly limited to about 3 MHz, while sharp peaks still are visible on the photothermally actuated spectrum. The red labels indicate the eigenmode of the longitudinal or torsional modes t .

sional modes may be detected in the vertical deflection, since there is a local inclination in the cantilever along its axis.

Through the use of linear motorized steppers, we were able to move the cantilever in x and y directions within the focal plane. This allowed us to position the readout and excitation lasers at any position on the backside of the cantilever. In combination with LabView we were able to scan over the entire surface of the cantilever, recording intensity, amplitude and phase of multiple eigenmodes at every position (pixel resolution 100nm). Column a in Figure 8.3 shows the amplitude (top) and phase (bottom) response obtained at different positions on the cantilever, for the first five eigenmodes, for the mechanical excitation. The fifth mode, at 7.24 MHz, can no longer be excited mechanically with a dither piezo. Column b in Figure 8.3 shows the same cantilever under photothermal excitation. The acoustic excitation scans show that for eigenmode n there are always $n - 1$ zeros where no amplitude can be detected. At these locations the beam effectively does not change its angle of deflection, resulting in no signal in the reflected laser beam. Similarly, the regions where the angle change is the highest are the regions where the highest amplitudes are recorded.

Interestingly, the thermal excitation scans show more zeros and maxima than the equivalent mechanical excitation scan. This is due to additional local zeros due to the thermal excitation efficiency. Heating a spot on the cantilever surface always induces a local thermal stress in the metal backside coating, resulting in a mechanical displacement, similar to that of a bi-metallic

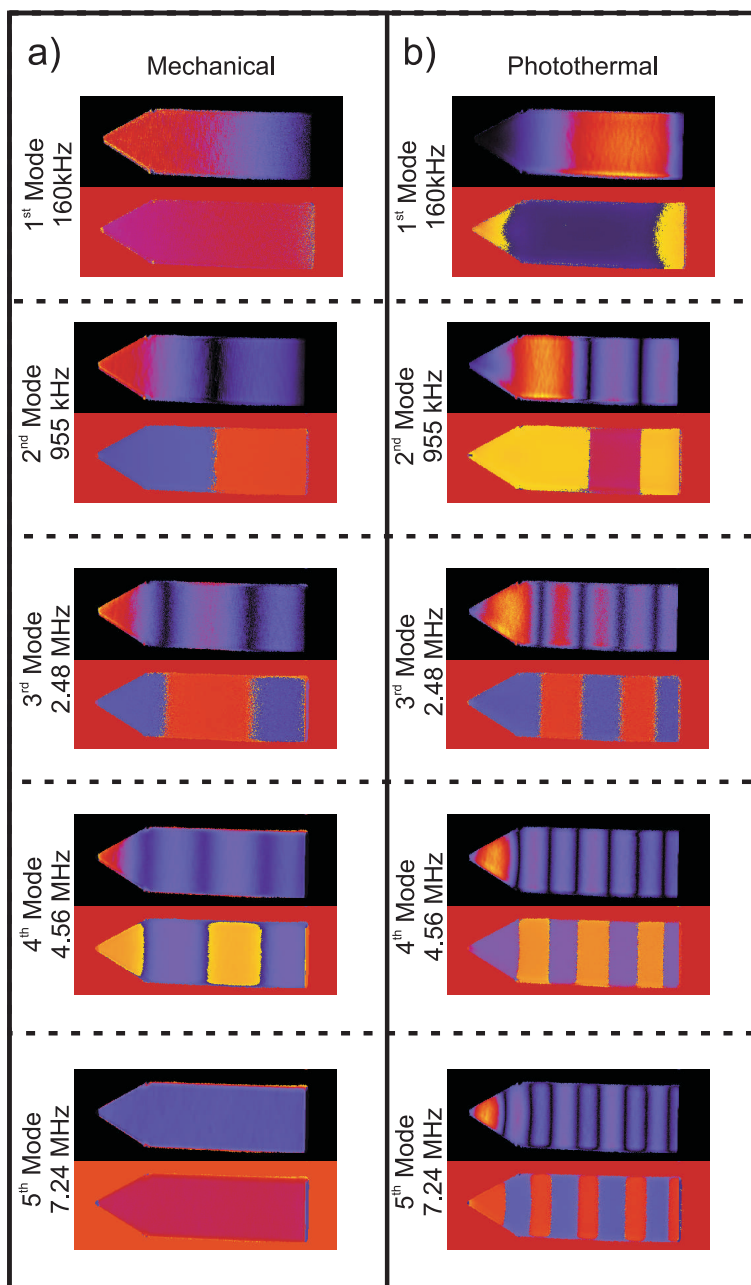


Figure 8.3: Comparison of the amplitude and phase information obtained at different locations on the cantilever. The first five eigenmodes are shown using mechanical (left) and photothermal (right) excitation.

strip. A cantilever oscillating at one of its eigenmodes will have regions where such deformations are inherent to the shape of the oscillation, which are regions that express a high amount of surface tension during oscillation. Equivalently there are regions where no deformation, and thus no surface tension, takes place. These regions are equivalent to the minima and maxima

(respectively) observed for photothermal excitation, and are offset in position from the beam deflection minima and maxima. This is consistent with the theory that photothermal excitation uses a thermal gradient in a bi-metal like surface to produce thermomechanical stress in the material [Wang07, Ramos06, Jeppesen09]. Since the excitation and readout lasers are superimposed and scan over the backside of the cantilever simultaneously, the amplitude and phase response recorded is a convolution of these two different effects, resulting in the additional signal maxima and zeroes.

Uncoated cantilevers responded to photothermal actuation significantly weaker, resulting in difficulty in identifying resonance peaks. This is consistent with the theory of a bimetallic strip like actuation mechanism. Typical backside coatings for silicon cantilevers include aluminum and gold coatings. At 25°C, gold has a thermal expansion of $14.2 \times 10^{-6} \text{ K}^{-1}$, and aluminum has a thermal expansion of $31 \times 10^{-6} \text{ K}^{-1}$, which are both higher than that of silicon, at $2.6 \times 10^{-6} \text{ K}^{-1}$ [Lide10].

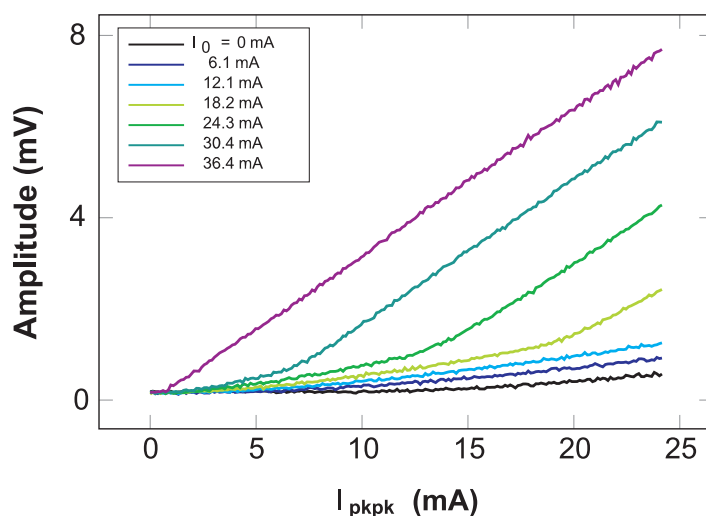


Figure 8.4: Amplitude response of the cantilever as a function of excitation laser modulation depth at different current offsets. As the offset is increased, the amplitude response to different modulation depths becomes more linear. The ideal response is when the offset is just above the diode laser threshold (in our case 36.4 mA), where the modulation depth will no longer drop below the threshold.

In addition to analyzing the ideal position for photothermal excitation, we also analyzed the cantilever's fundamental eigenmode amplitude response as a function of photothermal modulation depth. To do this we swept the excitation signal at a number of different current offsets and recorded the amplitude response. The spot was positioned a few micrometers from the base of the cantilever, in the region of highest amplitude response for the fundamental eigenmode (see Figure 8.3b). The results of these sweeps are shown in Figure 8.4. If the modulation remains below the threshold of the excitation laser, the system will have a non-linear relation between

excitation and the resulting amplitude. As the DC current offset pushes the modulation over the laser threshold (36.4 mA), the response becomes very linear. We find that the ideal point for laser excitation is when the offset is just above threshold, which will hinder the modulation from dropping below threshold into the non-linear region. A linear excitation to amplitude response is desirable and expected by most amplitude and automatic gain controllers. In addition, a linear response will reduce the degree of unwanted harmonics in the excitation signal.

8.3 Conclusion

We have show that a CD/DVD head can be used as an affordable light source suitable for simultaneous excitation and readout of AFM microcantilevers. Using photothermal excitation we could excite eigenmodes up to 21 MHz, up to the bandwidth of our photodiode readout. Scanning the laser beam over the cantilever helps to understanding the cantilever dynamics, provides the position where the highest readout sensitivity and excitation efficiency can be achieved, and can be useful to reveal contaminated or damaged cantilevers.

Chapter 9

Appendix C: Analysis of 2-D Polymer Surfaces

9.1 Thin Film Characterization and Visualization

The atomic force microscope is an excellent tool for imaging and analyzing the structure and size of polymer films. Accurate detection of polymer film thickness and conformation is an important aspect of materials science and chemistry [Kumaki96]. Through AFM, the polymer film can be imaged to resolve individual regions or units of polymers and co-polymers [Kumaki98, Akhremitchev98], and can be used to invasively to "scratch" and characterize film thicknesses [Ton-That00, Anariba03, Kissel10], also termed as nanoshaving [Xu97]¹.

Our efforts were to characterize the assembly and stability of a potentially free standing monolayer sheet from the air/water interface from a shape-persistent, hexafunctional terpyridine (tpy)-based D_{6h} -symmetric monomer. The steps involved in the synthesis of the monomer can be seen in Figure 9.1, based on the procedure given in [Bauer10]. This monomer can be transferred from the air/water interface to atomically flat mica surfaces for further analysis through AFM, using the Langmuir Blodgett technique. Ideally these monomers have a diameter of approximately 3.0 nm, and a height of 0.9 nm. In the topography image of Figure 9.2, a surface coated with synthesized monomers with small bead like structures of approximately 5 nm in diameter can be seen. The apparently larger size of the monomers in the image can be attributed to the convolution of the tip-radius with the topography, a common artifact when imaging samples in similar size range as the tip itself.

¹**Acknowledgments:** The results achieved in this section were gathered in cooperation with Mr. Thomas Bauer and Prof. Dieter Schlueter's Polymer Chemistry Group (ETH Zuerich). Our novel microscope significantly aided Thomas Bauer's work on analyzing and testing the creation of a flat, single layered 2-dimensional polymer film, samples of which he prepared and provided to us.

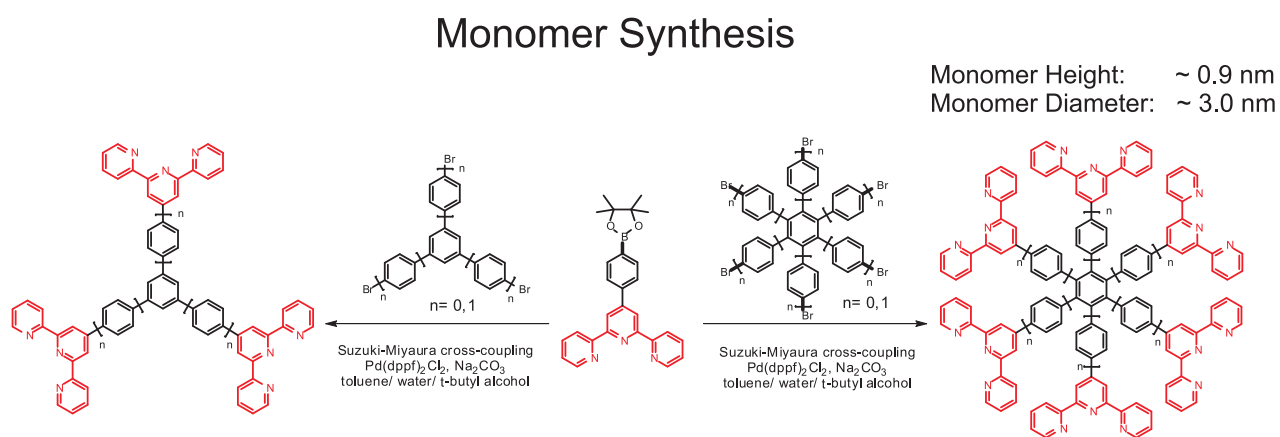


Figure 9.1: Synthesis of D_{3h} and D_{6h} symmetric monomers via Suzuki-Miyaura cross coupling [Bauer10].

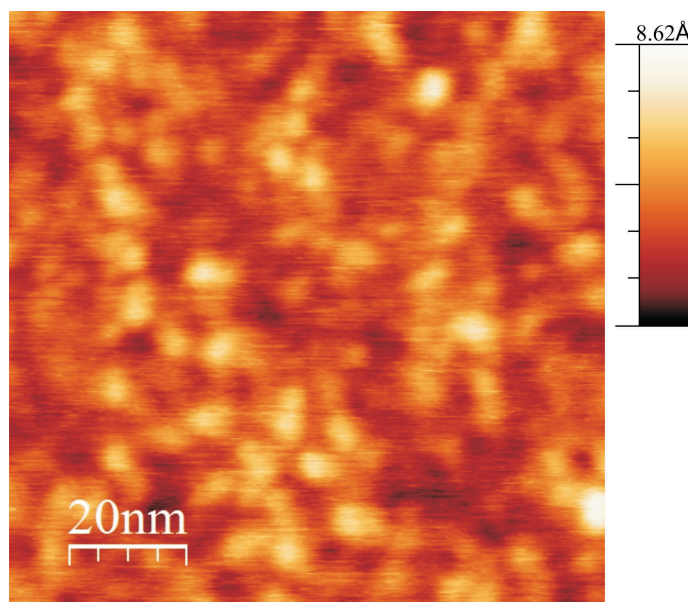


Figure 9.2: High resolution topography image of the monomer on a mica substrate in air. Spherical structures $<5\text{nm}$ in diameter are seen resting on the surface in no apparent order. This image was obtained via light AM mode on an Asylum Research Cypher microscope using an Olympus AC200 cantilever oscillating at the first eigenmode (160.6kHz). Deviations in the measured monomer diameter are due to cantilever tip artifacts.

The thickness of these monomer films can be estimated after an invasive "nanoshaving" experiment. The mica substrate underneath the monomer layer was freshly cleaved before application of the monomer. Through careful control of the loading force of the cantilever, it is possible to scratch away the monomer without damaging the underlying substrate. The scratching experi-

ment was performed by switching into constant force mode (contact mode) and applying a constant loading force while scanning the surface. Afterward the surface is re-imaged to evaluate the invasive removal of the monomer.

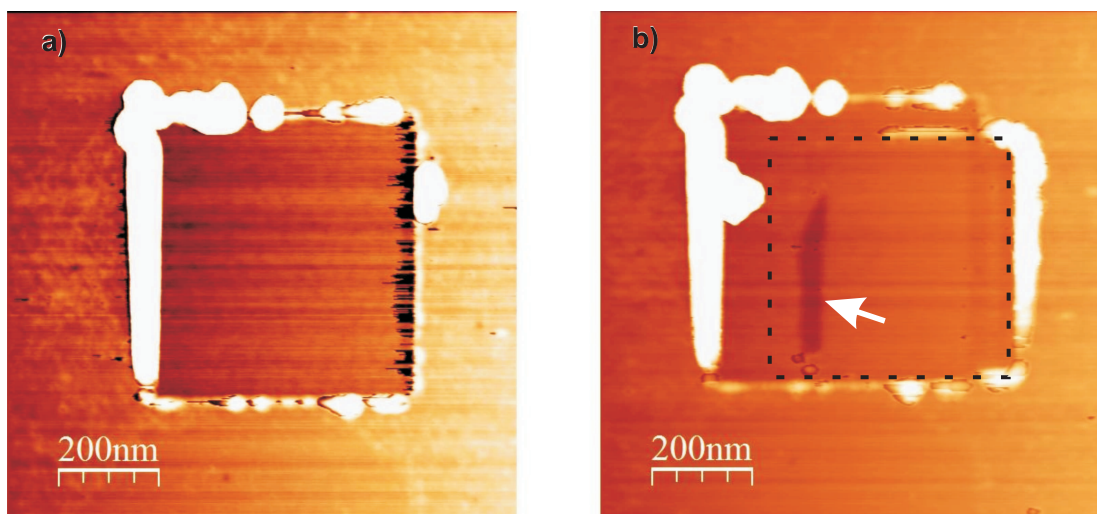


Figure 9.3: These images were created using an Asylum Research MFP3D microscope and an Olympus AC 240 cantilever in AM mode ($f_0 = 74.9\text{kHz}$, $A_0 = 60\text{nm}$, $Asp = 38\text{nm}$, scan size = $1 \times 1 \mu\text{m}^2$, scan speed = 2 lines / sec). The surface was scratched with the same cantilever used to image by switching into constant force mode and applying a constant force while scanning. The applied load of 28 nN for the first shave is lower than needed to wear the underlying mica substrate, and can be seen in a). A second shaving scan is performed using the same force in order to guarantee the revealed substrate is truly mica, and a third shave with higher load of 71 nN is performed (dotted box in b), causing the first signs of wear on the hard mica surface, indicated by the white arrow. All constant force mode shaving scans consisted of a $600 \times 600 \text{nm}^2$ square, with a scan speed = 5 lines/sec.

After the scratching experiment, the cantilever resonance frequency was checked to confirm the tip stayed intact and no residues adsorbed on it. Cantilever spring constants were determined using the inverse thermal method. The scratching of Figure 9.3 was performed with a constant force of $\approx 28 \text{ nN}$. A second scratch with identical parameters was performed over the same area in order to guarantee complete removal of the monomer film. The load of 28 nN is lower than needed to wear the underlying mica substrate. A third scratch with higher load of 71 nN is performed, causing the first signs of wear on the hard mica surface [Hu95a].

Figure 9.4a shows a monomer surface where a region has been scratched away using nanoshaving, exposing the underlying mica surface. Scan parameters were equivalent to those in Figure 9.3. Figure 9.4b shows the profile of the line in a), revealing a height of approximately 0.8 - 1.0 nm, conforming very nicely with the theoretical value. These results suggest that it is possible to apply a single molecular layer of D_{6h} -symmetric monomers onto a mica substrate, and that the film on the air/water interface is truly one molecular layer thick.

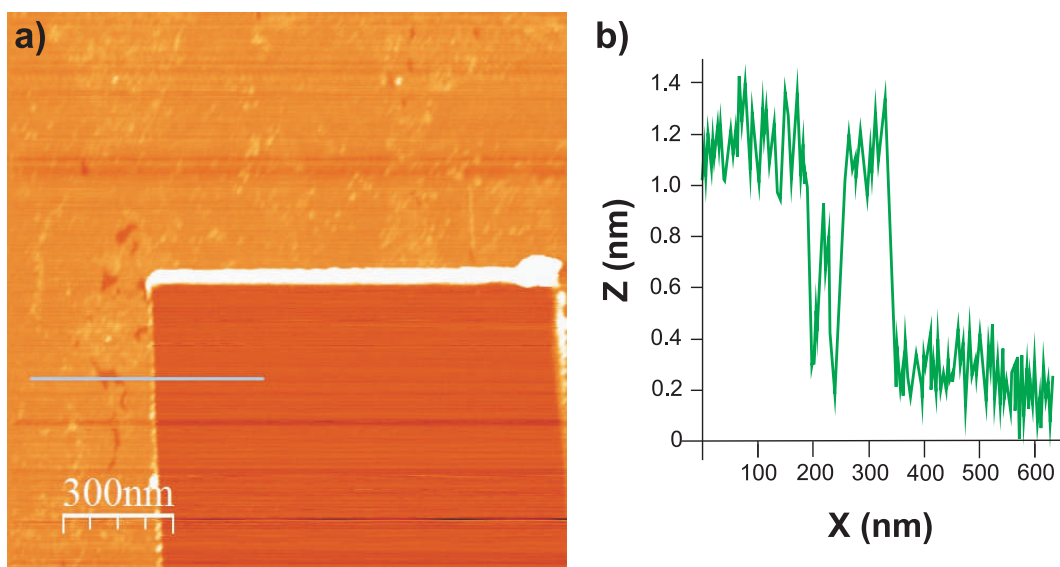


Figure 9.4: a) A region of monomer has been removed using the nanoshaving technique, exposing the mica surface below. The profile of the line in a) is shown in b), where a height of approximately 0.8 - 1.0 nm can be seen. Scan parameters were equivalent to those in Figure 9.3.

Polymer Synthesis

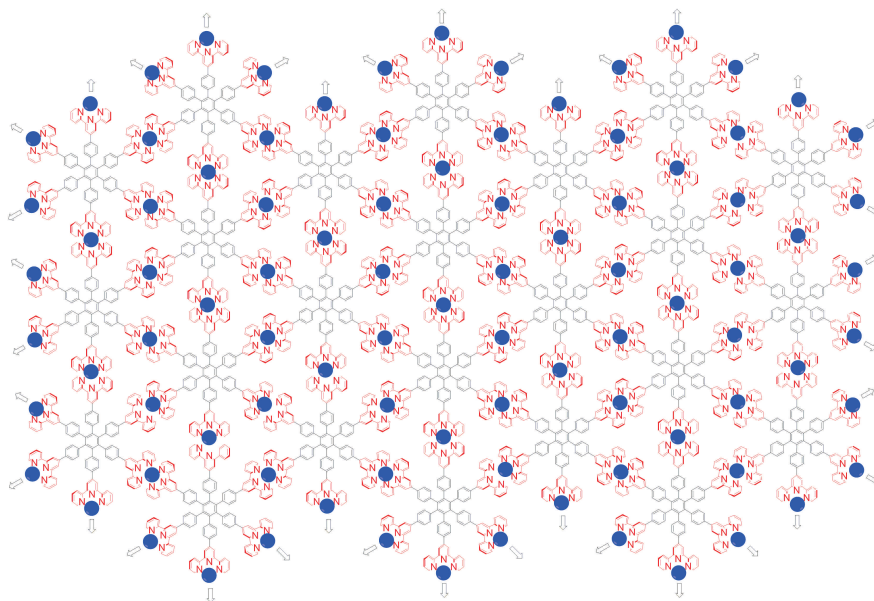


Figure 9.5: Schematic of the ideal resulting polymeric surface. The tpy units (red) of contiguous monomers will connect, consuming the metal ion (blue spheres) in the process. Ideally, a flat, 2-dimensional surface will be formed. Counter anions are omitted.

Polymerization of the monomer is achieved by exposing the monomer with metal salts in the water subphase before transfer. Metal ions such as Zn^{2+} , Co^{2+} , Ni^{2+} , Fe^{2+} , or Ru^{2+} will diffuse to the monomers at the air/water interface, where the metal ion is consumed in a complexation reaction between 2 individual tpy units. Ideally all 6 tpy units of a particular monomer will merge with a unit from another monomer, forming a contiguous, 2-dimensional polymeric surface, a schematic of which is shown in Figure 9.5. This polymeric surface is then transferred to the mica substrate, washed with ultra-pure water, and imaged, where an attempt to image the molecular periodicity of the transferred polymer is made.

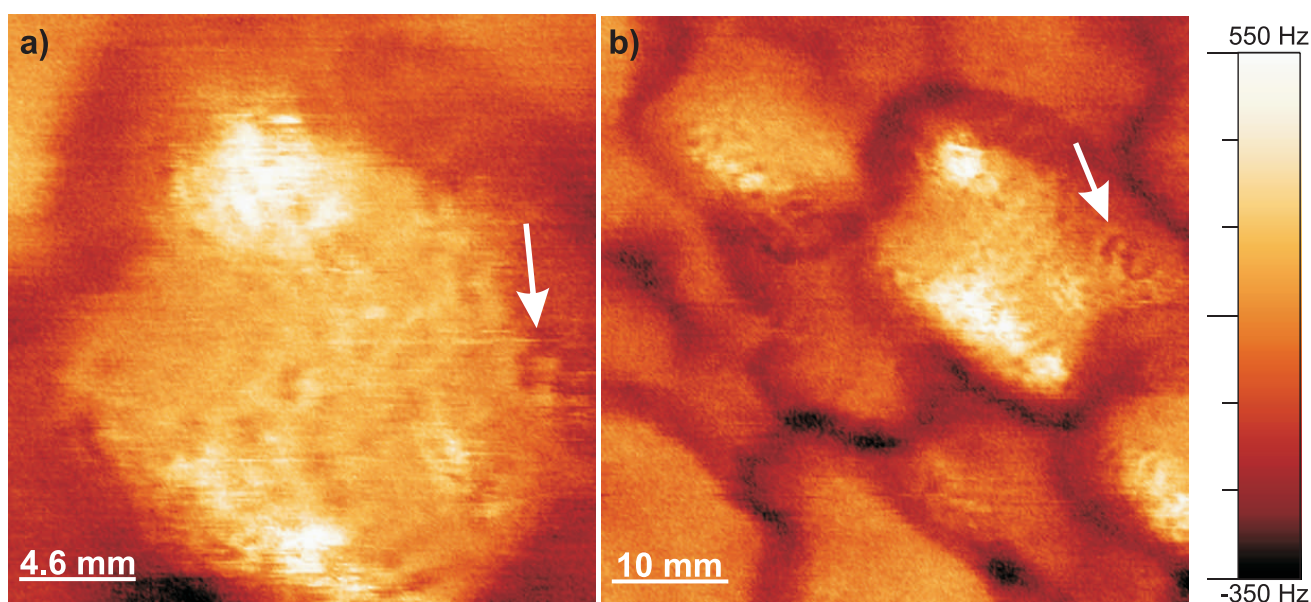


Figure 9.6: Frequency Shift signal of the second eigenmode of the D_{6h} -symmetric polymer in air. The fundamental eigenmode was used in FM to control for topography, while the second eigenmode was used to acquire a high resolution frequency shift signal. Cantilever used was an Olympus AC200. a) Image scan size = $23 \times 23 \text{ nm}^2$, scan speed = 130 nm/s, $f_0 = 180.3 \text{ kHz}$, $\Delta f = -315 \text{ Hz}$, $A_0 = 12.85 \text{ nm}$, $f_1 = 1.04 \text{ MHz}$, $A_1 = 0.51 \text{ nm}$. b) Image scan size = $50 \times 50 \text{ nm}^2$, scan speed = 250 nm/s, $f_0 = 180.3 \text{ kHz}$, $\Delta f = -315 \text{ Hz}$, $A_0 = 2.85 \text{ nm}$, $f_1 = 1.04 \text{ MHz}$, $A_1 = 0.51 \text{ nm}$. The white arrow points to a repeating structure that can clearly be seen in both images.

The polymeric surface was scanned in the novel microscope using an Olympus AC200 oscillating at two cantilever eigenmodes simultaneously; the fundamental oscillating at 180.3 kHz with an amplitude of 12.85 nm, and the second eigenmode oscillating at 1.04 MHz with an amplitude of 0.51 nm. The first eigenmode was used to control the tip-sample separation, by using attractive FM with a setpoint of -315 Hz. The higher eigenmode permitted the use of a very small oscillation amplitude without the danger of quenching the oscillation by jump-to-contact. See Chapter 5 for more information on effective cantilever stiffening due to higher eigenmodes.

The image of the polymeric surface is seen in Figure 9.6a and b. The polymeric surface forms

repeating plate-like structures, each of approximately 20 - 30 nm in diameter, which can be clearly seen in b). Surface structures approximately 1 nm in resolution can be seen, however without any recognizable order. The white arrows point to a region of high contrast, which can clearly be seen in both separate scans a) and b), confirming that the contrast is originating from the surface, and not a random artifact. The thickness of the polymer film could not be confirmed, as nanoshaving experiments on this surface always resulted in the destruction of the tip and irreproducible changes to the sample.

9.2 Conclusion

Although the AFM scans did reveal that the polymeric surface does not yet form a continuous, truly two dimensional structure, the results obtained here were mostly favorable from the instrument point of view. The high resolution images of the monomeric units do suggest that the monomers fit their theoretical lateral size. Similarly, the nanoshaving tests suggest that the monomer height fits the theoretically established values, and suggest that a true monolayer of monomers can be formed along the air/water interface. The scans of the polymeric images confirm that a structural change is taking place during polymerization, and that the microscope is capable of measuring the surface with a very high resolution.

Bibliography

- [Abe07] M. Abe, Y. Sugimoto, T. Namikawa, K. Morita, N. Oyabu, and S. Morita. Drift-compensated data acquisition performed at room temperature with frequency modulation atomic force microscopy. *Applied Physics Letters*, 90(20):203103, **2007**.
- [Abrahamson63] A. A. Abrahamson. Repulsive interaction potentials between rare-gas atoms. homonuclear two-center systems. *Phys. Rev.*, 130(2):693, **1963**.
- [Akhremitchev98] B. B. Akhremitchev, B. K. Mohny, K. G. Marra, T. M. Chapman, and G. C. Walker. Atomic force microscopy studies of hydration of fluorinated amide/urethane copolymer film surfaces. *Langmuir*, 14(15):3976, **1998**.
- [Albrecht87] T. R. Albrecht and C. F. Quate. Atomic resolution imaging of a nonconductor by atomic force microscopy. *Journal of Applied Physics*, 62(7):2599, **1987**.
- [Albrecht91] T. R. Albrecht, P. Grutter, D. Horne, and D. Rugar. Frequency modulation detection using high-q cantilevers for enhanced force microscope sensitivity. *Journal of Applied Physics*, 69(2):668, **1991**.
- [Alexander89] S. Alexander, L. Helleman, O. Marti, J. Schneir, V. Elings, P. K. Hansma, M. Longmire, and J. Gurley. An atomic-resolution atomic-force microscope implemented using an optical lever. *Journal of Applied Physics*, 65(1):164, **1989**.
- [Alphonse02] G. A. Alphonse. Design of high-power superluminescent diodes with low spectral modulation. volume 4648, 125–138. SPIE, **2002**.
- [Amer86] N. M. Amer, A. Skumanich, and D. Ripple. Photothermal modulation of the gap distance in scanning tunneling microscopy. *Applied Physics Letters*, 49(3):137, **1986**.

- [Anariba03] F. Anariba, S. H. DuVall, and R. L. McCreery. Mono- and multilayer formation by diazonium reduction on carbon surfaces monitored with atomic force microscopy scratching. *Analytical Chemistry*, 75(15):3837, **2003**. PMID: 14572051.
- [Ando01] T. Ando, N. Kodera, E. Takai, D. Maruyama, K. Saito, and A. Toda. A high-speed atomic force microscope for studying biological macromolecules. *Proceedings of the National Academy of Sciences*, 98(22):12468, **2001**.
- [Arimoto86] A. Arimoto, M. Ojima, N. Chinone, A. Oishi, T. Gotoh, and N. Ohnuki. Optimum conditions for the high frequency noise reduction method in optical videodisc players. *Appl. Opt.*, 25(9):1398, **1986**.
- [Bader00] R. F. W. Bader. Atomic force microscope as an open system and the ehrenfest force. *Phys. Rev. B*, 61(11):7795, **2000**.
- [Bader06] R. F. W. Bader. Pauli repulsions exist only in the eye of the beholder. *Chemistry - A European Journal*, 12:2896, **2006**.
- [Bar97] G. Bar, Y. Thomann, R. Brandsch, H.-J. Cantow, and M.-H. Whangbo. Factors affecting the height and phase images in tapping mode atomic force microscopy. study of phase-separated polymer blends of poly(ethene-co-styrene) and poly(2,6-dimethyl-1,4-phenylene oxide). *Langmuir*, 13(14):3807, **1997**.
- [Baralia06] G. G. Baralia, A. Pallandre, B. Nysten, and A. M. Jonas. Nanopatterned self-assembled monolayers. *Nanotechnology*, 17(4):1160, **2006**.
- [Basak06] S. Basak, A. Raman, and S. V. Garimella. Hydrodynamic loading of microcantilevers vibrating in viscous fluids. *Journal of Applied Physics*, 99(11):114906, **2006**.
- [Bauer10] T. Bauer, A. D. Schlüter, and J. Sakamoto. Towards 2d and 3d coordination polymers: Synthesis of shape-persistent star monomers with 2,2':6,2'-terpyridin-4-yl units at the periphery. *Thieme eJournals*, 6:877, **2010**.
- [Belikov06] S. Belikov and S. Magonov. True molecular-scale imaging in atomic force microscopy: Experiment and modeling. *Japanese Journal of Applied Physics*, 45(3B):2158, **2006**.
- [Bhiladvala04] R. B. Bhiladvala and Z. J. Wang. Effect of fluids on the q factor and resonance frequency of oscillating micrometer and nanometer scale beams. *Phys. Rev. E*, 69(3):036307, **2004**.

- [Bhushan95] B. Bhushan, J. Israelachvili, and U. Landman. Nanotribology: friction, wear and lubrication at the atomic scale. *Nature*, 374:607, **1995**.
- [Bhushan07] B. Bhushan (Editor). *Springer Handbook of Nano-technology*. Springer Berlin / Heidelberg / New York, **2007**.
- [Bilotti75] A. Bilotti and E. Mariani. Noise characteristics of current mirror sinks/sources. *Journal of Solid-State Circuits, IEEE*, 10:516 , **1975**.
- [Binggeli94] M. Binggeli and C. M. Mate. Influence of capillary condensation of water on nanotribology studied by force microscopy. *Applied Physics Letters*, 65(4):415, **1994**.
- [Binnig82] G. Binnig, H. Rohrer, C. Gerber, and E. Weibel. Surface studies by scanning tunneling microscopy. *Phys. Rev. Lett.*, 49(1):57, **1982**.
- [Binnig83] G. Binnig, H. Rohrer, C. Gerber, and E. Weibel. 7 x 7 reconstruction on si(111) resolved in real space. *Phys. Rev. Lett.*, 50(2):120, **1983**.
- [Binnig86] G. Binnig, C. F. Quate, and C. Gerber. Atomic force microscope. *Phys. Rev. Lett.*, 56(9):930, **1986**.
- [Binnig99] G. Binnig and H. Rohrer. In touch with atoms. *Rev. Mod. Phys.*, 71(2):S324, **1999**.
- [Boccaro80] A. C. Boccaro, D. Fournier, W. Jackson, and N. M. Amer. Sensitive photothermal deflection technique for measuring absorption in optically thin media. *Opt. Lett.*, 5(9):377, **1980**.
- [Bradley90] C. C. Bradley, J. Chen, and R. G. Hulet. Instrumentation for the stable operation of laser diodes. *Review of Scientific Instruments*, 61(8):2097, **1990**.
- [Braun10] O. Braun. Bridging the gap between the atomic-scale and macroscopic modeling of friction. *Tribology Letters*, 39:283, **2010**. ISSN 1023-8883. 10.1007/s11249-010-9648-7.
- [Buckingham38] R. A. Buckingham. The classical equation of state of gaseous helium, neon and argon. *Proceedings of the Royal Society of London. Series A, Mathematical and Physical Sciences*, 168:264, **1938**.
- [Budakian02] R. Budakian and S. J. Putterman. Force detection using a fiber-optic cantilever. *Applied Physics Letters*, 81(11):2100, **2002**.

- [Butt91] H.-J. Butt. Measuring electrostatic, van der waals, and hydration forces in electrolyte solutions with an atomic force microscope. *Biophysical Journal*, 60(6):1438 , **1991**. ISSN 0006-3495.
- [Butt95] H.-J. Butt and M. Jaschke. Calculation of thermal noise in atomic force microscopy. *Nanotechnology*, 6:1, **1995**.
- [Butt05] H.-J. Butt, B. Cappella, and M. Kappl. Force measurements with the atomic force microscope: Technique, interpretation and applications. *Surface Science Reports*, 59(1-6):1 , **2005**. ISSN 0167-5729.
- [Butt08] H.-J. Butt. Capillary forces: Influence of roughness and heterogeneity. *Langmuir*, 24(9):4715, **2008**. PMID: 18442225.
- [Carpick99] R. W. Carpick, D. F. Ogletree, and M. Salmeron. A general equation for fitting contact area and friction vs load measurements. *Journal of Colloid and Interface Science*, 211(2):395 , **1999**. ISSN 0021-9797.
- [Chen90] C. J. Chen. Origin of atomic resolution on metal surfaces in scanning tunneling microscopy. *Phys. Rev. Lett.*, 65(4):448, **1990**.
- [Cleveland93] J. P. Cleveland, S. Manne, D. Bocek, and P. K. Hansma. A nondestructive method for determining the spring constant of cantilevers for scanning force microscopy. *Review of Scientific Instruments*, 64(2):403, **1993**.
- [Cleveland98] J. P. Cleveland, B. Anczykowski, A. E. Schmid, and V. B. Elings. Energy dissipation in tapping-mode atomic force microscopy. *Applied Physics Letters*, 72(20):2613, **1998**.
- [Colchero01] J. Colchero, A. Gil, and A. M. Baró. Resolution enhancement and improved data interpretation in electrostatic force microscopy. *Phys. Rev. B*, 64(24):245403, **2001**.
- [Derjaguin75] B. V. Derjaguin, V. M. Muller, and Y. P. Toporov. Effect of contact deformations on the adhesion of particles. *Journal of Colloid and Interface Science*, 53(2):314 , **1975**. ISSN 0021-9797.
- [Dicke46a] R. H. Dicke. The measurement of thermal radiation at microwave frequencies. *Review of Scientific Instruments*, 17(7):268, **1946**.
- [Dicke46b] R. H. Dicke, R. Beringer, R. L. Kyhl, and A. B. Vane. Atmospheric absorption measurements with a microwave radiometer. *Phys. Rev.*, 70(5-6):340, **1946**.

- [Duerig86] U. Duerig, J. K. Gimzewski, and D. W. Pohl. Experimental observation of forces acting during scanning tunneling microscopy. *Phys. Rev. Lett.*, 57(19):2403, **1986**.
- [Duerig97] U. Duerig, H. R. Steinauer, and N. Blanc. Dynamic force microscopy by means of the phase-controlled oscillator method. *Journal of Applied Physics*, 82(8):3641, **1997**.
- [Duerig99a] U. Duerig. Conservative and dissipative interactions in dynamic force microscopy. *Surface and Interface Analysis*, 27(5-6):467, **1999**. ISSN 1096-9918.
- [Duerig99b] U. Duerig. Relations between interaction force and frequency shift in large-amplitude dynamic force microscopy. *Applied Physics Letters*, 75(3):433, **1999**.
- [Eguchi02] T. Eguchi and Y. Hasegawa. High resolution atomic force microscopic imaging of the *si*(111) – (7 × 7) surface: Contribution of short-range force to the images. *Phys. Rev. Lett.*, 89(26):266105, **2002**.
- [Elmer97] F.-J. Elmer and M. Dreier. Eigenfrequencies of a rectangular atomic force microscope cantilever in a medium. *Journal of Applied Physics*, 81(12):7709, **1997**.
- [Enning11] R. Enning, D. Ziegler, A. Nievergelt, R. Friedlos, K. Venkataramani, and A. Stemmer. A high frequency sensor for optical beam deflection atomic force microscopy. *Review of Scientific Instruments*, 82(4):043705, **2011**.
- [Fabre96] A. Fabre, O. Saaid, F. Wiest, and C. Boucheron. High frequency applications based on a new current controlled conveyor. *Circuits and Systems I: Fundamental Theory and Applications, IEEE Transactions on*, 43(2):82, **1996**. ISSN 1057-7122.
- [Fan Fei09] L. Fan Fei. Translinear circuits tackle rf signals. *Microwaves & RF*, 48:100, **2009**.
- [Frenken10] J. Frenken and T. Oosterkamp. When mica and water meet. *Nature*, 464:38, **2010**.
- [Friis44] H. Friis. Noise figures of radio receivers. *Proceedings of the IRE*, 32(7):419, **1944**. ISSN 0096-8390.

- [Fukuma04] T. Fukuma, K. Kimura, K. Kobayashi, K. Matsushige, and H. Yamada. Dynamic force microscopy at high cantilever resonance frequencies using heterodyne optical beam deflection method. *Applied Physics Letters*, 85(25):6287, **2004**.
- [Fukuma05a] T. Fukuma, T. Ichii, K. Kobayashi, H. Yamada, and K. Matsushige. True-molecular resolution imaging by frequency modulation atomic force microscopy in various environments. *Applied Physics Letters*, 86(3):034103, **2005**.
- [Fukuma05b] T. Fukuma, K. Kimura, K. Kobayashi, K. Matsushige, and H. Yamada. Development of a low noise cantilever deflection sensor for multienvironment frequency-modulation atomic force microscopy. *Review of Scientific Instruments*, 76(12):053704, **2005**.
- [Fukuma05c] T. Fukuma, K. Kimura, K. Kobayashi, K. Matsushige, and H. Yamada. Frequency-modulation atomic force microscopy at high cantilever resonance frequencies using the heterodyne optical beam deflection method. *Review of Scientific Instruments*, 76(12), **2005**.
- [Fukuma05d] T. Fukuma, K. Kobayashi, K. Matsushige, and H. Yamada. True atomic resolution in liquid by frequency-modulation atomic force microscopy. *Applied Physics Letters*, 87(3):034101, **2005**.
- [Fukuma06] T. Fukuma and S. P. Jarvis. Development of a liquid-environment frequency modulation atomic force microscope with low noise deflection sensor for cantilevers of various dimensions. *Review of Scientific Instruments*, 77:043701, **2006**.
- [Fukuma09] T. Fukuma. Wideband low-noise optical beam deflection sensor with photothermal excitation for liquid-environment atomic force microscopy. *Review of Scientific Instruments*, 80(2):023707, **2009**.
- [Gan09] Y. Gan. Atomic and subnanometer resolution in ambient conditions by atomic force microscopy. *Surface Science Reports*, 64:99, **2009**.
- [Gao97] C. Gao. Theory of menisci and its applications. *Applied Physics Letters*, 71(13):1801, **1997**.
- [Garcia99] R. Garcia and A. San Paulo. Attractive and repulsive tip-sample interaction regimes in tapping-mode atomic force microscopy. *Phys. Rev. B*, 60(7):4961, **1999**.

- [Garcia00] R. Garcia and A. San Paulo. Dynamics of a vibrating tip near or in intermittent contact with a surface. *Phys. Rev. B*, 61(20):R13381, **2000**.
- [Ge07] G. Ge, D. Han, D. Lin, W. Chu, Y. Sun, L. Jiang, W. Ma, and C. Wang. Mac mode atomic force microscopy studies of living samples, ranging from cells to fresh tissue. *Ultramicroscopy*, 107(4-5):299, **2007**. ISSN 0304-3991.
- [Geisse09] N. A. Geisse. Afm and combined optical techniques. *Materials Today*, 12(7-8):40, **2009**. ISSN 1369-7021.
- [Giessibl95] F. J. Giessibl. Atomic resolution of the silicon (111)-(7x7) surface by atomic force microscopy. *Science*, 267:68, **1995**.
- [Giessibl97] F. J. Giessibl. Forces and frequency shifts in atomic-resolution dynamic-force microscopy. *Phys. Rev. B*, 56(24):16010, **1997**.
- [Giessibl99] F. J. Giessibl, H. Bielefeldt, S. Hembacher, and J. Mannhart. Calculation of the optimal imaging parameters for frequency modulation atomic force microscopy. *Applied Surface Science*, 140(3-4):352, **1999**. ISSN 0169-4332.
- [Giessibl00] F. J. Giessibl. Atomic resolution on si(111)-(7x7) by noncontact atomic force microscopy with a force sensor based on a quartz tuning fork. *Appl. Phys. Lett.*, 76:1470, **2000**.
- [Giessibl01] F. Giessibl, H. Bielefeldt, S. Hembacher, and J. Mannhart. Imaging of atomic orbitals with the atomic force microscope - experiments and simulations. *Annalen der Physik*, 10(11-12):887, **2001**. ISSN 1521-3889.
- [Gilbert75] B. Gilbert. Translinear circuits: a proposed classification. *Electronics Letters*, 11:14, **1975**.
- [Gilbert84] B. Gilbert. A monolithic 16-channels analog array normalizer. *IEEE Journal of Solid-State Circuits*, 19(6):956, **1984**.
- [Gilbert96] B. Gilbert. Translinear circuits: An historical overview. *Analog Integrated Circuits and Signal Processing*, 9:95, **1996**. ISSN 0925-1030. 10.1007/BF00166408.
- [Gnecco00] E. Gnecco, R. Bennewitz, T. Gyalog, C. Loppacher, M. Bammerlin, E. Meyer, and H.-J. Güntherodt. Velocity dependence of atomic friction. *Phys. Rev. Lett.*, 84(6):1172, **2000**.

- [Goldwasser11] S. M. Goldwasser. Diode lasers. <http://www.repairfaq.org/sam/laserdio.htm>, **2011**.
- [Goodman91] F. O. Goodman and N. Garcia. Roles of the attractive and repulsive forces in atomic-force microscopy. *Phys. Rev. B*, 43(6):4728, **1991**.
- [Gotsmann99] B. Gotsmann, C. Seidel, B. Anczykowski, and H. Fuchs. Conservative and dissipative tip-sample interaction forces probed with dynamic afm. *Phys. Rev. B*, 60(15):11051, **1999**.
- [Gotsmann01] B. Gotsmann and H. Fuchs. Dynamic force spectroscopy of conservative and dissipative forces in an al-au(111) tip-sample system. *Phys. Rev. Lett.*, 86(12):2597, **2001**.
- [Graeme96] J. Graeme. *Photodiode Amplifiers: Op Amp Solutions*. McGraw-Hill, **1996**.
- [Grober00] R. Grober, J. Acimovic, J. Schuck, D. Hessman, P. Kindlemann, J. Hespanha, S. Morse, K. Karrai, I. Tiemann, and S. Manus. Fundamental limits to force detection using quartz tuning forks. *Review of Scientific Instruments*, 71:2776, **2000**.
- [Han96] W. Han, S. M. Lindsay, and T. Jing. A magnetically driven oscillating probe microscope for operation in liquids. *Applied Physics Letters*, 69(26):4111, **1996**.
- [Hansma88] P. Hansma, V. Elings, O. Marti, and C. Bracker. Scanning tunneling microscopy and atomic force microscopy: application to biology and technology. *Science*, 242(4876):209, **1988**.
- [Hao91] H. W. Hao, A. M. Baro, and J. J. Saenz. Electrostatic and contact forces in force microscopy. *Journal of Vacuum Science & Technology B*, 9(2):1323, **1991**.
- [Hertz82] H. Hertz. Ueber die beruehrung fester elastischer koerper. *Journal für die reine und angewandte Mathematik*, 92:156, **1882**.
- [Heuberger96] M. Heuberger, G. Dietler, and L. Schlapbach. Elastic deformations of tip and sample during atomic force microscope measurements. *Journal of Vacuum Science & Technology*, 14(2):1250, **1996**.
- [Heumier93] T. Heumier and J. Carlsten. Detecting mode hopping in semiconductor lasers by monitoring intensity noise. *Quantum Electronics, IEEE Journal of*, 29(11):2756, **1993**. ISSN 0018-9197.

- [Hobbs09] P. C. D. Hobbs. *Building Electro-Optical Systems: Making It All Work*. John Wiley & Sons, Inc., **2009**.
- [Hoelscher00] H. Hoelscher, A. Schwarz, W. Allers, U. D. Schwarz, and R. Wiesendanger. Quantitative analysis of dynamic-force-spectroscopy data on graphite(0001) in the contact and noncontact regimes. *Phys. Rev. B*, 61(19):12678, **2000**.
- [Hoffmann09] P. M. Hoffmann. *Small Amplitude AFM Dekker Encyclopedia of Nanoscience and Nanotechnology, Second Edition*. Taylor & Francis, **2009**.
- [Holloway86] H. Holloway. Collection efficiency and crosstalk in closely spaced photodiode arrays. *Journal of Applied Physics*, 60(3):1091, **1986**.
- [Hoogenboom05] B. W. Hoogenboom, P. L. T. M. Frederix, J. L. Yang, S. Martin, Y. Pellmont, M. Steinacher, S. Zach, E. Langenbach, H.-J. Heimbeck, A. Engel, and H. J. Hug. A fabry-perot interferometer for micrometer-sized cantilevers. *Applied Physics Letters*, 86(7):074101, **2005**.
- [Hosaka95] H. Hosaka, K. Ito, and S. Kuroda. Damping characteristics of beam-shaped micro-oscillators. *Sensors and Actuators A: Physical*, 49(1-2):87, **1995**. ISSN 0924-4247.
- [Hosaka00] S. Hosaka, K. Etoh, A. Kikukawa, and H. Koyanagi. Megahertz silicon atomic force microscopy (afm) cantilever and high-speed readout in afm-based recording. *Journal of Vacuum Science & Technology B: Microelectronics and Nanometer Structures*, 18(1):94, **2000**.
- [Hosokawa08] Y. Hosokawa, T. Ichii, K. Kobayashi, K. Matsushige, and H. Yamada. Small amplitude frequency modulation atomic force microscopy of lead phthalocyanine molecules using cantilever with very high spring constant. *Japanese Journal of Applied Physics*, 47(7):6125, **2008**.
- [Hu95a] J. Hu, X. d. Xiao, D. F. Ogletree, and M. Salmeron. Atomic scale friction and wear of mica. *Surface Science*, 327(3):358, **1995**. ISSN 0039-6028.
- [Hu95b] J. Hu, X.-D. Xiao, and M. Salmeron. Scanning polarization force microscopy: A technique for imaging liquids and weakly adsorbed layers. *Applied Physics Letters*, 67(4):476, **1995**.
- [Hudlet98] S. Hudlet, M. Saint Jean, C. Guthmann, and J. Berger. Evaluation of the capacitive force between an atomic force microscopy tip and a metallic

- surface. *The European Physical Journal B - Condensed Matter and Complex Systems*, 2:5, **1998**. ISSN 1434-6028. 10.1007/s100510050219.
- [Huijsing99] J. Huijsing, R. Plassche, and W. Sansen (Editors). *Analog Circuit Design: Volt Electronics; Mixed-Mode Systems; Low-Noise and RF Power Amplifiers for telecommunication*. Kluwer Academic Publishers, **1999**.
- [Hutter93] J. L. Hutter and J. Bechhoefer. Calibration of atomic-force microscope tips. *Review of Scientific Instruments*, 64(7):1868, **1993**.
- [Hutter94] J. L. Hutter and J. Bechhoefer. Measurement and manipulation of van der waals forces in atomic-force microscopy. *Journal of Vacuum Science & Technology*, 12(3):2251, **1994**.
- [Hwu06] E. Hwu, K. Huang, S. Hung, and S. Hwang. Measurement of cantilever displacement using a compact disk/digital versatile disk pickup head. *Japanese Journal of Applied Physics*, 45(12):2368, **2006**.
- [Israelachvili07] J. Israelachvili. *Intermolecular and Surface Forces*. Elsevier, **2007**.
- [Jacobs98] H. O. Jacobs, P. Leuchtman, O. J. Homan, and A. Stemmer. Resolution and contrast in kelvin probe force microscopy. *Journal of Applied Physics*, 84(3):1168, **1998**.
- [Jacobs99] H. O. Jacobs, H. F. Knapp, and A. Stemmer. Practical aspects of kelvin probe force microscopy. *Review of Scientific Instruments*, 70(3):1756, **1999**.
- [Jeppesen09] C. Jeppesen, K. Molhave, and A. Kristensen. Competition between the thermal gradient and the bimorph effect in locally heated MEMS actuators. *Journal of Micromechanics and Microengineering*, 19(1):015008, **2009**. ISSN 0960-1317.
- [Johnson71] K. L. Johnson, K. Kendall, and A. D. Roberts. Surface energy and the contact of elastic solids. *Proceedings of the Royal Society of London. Series A, Mathematical and Physical Sciences*, 324(1558):pp. 301, **1971**. ISSN 00804630.
- [Jones24] J. E. Jones. On the Determination of Molecular Fields. II. From the Equation of State of a Gas. *Proceedings of the Royal Society of London. Series A*, 106(738):463, **1924**.
- [Kalinin01] S. V. Kalinin and D. A. Bonnell. Local potential and polarization screening on ferroelectric surfaces. *Phys. Rev. B*, 63(12):125411, **2001**.

- [Karrai95] K. Karrai and R. D. Grober. Piezoelectric tip-sample distance control for near field optical microscopes. *Applied Physics Letters*, 66(14):1842, **1995**.
- [Kassies04] R. Kassies, K. O. van der Werf, M. L. Bennink, and C. Otto. Removing interference and optical feedback artifacts in atomic force microscopy measurements by application of high frequency laser current modulation. *Review of Scientific Instruments*, 75(3):689, **2004**.
- [Kawai06a] S. Kawai and H. Kawakatsu. Atomically resolved amplitude modulation dynamic force microscopy with a high-frequency and high-quality factor cantilever. *Applied Physics Letters*, 89(1):013108, **2006**.
- [Kawai06b] S. Kawai and H. Kawakatsu. Atomically resolved dynamic force microscopy operating at 4.7 mhz. *Applied Physics Letters*, 88(13):133103, **2006**.
- [Kawai09] S. Kawai, T. Glatzel, S. Koch, B. Such, A. Baratoff, and E. Meyer. Systematic achievement of improved atomic-scale contrast via bimodal dynamic force microscopy. *Phys. Rev. Lett.*, 103(22):220801, **2009**.
- [Khan10] Z. Khan, C. Leung, B. A. Tahir, and B. W. Hoogenboom. Digitally tunable, wide-band amplitude, phase, and frequency detection for atomic-resolution scanning force microscopy. *Review of Scientific Instruments*, 81(7):073704, **2010**.
- [Kim93] H. S. Kim and P. J. Bryant. Tunnel current controlled atomic force microscope designs. *Journal of Vacuum Science & Technology*, 11(4):768, **1993**.
- [Kim07] M.-S. Kim, J.-H. Choi, J.-H. Kim, and Y.-K. Park. Si-traceable determination of spring constants of various atomic force microscope cantilevers with a small uncertainty of 1. *Measurement Science and Technology*, 18(11):3351, **2007**.
- [Kim10] D.-I. Kim, Y.-K. Jeong, M.-C. Kang, H.-S. Ahn, and K. H. Kim. Effect of relative vapor pressure on separation of nanoscale contact in atomic force microscope. *Journal of Applied Physics*, 108(11):114309, **2010**.
- [Kissel10] P. Kissel, J. van Heijst, R. Enning, A. Stemmer, A. D. Schlueter, and J. Sakamoto. Macrocyclic amphiphiles with 1,8-anthrylene fluorophores: Synthesis and attempts toward two-dimensional organization. *Organic Letters*, 12(12):2778, **2010**.

- [Klinov04] D. Klinov and S. Magonov. True molecular resolution in tapping-mode atomic force microscopy with high-resolution probes. *Applied Physics Letters*, 84(14):2697, **2004**.
- [Knoll10] A. Knoll, H. Rothuizen, B. Gotsmann, and U. Duerig. Wear-less floating contact imaging of polymer surfaces. *Nanotechnology*, 21(18):185701, **2010**.
- [Kobayashi09] K. Kobayashi, H. Yamada, and K. Matsushige. Frequency noise in frequency modulation atomic force microscopy. *Review of Scientific Instruments*, 80:043708, **2009**.
- [Kokavec07] J. Kokavec and A. Mechler. Investigation of fluid cell resonances in intermittent contact mode atomic force microscopy. *Applied Physics Letters*, 91(2):023113, **2007**. ISSN 00036951.
- [Koli03] K. Koli and K. Halonen. Introduction to current-mode circuit techniques. In *CMOS Current Amplifiers*, volume 681 of *The International Series in Engineering and Computer Science*, 1–9. Springer Netherlands, **2003**.
- [Kumaki96] J. Kumaki, Y. Nishikawa, and T. Hashimoto. Visualization of single-chain conformations of a synthetic polymer with atomic force microscopy. *Journal of the American Chemical Society*, 118(13):3321, **1996**.
- [Kumaki98] J. Kumaki and T. Hashimoto. Two-dimensional microphase separation of a block copolymer in a langmuir?blodgett film. *Journal of the American Chemical Society*, 120(2):423, **1998**.
- [Labuda11] A. Labuda and P. H. Grutter. Exploiting cantilever curvature for noise reduction in atomic force microscopy. *Review of Scientific Instruments*, 82(1):013704, **2011**.
- [Lau84] K. Lau, C. Harder, and A. Yariv. Longitudinal mode spectrum of semiconductor lasers under high-speed modulation. *Quantum Electronics, IEEE Journal of*, 20(1):71, **1984**. ISSN 0018-9197.
- [Lazar03] J. Lazar, P. Jedlicka, O. Cip, and B. Ruzicka. Laser diode current controller with a high level of protection against electromagnetic interference. *Review of Scientific Instruments*, 74(8):3816, **2003**.
- [Lee03] J. S. Lee, R. Hornsey, and D. Renshaw. Analysis of cmos photodiodes. ii. lateral photoresponse. *Electron Devices, IEEE Transactions on*, 50(5):1239, **2003**. ISSN 0018-9383.

- [Libbrecht93] K. G. Libbrecht and J. L. Hall. A low-noise high-speed diode laser current controller. *Review of Scientific Instruments*, 64(8):2133, **1993**.
- [Libioulle95] L. Libioulle, Y. Houbion, and J.-M. Gilles. Very sharp platinum tips for scanning tunneling microscopy. *Review of Scientific Instruments*, 66(1):97, **1995**.
- [Lide10] D. R. Lide. *CRC Handbook of Chemistry and Physics*. 101. CRC Press, 91 edition, **2010**. ISBN 978-0849304798.
- [Loh97] G. Loh and M. Santi. A multiple output current mirror. *U.S. Patent No. 5,627,732*, (5627732), **1997**.
- [Lozano10] J. R. Lozano, D. Kiracofe, J. Melcher, R. Garcia, and A. Raman. Calibration of higher eigenmode spring constants of atomic force microscope cantilevers. *Nanotechnology*, 21(46):465502, **2010**.
- [MacLennan07] B. J. MacLennan. A review of analog computing. Technical report, Department of Electrical Engineering & Computer Science, University of Tennessee, Knoxville, **2007**.
- [Magonov97] S. Magonov, V. Elings, and M.-H. Whangbo. Phase imaging and stiffness in tapping-mode atomic force microscopy. *Surface Science*, 375(2-3):L385, **1997**. ISSN 0039-6028.
- [Mamin01] H. J. Mamin and D. Rugar. Sub-attoNewton force detection at millikelvin temperatures. *Applied Physics Letters*, 79(20):3358, **2001**.
- [Marti90] O. Marti, J. Colchero, and J. Mlynek. Combined scanning force and friction microscopy of mica. *Nanotechnology*, 1(2):141, **1990**.
- [Martin87] Y. Martin, C. C. Williams, and H. K. Wickramasinghe. Atomic force microscope—force mapping and profiling on a sub 100- \AA -ring scale. *Journal of Applied Physics*, 61(10):4723, **1987**.
- [Maugis92] D. Maugis. Adhesion of spheres: The jkr-dmt transition using a dugdale model. *Journal of Colloid and Interface Science*, 150(1):243, **1992**. ISSN 0021-9797.
- [McLean97] R. S. McLean and B. B. Sauer. Tapping-mode afm studies using phase detection for resolution of nanophases in segmented polyurethanes and other block copolymers. *Macromolecules*, 30(26):8314, **1997**.

- [Medyanik06] S. N. Medyanik, W. K. Liu, I.-H. Sung, and R. W. Carpick. Predictions and observations of multiple slip modes in atomic-scale friction. *Phys. Rev. Lett.*, 97(13):136106, **2006**.
- [Melcher07] J. Melcher, S. Hu, and A. Raman. Equivalent point-mass models of continuous atomic force microscope probes. *Applied Physics Letters*, 91(5), **2007**.
- [Melmed91] A. J. Melmed. The art and science and other aspects of making sharp tips. *Journal of Vacuum Science & Technology B*, 9:601, **1991**.
- [Meyer88] G. Meyer and N. M. Amer. Novel optical approach to atomic force microscopy. *Applied Physics Letters*, 53(12):1045, **1988**.
- [Meyer90] G. Meyer and N. M. Amer. Optical-beam-deflection atomic force microscopy: The nacl (001) surface. *Applied Physics Letters*, 56(21):2100, **1990**.
- [Müller95] D. Müller, F. Schabert, G. Büldt, and A. Engel. Imaging purple membranes in aqueous solutions at sub-nanometer resolution by atomic force microscopy. *Biophysical Journal*, 68(5):1681, **1995**. ISSN 0006-3495.
- [Mo09] Y. Mo, K. turner, and I. Szlufarska. Friction laws at the nanoscale. *Nature*, 457:1116, **2009**.
- [Moore06] A. C. Moore, Z. Ninkov, and W. J. Forrest. Quantum efficiency overestimation and deterministic cross talk resulting from interpixel capacitance. *Optical Engineering*, 45(7):076402, **2006**.
- [Muller83] V. M. Muller, B. V. Derjaguin, and Y. P. Toporov. On two methods of calculation of the force of sticking of an elastic sphere to a rigid plane. *Colloids and Surfaces*, 7(3):251, **1983**. ISSN 0166-6622.
- [Nagai94] H. Nagai, M. Kume, A. Yoshikawa, and K. Itoh. Noise characteristics of a nd:yvo4 laser pumped by laser diode modulated at high frequency. *Appl. Opt.*, 33(24):5542, **1994**.
- [Naik03] T. Naik, E. K. Longmire, and S. C. Mantell. Dynamic response of a cantilever in liquid near a solid wall. *Sensors and Actuators A: Physical*, 102(3):240, **2003**. ISSN 0924-4247.
- [Nain10] A. S. Nain, S. Filiz, O. B. Ozdoganlar, M. Sitti, and C. Amon. Note: Aligned deposition and modal characterization of micron and submicron

- poly(methyl methacrylate) fiber cantilevers. *The Review of scientific instruments*, 81(1):016102, **2010**. ISSN 1089-7623.
- [Ng07] T. Ng and S. Thirunavukkarasu. Optical sensing limits in contact and bending mode atomic force microscopy. *Experimental Mechanics*, 47:841, **2007**. ISSN 0014-4851. 10.1007/s11340-007-9044-x.
- [Ohnesorge93] F. Ohnesorge and G. Binnig. True atomic resolution by atomic force microscopy through repulsive and attractive forces. *Science*, 260(5113):1451, **1993**.
- [Ojima86] M. Ojima, A. Arimoto, N. Chinone, T. Gotoh, and K. Aiki. Diode laser noise at video frequencies in optical videodisc players. *Appl. Opt.*, 25(9):1404, **1986**.
- [Olmstead83] M. A. Olmstead, N. M. Amer, S. Kohn, D. Fournier, and A. C. Boccara. Photothermal displacement spectroscopy: An optical probe for solids and surfaces. *Applied Physics A: Materials Science & Processing*, 32:141, **1983**. ISSN 0947-8396. 10.1007/BF00616610.
- [Pakarinen05] O. H. Pakarinen, A. S. Foster, M. Paajanen, T. Kalinainen, J. Katainen, I. Makkonen, J. Lahtinen, and R. M. Nieminen. Towards an accurate description of the capillary force in nanoparticle-surface interactions. *Modelling and Simulation in Materials Science and Engineering*, 13(7):1175, **2005**.
- [Patil07] S. Patil, N. Martinez, J. Lozano, and R. Garcia. Force microscopy imaging of individual protein molecules with sub-pico newton force sensitivity. *Journal of Molecular Recognition*, 20:516, **2007**.
- [Paulo01] A. S. Paulo and R. García. Tip-surface forces, amplitude, and energy dissipation in amplitude-modulation (tapping mode) force microscopy. *Physical Review B*, 64(19):193411+, **2001**.
- [Putman92a] C. Putman, B. De Grooth, N. Van Hulst, and J. Greve. A detailed analysis of the optical beam deflection technique for use in atomic force microscopy. *Journal of Applied Physics*, 72:6, **1992**.
- [Putman92b] C. Putman, B. Grooth, N. Hulst, and J. A detailed analysis of the optical beam deflection technique for use in atomic force microscopy. *Journal of Applied*, 72(1):6, **1992**.

- [Ramos06] D. Ramos, J. Tamayo, J. Mertens, and M. Calleja. Photothermal excitation of microcantilevers in liquids. *Journal of Applied Physics*, 99(12), **2006**.
- [Rasool10] H. Rasool, P. Wilkinson, A. Stieg, and J. Gimzewski. A low noise all-fiber interferometer for high resolution frequency modulated atomic force microscopy imaging in liquids. *Rev. Sci. Instrum.*, 81:023703, **2010**.
- [Ratcliff98] G. Ratcliff, D. Erie, and R. Superfine. Photothermal modulation for oscillating mode atomic force microscopy in solution. *Applied Physics Letters*, 72:1911, **1998**.
- [Rosenthal77] B. D. Rosenthal. Current subtracter. *U.S. Patent No. 4,055,812*, (4055812), **1977**.
- [Rugar88] D. Rugar, H. Mamin, R. Erlandsson, J. Stern, and B. Terris. Force microscope using a fiber-optic displacement sensor. *Review of Scientific Instruments*, 59:2337, **1988**.
- [Rugar89] D. Rugar, H. J. Mamin, and P. Guethner. Improved fiber-optic interferometer for atomic force microscopy. *Applied Physics Letters*, 55(25):2588, **1989**.
- [Rutten11] P. Rutten. World's fastest optical beam position sensor - private correspondence with the inventor, **2011**.
- [Sader99] J. E. Sader, J. W. M. Chon, and P. Mulvaney. Calibration of rectangular atomic force microscope cantilevers. *Review of Scientific Instruments*, 70(10):3967, **1999**.
- [Sader04] J. E. Sader and S. P. Jarvis. Accurate formulas for interaction force and energy in frequency modulation force spectroscopy. *Applied Physics Letters*, 84(10):1801, **2004**.
- [Sarid94] D. Sarid. *Scanning Force Microscopy: With Applications to Electric, Magnetic, and Atomic Forces*. Oxford University Press, **1994**.
- [Sarid07] D. Sarid. *Exploring Scanning Probe Microscopy with MATHEMATICA*. Wiley-VCH, **2007**.
- [Schaeffer96] T. E. Schaeffer, J. P. Cleveland, F. Ohnesorge, D. A. Walters, and P. K. Hansma. Studies of vibrating atomic force microscope cantilevers in liquid. *Journal of Applied Physics*, 80(7):3622, **1996**.

- [Schoenenberger89] C. Schoenenberger and S. Alvarado. A differential interferometer for force microscopy. *Review of Scientific Instruments*, 60:3131 , **1989**.
- [Schwarz97] U. D. Schwarz, O. Zwörner, P. Köster, and R. Wiesendanger. Quantitative analysis of the frictional properties of solid materials at low loads. i. carbon compounds. *Phys. Rev. B*, 56(11):6987, **1997**.
- [Schwarz00] U. D. Schwarz, H. Hoelscher, and R. Wiesendanger. Atomic resolution in scanning force microscopy: Concepts, requirements, contrast mechanisms, and image interpretation. *Phys. Rev. B*, 62(19):13089, **2000**.
- [Sedra09] A. S. Sedra and K. C. Smith. *Microelectronic Circuits*. Oxford University Press, **2009**.
- [Shluger94] A. L. Shluger, R. M. Wilson, and R. T. Williams. Theoretical and experimental investigation of force imaging at the atomic scale on alkali halide crystals. *Phys. Rev. B*, 49(7):4915, **1994**.
- [Sokolov00] I. Y. Sokolov and G. S. Henderson. Atomic resolution imaging using the electric double layer technique: friction vs. height contrast mechanisms. *Applied Surface Science*, 157(4):302 , **2000**. ISSN 0169-4332.
- [Spear96] J. D. Spear and R. E. Russo. Low noise position sensitive detector for optical probe beam deflection measurements. *Review of Scientific Instruments*, 67(7):2481, **1996**.
- [StandfordResearch] StandfordResearch. About lock-in amplifiers. Technical report, <http://www.thinksrs.com/downloads/PDFs/ApplicationNotes/AboutLIAs.pdf>.
- [Stark04] R. W. Stark. Optical lever detection in higher eigenmode dynamic atomic force microscopy. *Review of Scientific Instruments*, 75(11):5053, **2004**. ISSN 00346748.
- [Stark10] R. W. Stark. Bistability, higher harmonics, and chaos in afm. *Materials Today*, 13(9):24 , **2010**. ISSN 1369-7021.
- [Stemmer88] A. Stemmer, A. Engel, R. Häring, R. Reichelt, and U. Aebi. Miniature-size scanning tunneling microscope with integrated 2-axes heterodyne interferometer and light microscope. *Ultramicroscopy*, 25(2):171 , **1988**. ISSN 0304-3991.
- [Stemmer89] A. Stemmer, A. Hefti, U. Aebi, and A. Engel. Scanning tunneling and transmission electron microscopy on identical areas of biological specimens. *Ultramicroscopy*, 30(3):263 , **1989**. ISSN 0304-3991.

- [Stowe97] T. D. Stowe, K. Yasumura, T. W. Kenny, D. Botkin, K. Wago, and D. Rugar. Attonewton force detection using ultrathin silicon cantilevers. *Applied Physics Letters*, 71(2):288, **1997**.
- [Sulchek00] T. Sulchek, R. Hsieh, J. D. Adams, G. G. Yaralioglu, S. C. Minne, C. F. Quate, J. P. Cleveland, A. Atalar, and D. M. Adderton. High-speed tapping mode imaging with active q control for atomic force microscopy. *Applied Physics Letters*, 76(11):1473, **2000**.
- [Szlufarska08] I. Szlufarska, M. Chandross, and R. W. Carpick. Recent advances in single-asperity nanotribology. *Journal of Physics D: Applied Physics*, 41(12):123001, **2008**.
- [Tabor69] D. Tabor and R. H. S. Winterton. The direct measurement of normal and retarded van der waals forces. *Proceedings of the Royal Society of London. A. Mathematical and Physical Sciences*, 312(1511):435, **1969**.
- [Tamayo97] J. Tamayo and R. Garcia. Effects of elastic and inelastic interactions on phase contrast images in tapping-mode scanning force microscopy. *Applied Physics Letters*, 71(16):2394, **1997**.
- [Tang01] J. Tang, C. Wang, M. Liu, M. Su, and C. Bai. Effect of humidity on the surface adhesion force of inorganic crystals by the force spectrum method. *Chinese Science Bulletin*, 46:912, **2001**. ISSN 1001-6538. 10.1007/BF02900464.
- [Terris89] B. D. Terris, J. E. Stern, D. Rugar, and H. J. Mamin. Contact electrification using force microscopy. *Phys. Rev. Lett.*, 63(24):2669, **1989**.
- [Tersoff83] J. Tersoff and D. R. Hamann. Theory and application for the scanning tunneling microscope. *Phys. Rev. Lett.*, 50(25):1998, **1983**.
- [Ton-That00] C. Ton-That, A. G. Shard, and R. H. Bradley. Thickness of spin-cast polymer thin films determined by angle-resolved xps and afm tip-scratch methods. *Langmuir*, 16(5):2281, **2000**.
- [Torbrugge08] S. Torbrugge, J. Lubbe, L. Troger, M. Cranney, T. Eguchi, Y. Hasegawa, and M. Reichling. Improvement of a dynamic scanning force microscope for highest resolution imaging in ultrahigh vacuum. *Review of Scientific Instruments*, 79(8):083701, **2008**.
- [Torii96] A. Torii, M. Sasaki, K. Hane, and S. Okuma. A method for determining the spring constant of cantilevers for atomic force microscopy. *Measurement Science and Technology*, 7:179, **1996**.

- [Tri08] *PANdrive PD013-42 and TMCM-013 and TMCM-013-LA Manual, Tri-namic GmbH, Hamburg Germany, 2008.*
- [Umeda91] N. Umeda, S. Ishizaki, and U. H. Scanning attractive force microscope using photothermal vibration. *Journal of Vacuum Science & Technology B*, 9:1318 , **1991**.
- [Verbridge06] S. S. Verbridge, L. M. Bellan, J. M. Parpia, and H. G. Craighead. Optically driven resonance of nanoscale flexural oscillators in liquid. *Nano Letters*, 6(9):2109, **2006**.
- [Viani99] M. B. Viani, T. E. Schaffer, A. Chand, M. Rief, H. E. Gaub, and P. K. Hansma. Small cantilevers for force spectroscopy of single molecules. *Journal of Applied Physics*, 86(4):2258, **1999**.
- [v.Pfeil02] A. v. Pfeil and T. von Freyhold. Beam shaping of broad-area diode lasers: principles and benefits. volume 4648, 82–90. SPIE, **2002**.
- [Walters96] D. A. Walters, J. P. Cleveland, N. H. Thomson, P. K. Hansma, M. A. Wendman, G. Gurley, and V. Elings. Short cantilevers for atomic force microscopy. *Review of Scientific Instruments*, 67(10):3583 , **1996**. ISSN 0034-6748.
- [Wang07] S. Wang, X. Wang, Y. Liu, B. Huang, and H. Wang. *Parameter optimization of optically excited microresonator by a semiconductor laser subject to optical feedback*. 201800. Spie, **2007**.
- [Wang10] X. Wang, M. Zhao, and D. D. Nolte. Ambient molecular water accumulation on silica surfaces detected by a reflectance interference optical balance. *Applied Physics Letters*, 97(18):183702, **2010**.
- [Webber08] G. B. Webber, G. W. Stevens, F. Grieser, R. R. Dagastine, and D. Y. C. Chan. Variations in properties of atomic force microscope cantilevers fashioned from the same wafer. *Nanotechnology*, 19(10):105709, **2008**.
- [Weinberg93] S. Weinberg. *Dreams of a final theory : the search for the fundamental laws of nature*. Hutchinson Radius, **1993**.
- [Weisenhorn89] A. L. Weisenhorn, P. K. Hansma, T. R. Albrecht, and C. F. Quate. Forces in atomic force microscopy in air and water. *Applied Physics Letters*, 54(26):2651, **1989**.
- [Wenning01] L. Wenning and M. H. Müser. Friction laws for elastic nanoscale contacts. *EPL (Europhysics Letters)*, 54(5):693, **2001**.

- [White97] D. N. White. A computationally efficient alternative to the Buckingham potential for molecular mechanics calculations. *Journal of Computer-Aided Molecular Design*, 11:517, **1997**. ISSN 0920-654X. 10.1023/A:1007911511862.
- [Xiao87] M. Xiao, L.-A. Wu, and H. J. Kimble. Precision measurement beyond the shot-noise limit. *Phys. Rev. Lett.*, 59(3):278, **1987**.
- [Xu97] S. Xu and G.-y. Liu. Nanometer-scale fabrication by simultaneous nanoshaving and molecular self-assembly. *Langmuir*, 13(2):127, **1997**.
- [Yamashita07] H. Yamashita, N. Kodera, A. Miyagi, T. Uchihashi, D. Yamamoto, and T. Ando. Tip-sample distance control using photothermal actuation of a small cantilever for high-speed atomic force microscopy. *Review of Scientific Instruments*, 78:083702, **2007**.
- [Yang00] J. Yang, T. Ono, and M. Esashi. Surface effects and high quality factors in ultrathin single-crystal silicon cantilevers. *Applied Physics Letters*, 77(23):3860, **2000**.
- [Yang05] J. L. Yang, M. Despont, U. Drechsler, B. W. Hoogenboom, P. L. T. M. Frederix, S. Martin, A. Engel, P. Vettiger, and H. J. Hug. Miniaturized single-crystal silicon cantilevers for scanning force microscopy. *Applied Physics Letters*, 86(13):134101, **2005**.
- [Young72] R. Young, J. Ward, and F. Scire. The topografiner: An instrument for measuring surface microtopography. *Review of Scientific Instruments*, 43(7):999, **1972**. ISSN 0034-6748.
- [Ziegler07] D. Ziegler, J. Rychen, N. Naujoks, and A. Stemmer. Compensating electrostatic forces by single-scan kelvin probe force microscopy. *Nanotechnology*, 18(22):225505+, **2007**. ISSN 0957-4484.
- [Ziegler09] D. Ziegler. *Techniques to Quantify Local Electric Potentials and Eliminate Electrostatic Artifacts in Atomic Force Microscopy*. Ph.D. thesis, ETH Zuerich, **2009**.

Comments/Response to Case ID: 0036A4B0

ReplyTo: Copyrights@ieee.org

From: Jacqueline Hansson

Date: 03/11/2011

Subject: Re: Using 2 images
in a PhD Thesis

Send To: Raoul Enning
<enning@nano.mavt.ethz.ch>

cc:

Dear Raoul Enning :

In response to your letter below, we are happy to grant you permission to reuse the IEEE copyrighted figure requested in all electronic and printed formats.

Our only requirements are that you credit the original source (author, paper, and publication), and that the IEEE copyright line (© [year of original publication] IEEE) appears prominently with the reprinted figure.

Sincerely,

Jacqueline Hansson, Coordinator

© © © © © © © © © © © © © © © © © © ©

IEEE Intellectual Property Rights Office
445 Hoes Lane
Piscataway, NJ 08855-1331 USA
+1 732 562 3966 (phone)
+1 732 562 1746 (fax)

IEEE-- Fostering technological innovation
and excellence for the benefit of humanity.

© © © © © © © © © © © © © © © © © © ©

Curriculum Vitae

Personal Data

Name: Raoul Enning
Date of Birth: September 5, 1980
Place of Birth: Charlottesville, Virginia, USA
Citizen of: Germany and the United States of America

Education

2008 – 2011 **PhD candidate under Prof. Andreas Stemmer at the
Chair of Nanotechnology**
Department of Mechanical and Process Engineering
ETH Zuerich, Switzerland

2005 – 2008 **Master's Degree in Biomedical Engineering**
Department of Electrical Engineering
ETH Zuerich, Switzerland

1998 – 2003 **Bachelor's Degree in Computer Engineering**
Department of Electrical and Computer Engineering
University of Maryland at College Park, Maryland, USA

Professional Experience

2003 – 2005 **Application Engineer at Philips Automotive (APM), Wetzlar, Germany**
Design and implementaiton of an MPEG-2 embedded
audio decoder for the automobile industry (MP3 - decoder)